Double Resonant Coherent Excitation of Highly-Charged Ions in Crystals

Dissertation

zur Erlangung des Doktorgrades
der Naturwissenschaften

vorgelegt beim Fachbereich Physik
der Johann Wolfgang Goethe-Universität
in Frankfurt am Main

von

Alena Ananyeva

aus Almaty

Frankfurt (2014)

(D 30)

vom Fachbereich Physik der

Johann Wolfgang Goethe - Universität als Dissertation angenommen.

Dekan: Professor J. Stroth

1. Gutachter: Professor R. Dörner

2. Gutachter: Professor T. Azuma

Datum der Disputation: 27.02.2015

Contents

Introduction

Excited states of few-electron ions are an ideal object to investigate the dynamics of strongly-correlated bound electrons. The simplest cases among such systems are H-like and He-like ions of which numerous photoexcitation spectroscopies have been performed using synchrotron radiation [0.1, 0.2]. However, synchrotron radiation is not applicable to few-electron high-Z ions because of its limited wavelength and intensities. Another efficient instrument to produce excited ions is a polarization-controlled laser field [0.3]. Restrictions for laser spectroscopy are usually caused by the frequency ν_L of the light emitted by the laser. Typically, the energy E_L of the photons produced by a visible light laser is about few eV. This value can be increased by using a beam of ions accelerated up to relativistic velocities, aligned antiparallel to the laser direction. Due to the Doppler Effect, the energy of the laser photons, in the rest frame of the ions, $E_L{}'$ can be shifted to a higher value:

$$E_L' = \sqrt{\frac{(1 + \beta)}{(1 - \beta)}} E_L \; , \tag{0.1}$$

where β is the ratio between the ions velocity $\boldsymbol{v}$ and the speed of light [0.4].
Therefore the wavelength becomes:

$$\nu_L{}' = \sqrt{\frac{(1 - \beta)}{(1 + \beta)}} \nu_L \tag{0.2}$$

Considering the limitations of the modern ion accelerators ($\gamma < 3$) [0.5, 0.6], the highest achievable transition energy is about 100 eV for laser spectroscopy ($\nu_L' \approx 10^{16}$ s^{-1}) [0.7].

The present work is dedicated to an alternative method for controlled production of the excited $n = 2, 3, 4$ and 5 states in few-electron high-Z ions using the electric field of a crystal-target. Relativistic projectiles passing a thin crystal-target feel the Coulomb potential of the crystal atoms as an oscillating electric field with frequency ν_{field}. If the frequency of the crystal field ν_{field} being seen by the projectiles is equal to the frequency ν_{ij} of the transition from the i into j state in the ions, Resonant Coherent Excitation (RCE) may occur [0.8]. The field frequency ν_{field}, in the rest frame of the projectile ions, is defined by the velocity of the ions $\boldsymbol{v}$ and distance d between the crystal atoms:

$$\nu_{field} = \frac{\gamma \boldsymbol{v}}{d}. \tag{0.3}$$

In this case, the frequency of the electric field in the rest frame of the ions is directly proportional to the ions velocity $\gamma\boldsymbol{v}$ (here γ is the Lorentz factor). The frequency, seen by the ions at relativistic velocities becomes very high ($\nu_{field} \approx 10^{18}$ s^{-1}), which is equivalent to keV transition energies:

$$E_{ij} = \hbar\nu_{ij} = \hbar\nu_{field} = \frac{\hbar\gamma\boldsymbol{v}}{d}. \qquad (0.4)$$

Moreover, a crystal field frequency can be tuned by changing the beam energy and by adjusting the target angular orientation with high precision. Whereas, a laser frequency in the rest frame of the projectiles can be tuned only by changing the beam energy. This makes the RCE phenomenon a universal instrument for production of excited states of highly-charged ions in a wide range.

The RCE phenomenon was predicted by V. V. Okorokov in 1965 [0.8]. An experimental investigation of the RCE has been started by S. Datz with light ions at planar channeling conditions [0.9]. For the first time coherent excitation of the ions in crystals was obtained as a selective resonance process. The experiments were performed with H-like light ions ($Z = 5$ to $Z = 9$) supplied by the Oak Ridge National Laboratory tandem accelerator. The ions with energy of about tens MeV/u were passing thin oriented Au and Ar crystal targets. The RCE into levels up to $n = 3$ (below 1 keV) have been observed from the survival charge-state fraction of the ions measured as a function of the beam velocity [0.10].

Later on, high-precision goniometers started to be used for this kind of experiments. A possibility to rotate the target with small steps improved the method in many ways. First, it replaced the scanning over the beam energy which can be extremely time-consuming. Second, it allowed the adjustment of the resonance conditions with high precision. And third, it gave a possibility to excite different transitions using the same crystal differently oriented relatively to the projectile ions direction. The RCE in N^{6+} and Mg^{11+} ions was observed at planar channeling conditions by measuring the initial charge-state fraction as a function of the angular orientation of the target-crystal mounted in a goniometer [0.11]. The excitation into a 2p level has been observed (about 1.47 keV transition energy).

Developing accelerator technics allowed extending the study towards higher transition energies of the heavier ions. Several RCE experiments on highly-charged ions were performed at the HIMAC facility in Tokyo [0.5] with beams of Ar and Fe ions at hundreds of MeV/u projectile energy. The RCE into the $n = 2$ level has been clearly demonstrated in Ar^{17+} (about 3.3 keV) at planar channeling in a thin Si-crystal [0.12, 0.13]. Coherent excitation into the $n = 3$ state (about 3.9 keV) was for the first time seen from the charge-state distribution of

6

Li-like Fe at planar channeling conditions [0.14]. A variation of the X-ray emission from the decay of the excited 2p states of Ar^{17+} was studied as a function of the angular crystal orientation in [0.15, 0.16]. Nowadays, beams of all ions species are available in a wide energy range. The GSI accelerator facility (Darmstadt) can provide highly-charged uranium (up to bare) with energy up to 1 GeV/u. The resonant excitation of the $2s_{1/2} \rightarrow 2p_{3/2}$ transition in U^{89+} (around 4.5 keV) was observes with a cooled ions beam at 190 MeV/u passing a Si-crystal target at (220) planar channeling conditions [0.17].

Recently, an RCE at non-channeling conditions has been observed for $n = 2$ transition in H-like Ar ion traveling through a Si crystal for the first time [0.18]. This phenomenon was called Three-dimensional RCE (3D-RCE). The channeling condition has been required in the previous experiments to suppress close collisions with the crystal atoms, which destroy the coherence between the transition frequency and the frequency of the crystal field in the rest frame of the projectiles. This is particularly essential for low Z and low energy ions. However, the ions penetrating a crystal-target in arbitrary directions also feel the crystal oscillating potential. In principle, RCE does not require channeling conditions. A 3D-RCE is adding two new features to the existing RCE at axial and planar channeling. First of all, it allows polarization control of the excited states in the ions using the electric field of the crystal [0.15, 0.17]. Furthermore, it gives the possibility for a sequential excitation to higher states of the ions using simultaneously the potentials of different crystal orientations.

The main goal of the present work was to investigate the phenomenon of Double Resonant Coherent Excitation (DRCE) into higher excited states, such as $n = 3$, 4 and 5, in relativistic H-like and He-like Ar ions. For this, three experiments have been performed at HIMAC accelerator facility (Japan) using beams of Ar^{17+} and Ar^{16+} with energy of few-hundred MeV/u.

The first chapter of the dissertation, "Ion – atom collisions", reviews the main processes occurring when ions penetrate matter, such as excitation of the projectile and target atoms and charge exchange between the colliding partners. Probabilities of these processes for light and heavy collision partners at different energies are discussed in Section 1. The interaction of charged projectiles with crystals is different from amorphous targets. Basic terms describing the crystal potential and different ions motion modes in crystal-targets, such as axial or planar channeling and non-channeling motion, are given in the beginning of Section 2. This section further describes the RCE phenomenon and explains the difference between RCE and DRCE processes. The section is finalized with a discussion on the possible

de-excitation ways of the ions and their probabilities calculated for H-like and He-like Ar ions.

Chapter 2, "Experiment", presents the methods and the tools used in this work to observe 3D-RCE DRCE of highly-charged ions in crystal targets. This chapter starts with a short presentation of the HIMAC facility and methods of the production of the highly-charged ions used in the experiments. The parameters of the beams used for different measurements are discussed in the second section of this chapter. The experimental setup consisting of the high-precision goniometer, the vacuum chamber and the target is presented in section 2.3. Section 2.4 reports on the working principle of the detectors used for the measurements of the ion yield and X-ray emission. In Section 2.5 the target adjustment to the resonance conditions is explained step by step. A scheme of the data acquisition used for the measurements is given in the last section of this chapter.

Chapter 3 is dedicated to the data analysis. The method, used to obtain the resonance spectra from the measured ion and X-ray yields, is presented here.

The results of the performed experiments are summarized in Chapter 4. Possible improvements and further applications of the developed method are covered in the last chapter, "Conclusions".

1 Ion – atom collisions

This chapter is dedicated to the processes occurring in collisions of energetic ions with atoms. The first section deals with the basic processes, such as excitation, ionization and electron capture. The special case of in interaction with crystal targets, which is different from the interaction with the amorphous ones, is discussed in detail in the second section. Ions motion in crystal-targets under axial and planar channeling and non-channeling conditions are considered here.

1.1 Ion-atom collisions

In collisions of energetic ions with neutral atoms, the projectile ion often changes its charge-state by capturing electron(s) from the target or by losing its orbital electron(s). Electron capture and electron loss are usually accompanied by other processes like excitation or ionization followed by the de-excitation of the colliding partners via photon and/or Auger decay. The probability of the electron capture and electron loss is defined by the atomic structure of the colliding partners and their relative velocity. Many theoretical approaches and semi-empirical formulas have been developed to estimate cross sections of the excitation and ionization processes for different combinations of the projectiles and targets for each energy range [1.1, 1.2]. This work was completed by a large amount of experimental data mentioned below.

1.1.1 Excitation

A collision of an ion with a neutral atom may result in a single or multiple excitation of one or both colliding partners:

$$X^{q+} + A \rightarrow X^{q+} + A^*, \text{ or}$$

$$X^{q+} + A \rightarrow (X^{q+})^* + A^*,$$

(1.1)

here X^{q+} is a projectile ion, q is the projectile initial charge and A denotes a target atom.

The excitation cross section of a target atom from the ground state into an excited state n for optically allowed transitions ($\Delta l = \pm 1$, $\Delta S = 0$) can be calculated in the Born approximation, known as the Bethe cross section:

$$\sigma_{ex}(n) = \frac{4\pi \, a_0^2 Z_1^2}{T/R} \left[a \ln \frac{T}{R} + b + \frac{c}{T/R} + O\left(\frac{E_n^2}{T^2}\right) \right],$$

(1.2)

and for optically forbidden transitions ($\Delta l = 0, \pm 2, \pm 3 \dots, \Delta S = 0$):

$$\sigma_{ex}(n) = \frac{4\pi \, a_0^2 Z_1^2}{T/R} \left[b + \frac{c}{T/R} + O\left(\frac{E_n^2}{T^2}\right) \right],$$

(1.3)

where a, b and c are factors listed in [1.3]; a_0 is the Bohr radius, R is the Rydberg constant, Z_1 is the projectile charge, $T/R = (v/v_0)^2$, v is the projectile velocity, v_0 is the Bohr velocity and E_n is the level energy. The numbers n, L and S are principal, azimuthal and spin projection quantum numbers of the excited state of the target atom, respectively.

Formulae (1.1) and (1.2) can be applied for high energy non-relativistic collisions. In the case of relativistic collisions the excitation cross section (1.4) for optically allowed and forbidden (1.5) transitions are calculated with:

$$\sigma_{ex}(n) = \frac{8\pi \, a_0^2 Z_1^2}{m_e v^2/R} \left\{ A \left[\ln\left(\frac{\beta^2}{1-\beta^2}\right) - \beta^2 \right] + C \right\},$$ (1.4)

$$\sigma_{ex}(n) = \frac{8\pi \, a_0^2 Z_1^2}{m_e v^2/R} \, B,$$ (1.5)

where m_e is the electron rest mass, $\beta = v/c$ and c is the speed of light. The factors A, B and C are listed in [1.3, 1.4].

In figure 1.1 a dependence of the reduced cross section $\tilde{\sigma}$ on the energy $\tilde{E}$ calculated for H-like and He-like ions using the scaling law (1.6) is presented [1.5]:

$$\tilde{\sigma} = \frac{\omega_{1n}^2}{q f_{1n}} \sigma \quad \text{and} \quad \tilde{E} = \frac{E}{q \omega_{1n}},$$ (1.6)

where q is the ion charge-state, ω_{1n} - electron transition energy in atomic units and f_{1n} – the generalized oscillator strength (GOS) for the specific excitation, as

$$\tilde{\sigma}(\tilde{E}) = \frac{A \, exp\left(-\alpha/\tilde{E}_{150}^{\frac{1}{2}}\right) \, ln\left(e + \gamma \tilde{E}_{150}\right)}{\left(1 + C\tilde{E}_{150}^{-\beta}\right)\tilde{E}_{150}} \times 10^{-17},$$ (1.7)

here $\tilde{E}_{150} = \tilde{E}/150$, e is the Napier's constant and coefficients A, B, α, β and γ are listed in [1.5] for H and He-like targets.
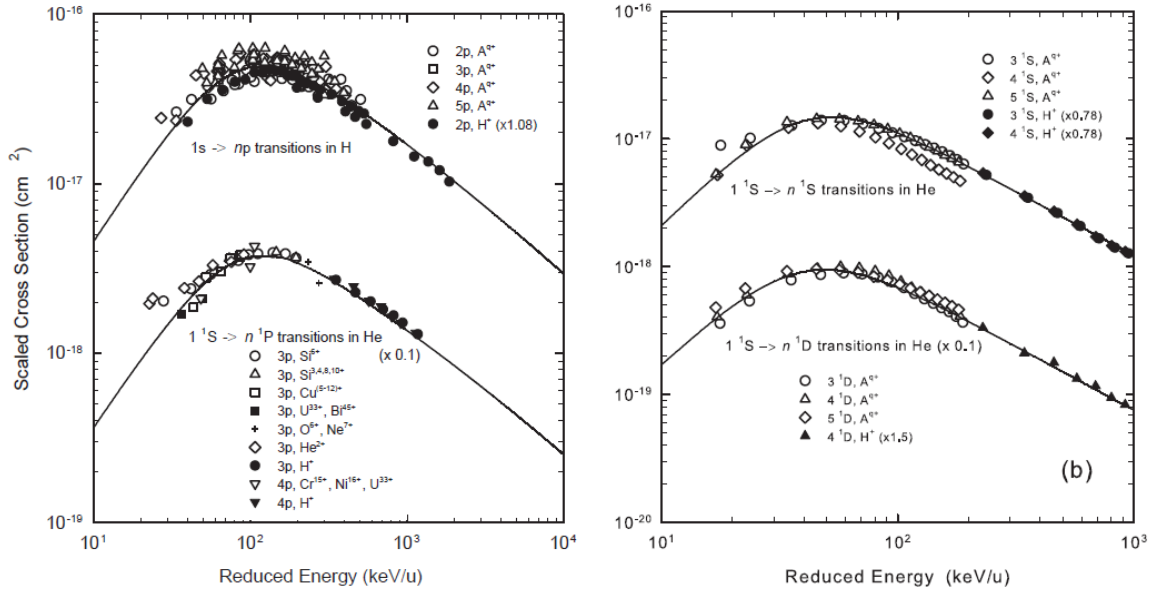
Figure 1.1 *Excitation cross section scaling by Janev [1.5] for optically allowed transitions. The curves are calculated using (1.5) and (1.6) for optically allowed 1s → np transitions in H (upper left curve), $1^1S \rightarrow n^1P$ transition in He (lower left curve) and for optically forbidden $1^1S \rightarrow n^1S$, $1^1S \rightarrow n^1D$ transitions in He. Open symbols represent the experimental data taken from [1.6-1.10] for different impacts.*

This scaling rule shows that, for a fixed energy, the nonscaled excitation cross section as a function of the ion charge-state q does not saturate at high q values but decreases after reaching a maximum.

1.1.2 Charge transfer

An ion colliding with an atom may undergo a change of initial charge state. A removal of one or more electrons from the projectile is usually called projectile ionization or electron loss:

$$X^{q+} + A \rightarrow X^{(q+m)+} + A + m\,e^-,\tag{1.8}$$
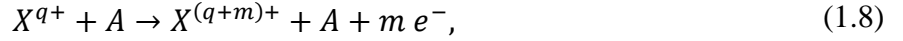
where $m \geq 1$ is the number of the ejected electrons to the target from the projectile.

A gain of one or more of the target-electrons by the projectile is known as electron-capture:

$$X^{q+} + A \rightarrow X^{(q-k)+} + A^{k+},\tag{1.9}$$

here $k \geq 1$ is the number of the captured electrons.

Electron loss and electron capture have different dependences on the projectile charge, E, effective charge of the target atoms Z_{eff}^2 and on the relative velocity of the collision v. At high energies the cross section of the electron capture σ_{EC} and electron loss σ_{EL} processes scales as:

$$\sigma_{EC} \sim \frac{q^5 Z_{eff}^5}{E^{5.5}}, \quad v^2 \gg I_p,$$

$$\sigma_{EL} \sim \frac{Z_{eff}^2}{q^2\,E}, \quad v^2 \gg I_p,\tag{1.10}$$

where I_p is the projectile electron binding energy.

The competition between these two processes at different energy regimes is demonstrated in figure 1.2 by the example of the U^{39+} projectile ions colliding with Ar atoms [1.11, 1.12].

The calculation indicates that the two processes are complementary: at energies below 1 MeV/u the electron capture is a dominated process, whereas at high energies it is overtaken by the electron loss. This result is supported also by the experimental data. At the intermediate energy, between 1 and 30 MeV/u, where the cross sections have a comparable size, the charge transfer is defined by the atomic structure of the projectile and target atoms. Two very different mechanisms contribute to the electron capture: the radiative capture, REC, in which the excess energy is carried away by a photon, and the non-radiative capture, NRC. An NRC is a capture of electrons bound in the target where the energy difference is compensated by a change of the projectile velocity and REC is a capture of a "free" electron. The REC process

is dominant in high-energy collisions, whereas the non-radiative capture becomes negligibly small.
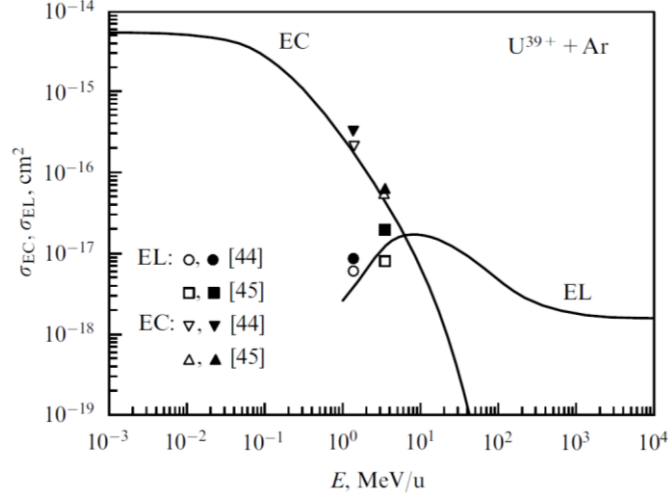

Figure 1.2 *Electron capture (EC) and electron loss (EL) cross sections in collisions of U^{39+} ions with Ar atoms as a function of the projectile energy. Empty and solid symbols: one-electron and total cross sections, respectively, from experiments [1.11] and [1.12]. Solid curves: calculations by the CAPTURE, DEPOSIT, and RICODE programs [1.13]*

The basic methods for calculating the electron capture cross section, such as the close-coupling method with an atomic or molecular basis [1.17 - 1.20], the electron tunneling model [1.21], the absorbing sphere model based on the Landau-Zener theory [1.22], the classical overbarrier-transition model [1.23], the distorted-wave approximation with normalization [1.24, 1.25] give a satisfactory agreement with the experimental data in their respective range of validity.

In figure 1.3 the electron capture cross section of Pb^{25+} ions colliding with Ar atoms, calculated with the CAPTURE code and a semi-empirical formula (1.11), are compared with the experimental data:

$$\sigma_{cap} = \frac{1.1 \times 10^{-8}}{\tilde{E}^{4.8}} \frac{q^{0.5}}{Z_T^{1.8}} \left(1 - exp\left(-0.037\tilde{E}^{2.2}\right)\right) \times \left(1 - exp\left(-2.44 \times 10^{-5}\tilde{E}^{2.6}\right)\right)$$

$$\tilde{E} = \frac{E}{Z_T^{1.25}q^{0.7}}, \quad q \geq 3, \quad \tilde{E} \geq 10$$

(1.11)

At high energies the experimental results and the theoretical models are in a good agreement but below 3 MeV/u the semi-empirical formula does not describe correctly the data. At the lower energy collisions the electron capture process is overtaken by the projectile ionization. Generally, the projectile ionization cross section increases with projectile energy E and it has a maximum at around $v^2 \sim 1.5I_1/2R$ and decreases as E^{-1} at the high energy limit.
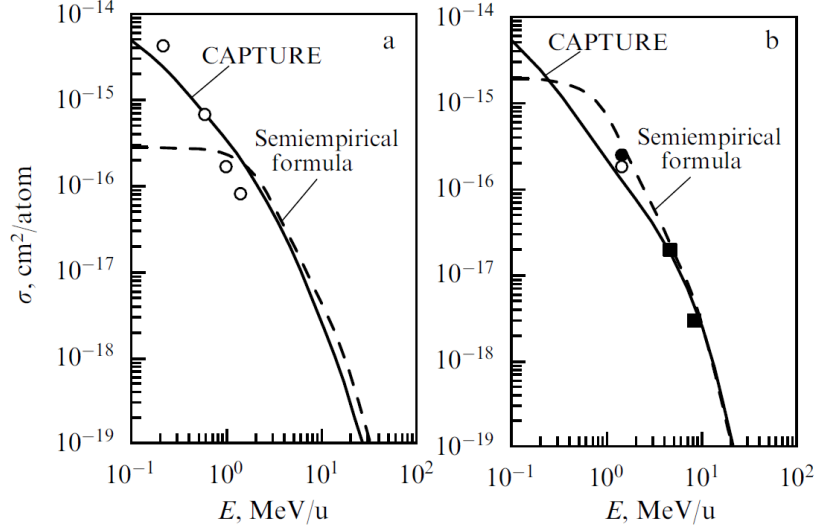
Figure 1.3 *Electron capture cross sections in collisions of*
(a): Pb^{25+} ions with Ar atoms (empty circles – experiment [1.11], solid curves – calculation using CAPTURE code [1.14]);
(b): Pb^{39+} ions with N_2 molecules are solid and empty circles are one-electron and total capture cross sections from the experiment [1.11], solid squares - [1.15], dashed curves – calculation with semi-empirical formula [1.16]

According the classical Born theory, neglecting the binding energy of the projectile electron [1.26], the electron loss of light ions passing low-Z targets at high energy is:

$$\sigma_{loss} = 4\pi a_0^2 Z_1^{-2} (Z_2^2 + Z_2) \left(\frac{v_0}{v}\right)^2, \tag{1.12}$$

light ions passing intermediate Z targets with $Z_1 \leq Z_2^{1/3}$:

$$\sigma_{loss} = \pi a_0^2 Z_1^{-1} Z_2^{2/3} \left(\frac{v_0}{v}\right), \tag{1.13}$$

heavy ions passing low Z targets:

$$\sigma_{loss} = \pi a_0^2 Z_1^{1/3} Z_2^2 \left(\frac{v_0}{v}\right)^3 \tag{1.14}$$

and heavy ions passing high Z targets:

$$\sigma_{loss} = \pi a_0^2 \left(Z_1^{1/3} + Z_2^{1/3}\right)^2 \left(\frac{v_0}{v}\right)^2, \tag{1.15}$$

The electron binding energy was taken into account by Alton et al. [1.27]:

$$\sigma_{loss} = \pi a_0^2 N_j \left(Z_1^{1/3} + Z_2^{1/3}\right)^2 \left(\frac{v_0}{v}\right)^2, \tag{1.16}$$

here N_j – outermost electrons with ionization energy I_j.

A semi-empirical formula obtained by Shevelko et al. using the relativistic Born approximation (the RICODE program [1.13]) provides electron loss cross sections for heavy, many-electron ions in a wide energy range:

$$\sigma_{loss} = A(Z_2 + 1)^2 \frac{u}{u^2 + 3.5} \left(\frac{R}{I_1}\right)^{1+0.01q} \times \left(4 + \frac{1.31}{n_0} ln(4u + 1)\right),$$

$$(1.17)$$

$$u = \frac{v}{I_1/R} = \frac{(\beta c)^2}{I_1/R},$$

here $A = 0.88 \times 10^{-16}$ cm^2, n_0 denotes the principal quantum number of the projectile outer shell electron and I_1 is the projectile ionization potential.
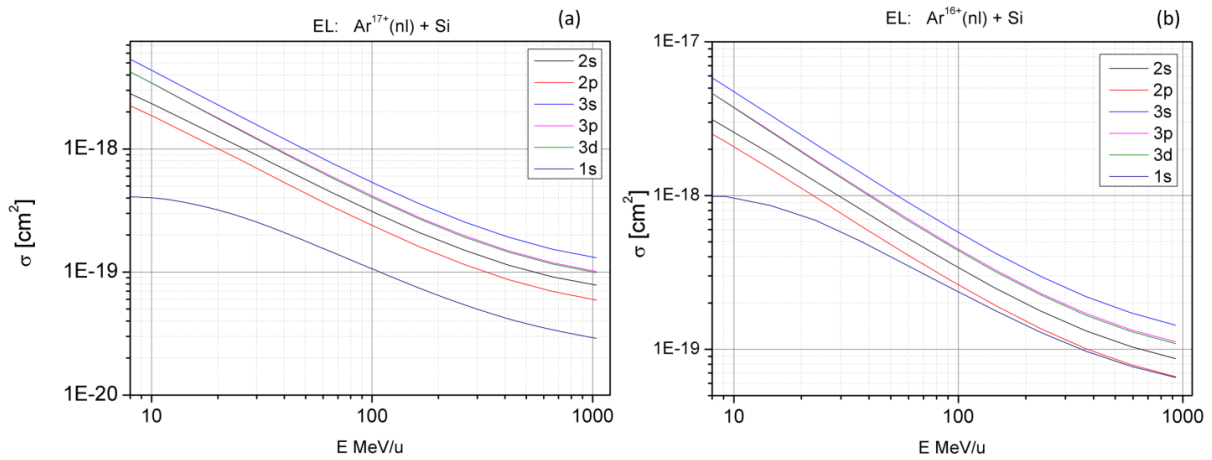
Figure 1.4 *Electron loss cross sections from different states in H-like (a) and He-like (b) Ar ions calculated by the RICODE program [1.13].*

For heavy ions the role of multi-electron processes increases and the contribution of the multi-electron loss cross section can be more than 50% to the total one [1.28].

The electron loss cross section calculated with RICODE program has been used in the present work for investigation of the highly-charged Ar ions penetrating a Si-target. In figure 1.4 the electron loss cross sections from different states in H-like and He-like Ar ions passing a Si-target are shown. The calculation shows higher projectile ionization probability from the excited states than from the ground state.

1.2 Ion – crystal interaction

In the case of a charged projectile passing an ordered structure, like a crystal, the interaction is different from a penetration through an amorphous target. Each crystal has a unique structure which can by described by an averaged periodic potential. Such a potential may affect the trajectory of the projectile in the target.

1.2.1 Crystal structure

The structure of a crystal can be considered as a Bravais lattice described by three unit vectors a_1, a_2 and a_3 and the set of integers n_1, n_2 and n_3 so that each lattice point, identified by a vector r, can be obtained from:

$$r = n_1 a_1 + n_2 a_2 + n_3 a_3, \tag{1.18}$$

where n_1, n_2 and n_3 are all possible integers [1.29].

The Bravias lattice of a crystal is a unit element which repeats in three dimensions to the crystal size. An arbitrary Bravias lattice is sketched in figure 1.5.
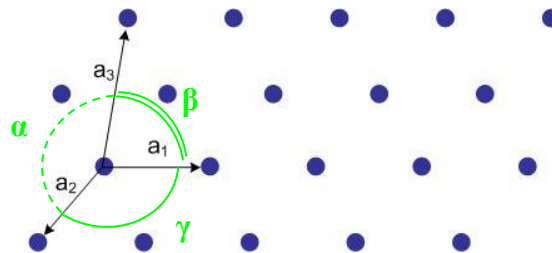

Figure 1.5 *An arbitrary Bravias lattice.*

Depending on the length of the a_1, a_2 and a_3 vectors and the values of the angles α, β and γ between them, there are seven types of crystal systems: triclinic, monoclinic, orthorhombic, tetragonal, cubic, trigonal and hexagonal. A crystal system may have different types of lattice [1.29].

In the simplest lattice is the one having an atom in every corner of the lattice polygon. This is the so-called primitive lattice. Further, a crystal system may have additionally two atoms in the polygons bases centers (base-centered lattice), or an atom in the volume center of the polygon (volume-centered lattice) or an atom in the center of every face of the polygon (face-centered lattice). Altogether, there are fourteen Bravias lattices.

An axial orientation is a group of crystal atoms located along the axis which always goes from the origin of the coordinate system based on the unit vectors a_1, a_2 and a_3 to the point with coordinates (k, l, m). The coordinates k, l and m are integers called Miller indices.

16

Crystallographic axes are denoted by values of the corresponding Miller indices enclosed in square brackets as [k l m]. For indices with negative value the notation becomes [$\bar{k}\,\bar{l}\,\bar{m}$].

In figure 1.6 few examples of the axial orientations in an arbitrary crystal system are shown. In the present notation, the unit vectors directions can be named as [100], [010] and [001]. The atoms belonging to the axes [110] and [111] are marked with magenta color in figure 1.6 (a) and 1.6 (b), respectively.
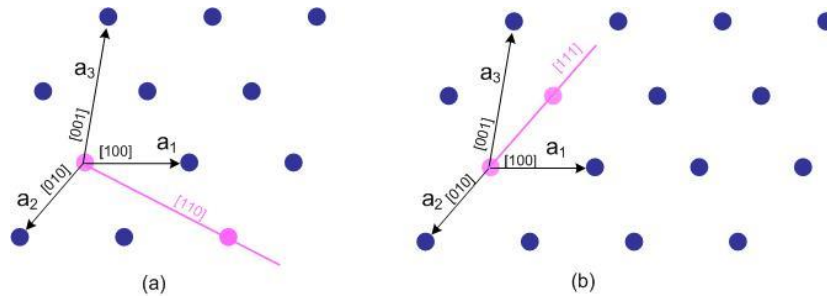
Figure 1.6 *Different axial orientations in an arbitrary array of atoms.*

A planar orientation is a family of planes whose intercept is proportional to the length of 1/k, 1/l and 1/m on unit vectors $\boldsymbol{a}_1$, $\boldsymbol{a}_2$ and $\boldsymbol{a}_3$. The interplanar spacing is defined also by the Miller indices and can be calculated for a specified crystal system type. Crystallographic planes are usually denoted using round brackets, as (k l m). In figure 1.7 (a) and (b) examples of (010) and (111) planar orientations are presented.
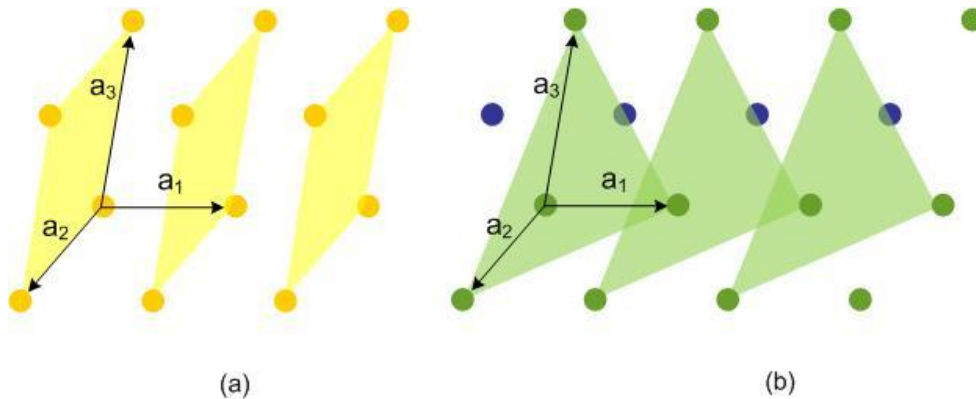
Figure 1.7 *Schemes of planar orientations in a crystal: (010) and (111) in (a) and (b).*

The crystal potential of an axial orientation is defined by the distance between the atoms in the raw. The planar potential is given by the total field created by the family of planes of a specific orientation. Therefore, it depends on the arrangement of the atoms in the plane and on the interplanar distance. Examples of axial and planar averaged potentials of Si and Ge crystals have been simulated in [1.30 – 1.32] using Doyle-Turner approximation.

1.2.2 Ion motion in a crystal

An ion penetrating in a crystal feels the periodic structure of the potential and can be captured to a specific oscillating motion along the crystal channel, i.e. around a crystallographic axis or between two crystal planes. This phenomenon is called "channeling".

There are two kinds of channeling motion: axial and planar channeling. The axial channeling is a one-dimensional example of this phenomenon. A scheme of the axial channeling motion of a projectile is presented in figure 1.8 (a). The particle moves along one single row of atoms in Z direction and oscillates in two other directions X and Y. The planar channeling is a two-dimensional case, when the projectile particle interacts with the planar potential field oscillating between two atomic planes of a crystal. The projectile particle moves in Z direction with oscillations perpendicular to the crystal planes (figure 1.8 (b)). The particles following such trajectories are called "channeled" particles. The trajectory of the channeled particle is strongly affected by the potential energy of the crystal and can be described by solving the equation of motion [1.33].
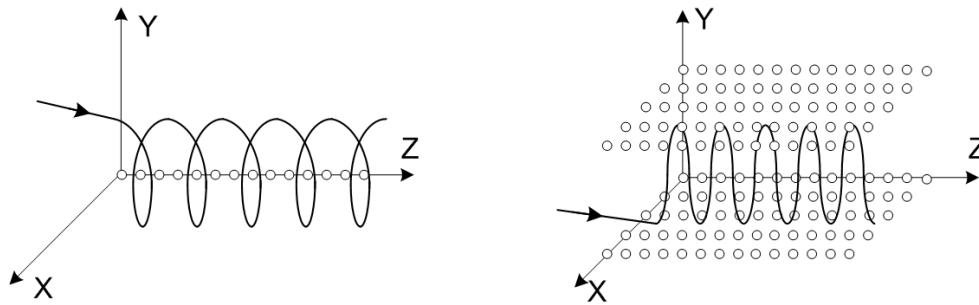
Figure 1.8 *Schematic representation of the channeling motion: (a) axial channeling trajectory along a single crystal axis; (b) planar channeling trajectory between two crystallographic planes.*

The channeling phenomenon occurs only when the particle incident angle θ is smaller than, the critical channeling angle θ_c, called Linhard's angle [1.33]:

$$\theta_c = \sqrt{E_\perp/E},\tag{1.19}$$

where $E_\perp = E\theta^2/2 + ZeV_{max}$ is a transversal energy of the projectile defined by the projectile kinetic energy E and charge Z and by the depth of the crystal potential well V_{max}.

If $\theta << \theta_c$, the particle will not have enough transverse energy $E_\perp$ to surmount the potential barrier and will be trapped in the transverse potential well. Thus, for a particle to be channeled, its entrance angle θ must be such that its transverse energy should be of the order magnitude of the continuum axial or planar crystal potential. Under these conditions a particle

will be guided (steered by the potential) along the crystal channel. Therefore, for an occurrence of the channeling phenomenon of charged particles in a crystal certain values of the incident angle and incident energy must be satisfied.

On the other hand, if $\theta > \theta_c$, the penetrating particle will have too large transverse energy $E_\perp$ to be trapped in the channel and will be free to move across the crystal. This is so-called non-channeling motion.

The oscillating trajectory at the channeling conditions is caused by the projectile scattering on the valence electrons of the crystal atoms, whereas close collisions with nuclei of the target atoms are suppressed.

A concept about continuous potentials of axes and planes and the channeling theory has been developed by J. Lindhard [1.33]. Many aspects of fast ions channeling physics were reported in the monograph of M.A. Kumahov and G. Shimer [1.34]. The majority of theoretical works about channeling radiation has been based on the concept of continuous potentials of axes or planes of the crystal forming a trajectory or wave function.

1.2.3 Resonant coherent excitation of ions

A projectile ion passing a crystal-target with a velocity $\mathbf{v}$ can be coherently excited by the crystal potential. When the frequency ν_{field} of the crystal field seen by the projectile is equal to the frequency ν_{ij} of the transition from the state i into j in the ion, a Resonant Coherent Excitation (RCE) of the ion may occur:

$$\nu_{field} = \nu_{ij}, \tag{1.20}$$

here $\nu_{ij} = E_{ij}/\hbar$, where E_{ij} is the transition energy and $\hbar$ is the Planck constant.

The transition energy in a projectile ion can be found as,

$$E_{ij} = \hbar\nu_{ij}, \tag{1.21}$$

The frequency of the crystal field seen by the projectile moving in the crystal with velocity $\mathbf{v}$ is defined as:

$$\nu_{field} = \frac{\gamma\mathbf{v}}{d}, \tag{1.22}$$

where is γ the Lorentz factor and d is the distance between the atoms of the specific crystal orientation.

Therefore, the resonance condition can written as,

$$E_{ij} = \frac{\hbar\gamma\mathbf{v}}{d} \tag{1.23}$$

In the context of the present thesis, a direct resonant coherent excitation of the projectile ions from the state i to j_1 in a crystal field with ν_{ij_1} frequency is called RCE. When the projectile ions "feel" simultaneously two fields with frequencies ν_{ij_1} and ν_{ij_2} induced by different crystallographic orientations, a Double Resonant Coherent Excitation (DRCE) may occur. The DRCE is a sequential excitation of the projectile ions, first, from the ground state i to the intermediate state j_1 and then, from the j_1 to the higher excited state j_2. The second step of the excitation is possible due to the additional energy transferred to the ion from the third frequency $\nu_{j_1 j_2}$ given by the difference between the frequencies ν_{ij_1} and ν_{ij_2}.

In figure 1.9 RCE (a) and DRCE (b) mechanisms are shown using the example of a one-electron ion, H-like. For instance, an ion can be excited directly from the ground state into the $n = 5$ state by the field with frequency $\nu_{1,5}$. Or the excited $n = 5$ state can be sequentially reached via an intermediate state $n = 2$; this is a DRCE.
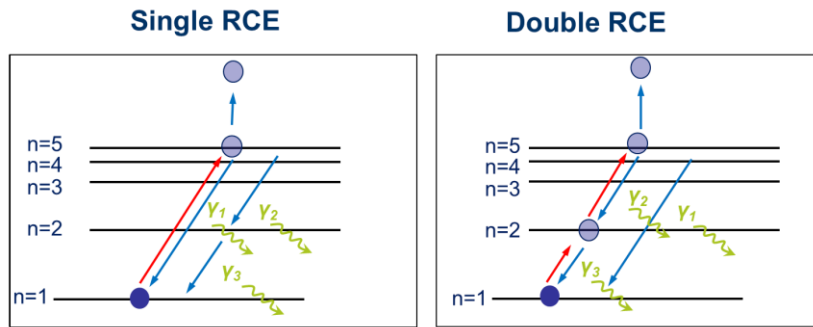
Figure 1.9 *Scheme of an RCE (a) and DRCE (b) in a H-like ion. The different excitation steps are denoted by red arrows and the different decay path of the excited state is denoted by blue arrows.*

1.2.4 De-excitation of the ions

The excited ions can be ionized in random collisions with target atoms or they decay into the ground state via X-ray emission. Generally, the probability of the collisional ionization from the excited state is higher than from the ground state. Therefore, a decrease of the initial charge-state fraction of the ions passing the target is expected at resonance conditions. The occurrence of the RCE can be observed also from the radiative de-excitation by measuring the X-ray emission. The radiative de-excitation rates of the excited states in H-like Ar and the rates of the collisional ionization calculated for Ar at 450 MeV/u are listed in tables 1.2 and 1.3, respectively. The decay rates of the $2p\ ^2P_{1/2}$ and $2p\ ^2P_{3/2}$ states are taken from [1.35] and the decay rates of the higher states, $n = 3$, 4, and 5, are calculated using the classical approximation [1.36] omitting the fine structure. The collisional ionization was calculated by the RICODE (Relativistic Ionization CODE) considering randomly oriented crystal-target, neglecting the density effects of the target [1.13].

Typically, an RCE is indicated from the sharp decrease of the initial charge-state fraction of the ion passing the target. The detection of the photon emitted from the decay of the excited state may help to distinguish RCE from DRCE. The theory shows that the collisional ionization from the excited states and radiative decay of the $n = 2$ states in highly-charged relativistic Ar projectiles occur with probabilities of the same order of magnitude, hence, both processes are experimentally measurable. Nevertheless, there are some experimental aspects recommending non-coincident accumulation of the ion and X-ray yields (see chapter 2).

The calculated transition rates of the excited states in He-like Ar are presented in table 1.4. The decay rates of the 1s2p states are taken from [1.37] and the decay rates of the $n = 3$ state, are calculated using the classical approximation [1.36] omitting the fine structure.

Table 1.2 *Calculated decay rates of the excites states in Ar^{17+} [1.35]*

Transition	Decay rate, s^{-1}
2p ^{2}P$_{1/2}$ → 1s ^{2}S$_{1/2}$ (E1)	6.5935×10^{13}
2p ^{2}P$_{3/2}$ → 1s ^{2}S$_{1/2}$ (E1)	6.5538×10^{13}
3p → 1s ^{2}S$_{1/2}$ (E1)	6.89×10^{12}
4p → 1s ^{2}S$_{1/2}$ (E1)	1.62×10^{12}
5p → 1s ^{2}S$_{1/2}$ (E1)	5.29×10^{11}
3s → 2p (E1)	4.78×10^{12}
4s → 2p (E1)	9.68×10^{11}
5s→ 2p (E1)	2.96×10^{11}

Table 1.3 *Collisional ionization rates in Ar^{17+} in 1 µm Si-crystal [1.13]*

State	Ionization probability at 450 MeV/u, s^{-1}	Ionization probability at 390 MeV/u, s^{-1}
1s	4.36×10^{13}	4.44×10^{13}
2p	9.12×10^{13}	9.34×10^{13}
2s	1.20×10^{14}	1.22×10^{14}
3p	1.56×10^{14}	1.60×10^{14}
3d	1.53×10^{14}	1.56×10^{14}
3s	2.02×10^{14}	2.07×10^{14}
4p	2.14×10^{14}	2.22×10^{14}
4s	2.75×10^{14}	2.86×10^{14}
4d	2.08×10^{14}	2.16×10^{14}
5p	2.37×10^{14}	2.44×10^{14}
5s	3.05×10^{14}	3.17×10^{14}
5d	2.31×10^{14}	2.40×10^{14}

Table 1.4 *Calculated transition probabilities in Ar^{16+} [1.37]*

Transition	Decay rate, s^{-1}
1s2p ^{3}P$_1$→ 1s^2 S$_0$ (E1)	1.82×10^{12}
1s2p ^{1}P$_1$→ 1s^2 S$_0$ (E1)	1.07×10^{14}
1s3p → 1s^2 S$_0$ (E1)	5.48×10^{12}
1s3p→ 1s2p (E1)	3.80×10^{12}

Table 1.5 *Collisional ionization probability in Ar^{16+} in 1 µm Si-crystal at 381 Mev/u [1.13]*

State	Ionization probability at 381 MeV/u, s^{-1}
1s	1.01×10^{14}
2p	1.04×10^{14}
2s	1.36×10^{14}
3p	1.77×10^{14}
3d	1.72×10^{14}
3s	2.28×10^{14}

In the case of excited He-like projectiles, a de-excitation via collisional ionization or radiative decay takes place too. The calculated probabilities of the collisional ionization from different states in He-like Ar at 381 MeV/u are listed in table 1.5.

The probability of the collisional ionization from the 1s2p excited state in Ar^{16+} and the probability of the radiative decay from this excited state into the ground state are comparable. Therefore, the occurrence of the RCE in Ar^{16+} into the 1s2p state can be seen experimentally from the variation of the X-rays and the charge-states yields.

1.2.5 Alignment of the magnetic substates of He-like and H-like ions

The population of the magnetic substates of the ions coherently excited in a crystal target can be controlled by the polarization direction of the oscillating crystal field.

The X-ray radiation direction from the decay of an excited state into the ground state in He-like ions is characterized by the orbital angular momentum of the excited state (neglecting the electron and the nuclear spin). The probability of the $1s^2 \rightarrow 1s2p$ electric dipole transition is determined by the squared transition matrix element:

$$P_{1s^2 \rightarrow 1s2p} = |\langle 1s^2|\mathbf{F'}\mathbf{d}|1s2p\rangle|^2, \tag{1.24}$$

where $\mathbf{d} = \langle 1s^2|e\,\mathbf{r}|1s2p\rangle$ is the effective dipole moment and $\mathbf{r}$ is the position operator. $\mathbf{F'}$is the electric crystal field in the rest frame of the ions.

According to the Lorentz transformation [1.38] from the laboratory system (ct, x, y, z) into the rest frame of the relativistic ions (ct', x', y', z') moving with a velocity $\boldsymbol{v}$ in Z direction:

$$ct' = \gamma(ct - \beta \cdot \mathbf{r})$$

$$\mathbf{r'} = \mathbf{r} + \frac{\gamma^2}{\gamma + 1}(\beta \cdot \mathbf{r})\beta - \gamma\beta c \tag{1.25}$$

The Lorentz transformation for electromagnetic field is written as,

$$\mathbf{F'} = \gamma(\mathbf{F} + c\beta \times \mathbf{B}) - \frac{\gamma^2}{\gamma + 1}\beta(\beta \cdot \mathbf{F})$$

$$\mathbf{B'} = \gamma\left(\mathbf{B} - \frac{\beta}{c} \times \mathbf{F}\right) - \frac{\gamma^2}{\gamma + 1}\beta(\beta \cdot \mathbf{B}) \tag{1.26}$$

Using a general expression for the crystal potential under the Moliere approximation [1.39] the electric field will be defined as,

$$\mathbf{F} = -\nabla V(\mathbf{r}) = \sum_{\mathrm{g}} 2\pi i\boldsymbol{g}\, V_{\mathbf{g}} \exp(-2\pi i\mathbf{g} \cdot \mathbf{r}) \tag{1.27}$$

Where $g_{k,l,m} = ka_1^* + la_2^* + ma_3^*$ is a reciprocal lattice vector and k, l and m are the Miller indices. The factor $V_{\mathbf{g}}$ is the Fourier coefficient of the potential $V(\mathbf{r})$. The vectors a_1, a_2 and a_3 are the unit vectors coinciding with the $[\bar{1}10]$, $[001]$ and $[110]$ axes of the Si crystal, respectively (see figure 1.10 (a)).

The coordinate system XYZ showed in figure 1.10 (a) is chosen in such a way that the ions move along Z axis. With green and yellow the (220) and (004) crystal planes are indicated. A relation of the XYZ system to the detectors alignment is represented in figure 1.10 (b).
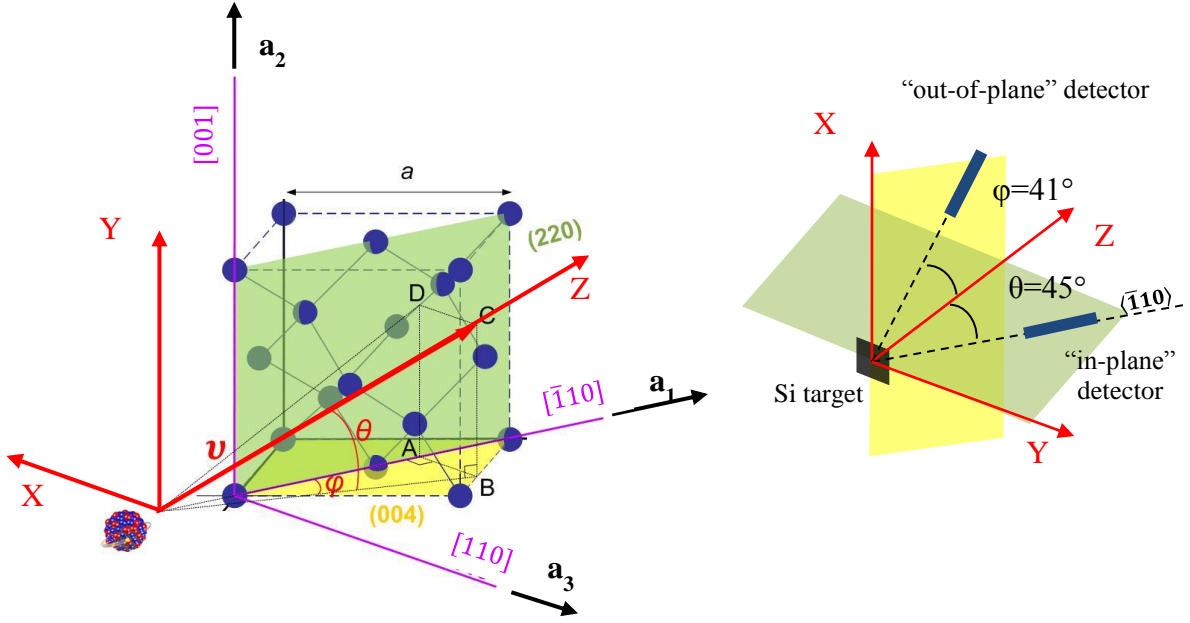
24

Figure 1.10 (a) *Si crystal unit cell; (b) the X-ray detectors alignment.*

The electrical field $\mathbf{F}'$ of the crystal in the rest frame of the ions can be defined by substituting the expressions for the vector $\mathbf{r}$ obtained from (1.25) and for the electric field $\mathbf{F}$ (1.27) into (1.26). We consider the case of purely electric crystal field when $\mathbf{B} = 0$.

$$\mathbf{F}'(\mathbf{r}', t') = \sum_{\mathbf{g}} 2\pi i g \, V_{\mathbf{g}} \left(\mathbf{g} - \frac{\gamma}{\gamma + 1} (\mathbf{g} \cdot \beta)\beta \right) \times \exp[-2\pi i \mathbf{g} \cdot \mathbf{v} t']$$
$$\times \exp\left[-2\pi i \mathbf{g} \cdot \left(\mathbf{r}' + \frac{\gamma^2}{\gamma + 1} (\beta \cdot \mathbf{r}')\beta \right) \right] \tag{1.28}$$

Assuming that the ions move along the Z axis, the electric field components normal to ions velocity $\mathbf{v}$ are multiplied by γ, while the parallel components are not affected by the motion of the coordinate. Therefore, the amplitude vectors of the electric field in the rest frame of the ions are:

$$|\mathbf{F}_x'| = \gamma |\mathbf{F}_x| = 2\pi V_{\mathbf{g}} \gamma g_x$$

$$|\mathbf{F}_y'| = \gamma |\mathbf{F}_y| = 2\pi V_{\mathbf{g}} \gamma g_y \tag{1.29}$$

$$|\mathbf{F}_z'| = |\mathbf{F}_z| = 2\pi V_{\mathbf{g}} g_z$$

Thus, the polarization direction of the oscillating crystal field is parallel to the vector $(\gamma g_x, \gamma g_y, g_z)$. The probabilities of the excitation into different magnetic substates 1s2p are proportional to the squared amplitudes of the correspondent electrical field components:

$$P_{1s2p_x} \sim |\mathbf{F}_x'|^2 = \left(2\pi V_\mathbf{g} \gamma g_x\right)^2$$

$$P_{1s2p_y} \sim |\mathbf{F}_y'|^2 = \left(2\pi V_\mathbf{g} \gamma g_y\right)^2 \qquad (1.30)$$

$$P_{1s2p_z} \sim |\mathbf{F}_z'| = \left(2\pi V_\mathbf{g} g_z\right)^2$$

The components of the reciprocal vector $\mathbf{g}$, g_x, g_y and g_z, can be found using the inverse rotation matrix R_θ^{-1} and R_φ^{-1}:

$$\begin{pmatrix} g_x \\ g_y \\ g_z \end{pmatrix} = R_\theta^{-1} R_\varphi^{-1} \begin{pmatrix} -m a_1^* \\ l\, a_2^* \\ k\, a_3^* \end{pmatrix} =$$

$$\left[\begin{pmatrix} 1 & 0 & 0 \\ 0 & \cos\theta & -\sin\theta \\ 0 & \sin\theta & \cos\theta \end{pmatrix} \times \begin{pmatrix} \cos\varphi & 0 & \sin\varphi \\ 0 & 1 & 0 \\ -\sin\varphi & 0 & \cos\varphi \end{pmatrix} \right] \times \begin{pmatrix} -m \dfrac{\sqrt{2}}{a} \\ l\, \dfrac{1}{a} \\ k\, \dfrac{\sqrt{2}}{a} \end{pmatrix} = \qquad (1.31)$$

$$= \frac{1}{a} \begin{pmatrix} \sqrt{2}k \sin\varphi - \sqrt{2}m \cos\varphi \\ -\sqrt{2} \sin\theta\, (k \cos\varphi + m \sin\varphi) + l \cos\varphi \\ \sqrt{2} \cos\theta\, (k \cos\varphi + m \sin\varphi) + l \sin\theta \end{pmatrix}$$

Here a_1^*, a_2^* and a_3^* are the reciprocal unit vectors.

The ratio between the X-ray emission measured by the "out-of-plane" and the "in-plane" detectors in the present experiments is expected to be:

$$R = \frac{N_{photons"out-of-plane"}}{N_{photons "in-plane"}} = \frac{P_{1s2p_y} + P_{1s2p_z}}{P_{1s2p_x} + P_{1s2p_z}} = \frac{(\gamma g_y)^2 + g_z{}^2}{(\gamma g_x)^2 + g_z{}^2} \qquad (1.32)$$

Assuming θ and $\varphi \ll 1°$:

$$R \approx \frac{2k^2 + \gamma^2 l^2}{2k^2 + 2\gamma^2 m^2} \qquad (1.33)$$

In the case of He-like ions the effect of fine structure were neglected because the spin angular momentum $S = 0$ for 2p states. The spin-orbit interaction modifies the shape and the dynamics of the electronic wave function of the excited states in H-like ions. The intensity distribution of the electric dipole radiation into the ω solid angle is:

$$I(\omega) = 1/2\,(1 - \cos 2\omega) \qquad (1.34)$$

In the geometry of the present experiment (see figure 1.10):

$$\cos \omega_x = \frac{|F'_{gx}|}{|F'_g|} \qquad\qquad \cos \omega_y = \frac{|F'_{gy}|}{|F'_g|} \qquad (1.35)$$

26

The ratio between the "out-of-plane" and "in-plane" X-ray emission is defined then as,

$$R = \frac{N_{photons"out-of-plane"}}{N_{photons"in-plane"}} = \frac{I(\omega_x)}{I(\omega_y)} = \frac{\left(\gamma g_y\right)^2 + g_z{}^2}{(\gamma g_x)^2 + g_z{}^2} \approx \frac{8k^2 + 4\gamma^2 l^2 + 2\gamma^2 m^2}{8k^2 + \gamma^2 l^2 + 8\gamma^2 m^2} \qquad (1.36)$$

2 The experiment

In the present work Resonant Coherent Excitation (RCE) and Double Resonant Coherent Excitation (DRCE) of H-like and He-like Ar ions passing a Si-crystal have been experimentally investigated. This chapter is dedicated to the methods and instrumentation used in the experiments performed at the HIMAC facility in Chiba, Japan.

The beam preparation procedure is discussed in sections 2.1 and 2.2. The experiment set-up is presented in detail in section 2.3. The high-precision goniometer and the target installed in the vacuum chamber are presented here. Section 2.4 reports on the detectors used to measure the charge-state yields of the projectiles and the X-ray emission from the decay of the projectile excited states into the ground state. Details regarding the experimental conditions used to observe the RCE and DRCE in highly-charged ions using a crystal-target are covered in section 2.5.

2.1 The HIMAC facility

The Heavy Ion Medical Accelerator (HIMAC) has been built in Chiba, Japan in 1984 and was the first heavy-ion accelerator dedicated to medicine in the world [2.1]. HIMAC was promoted by the Japanese National Institute of Radiological Sciences (NIRS) and was designed for cancer therapy. To satisfy the medical requirements the accelerator provides beams of H^{q+}, He^{q+}, C^{q+}, O^{q+}, Ne^{q+}, Ar^{q+}, Fe^{q+}, Kr^{q+} and Xe^{q+} ions with different charge-states q in the energy range from 100 MeV/u to 800 MeV/u with intensities up to 2×10^{11} pps (for C). In figure 2.1 a cross-sectional view of the HIMAC is presented. It consist of ion sources, an RFQ (Radio Frequency Quadrupole) and Alvarez-type linacs, two synchrotron rings, high energy beam transport lines, and irradiation facilities for treatment and experiments.
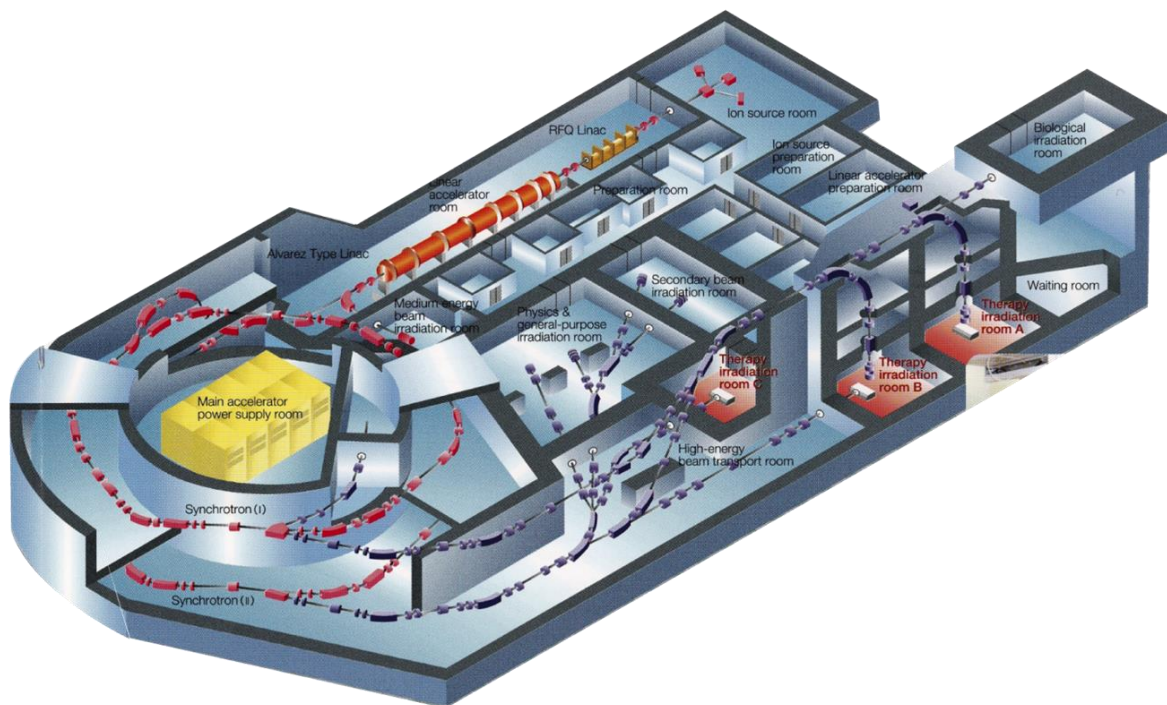

Figure 2.1 *Scheme of the HIMAC facility: ion sources, a sequence of linear accelerators, two synchrotron rings, experimental area and therapy rooms [2.2].*

The injection system of the HIMAC has two types of ion sources: a Penning Ionization Gauge (PIG) and an Electron Cyclotron Resonance (ECR) source. The PIG source is foreseen for a light ions production and the ECR is typically used as a heavy ions source. To match the injection energy of the first acceleration stage, the RFQ linac, of 8 keV the ion sources are put on high voltage platforms, up to 60 kV.

2.1.1 The linear accelerator

The first acceleration stage of the ions after living the source is a conventional four-vane type RFQ linac. The RFQ parameters are presented in table 2.1.

Table 2.1 *The RFQ linac specifications*

Specifications	
Operation frequency	100 MHz
Input / Output energy	8 / 800 keV
Charge-to-mass ratio	1/7
Transmission efficiency	0.92
Number of unit cells	300
Acceptance	145 πmm·mrad
Normalized acceptance	0.6 πmm·mrad

The RFQ linac is followed by the Alvarez-type linear accelerator which consists of three independent cavities and each cavity is fed with an RF power of about 1MW peak. The Alvarez linac tank is in total 24 m long, and consists of 106 unit cells. The Alvarez linac is separated into four tanks longitudinally.

Table 2.2 *The Alvarez linac specifications*

Specification	Tank 1	Tank 2	Tank 3
Synchronous phase	30°	30°	30°
Ion energy	0.8-2.669 MeV	2.669-4.385 MeV	4.385-6.060 MeV
Tank length	9.768 m	7.202 m	6.907 m
Acceleration rate	1.34 MeV/m	1.67 MeV/m	1.7 MeV/m
Tank diameter	2.20 m	2.18 m	2.16 m
Drift tube diameter	16 cm	16 cm	16 cm
Drift tube length	9.85-16.45 cm	17.99-21.72 cm	22.9- 25.73 cm
Number of the unit cells	56	28	22
Acceptance	67π mm·mrad	-	-
Normalized acceptance	2.8π mm·mrad	-	-

At the end of the Alvarez linac a 100 μg/cm^2 carbon stripper foil is installed in order obtain high charge-states of the ions. The ion beams, supplied by the linear accelerator system (at 6.060 MeV/u) are further injected into the one of the synchrotron rings.

2.1.2 The synchrotron accelerator

The synchrotron of the HIMAC facility consists of two rings located at the lower and upper underground flours at 7 m distance in vertical direction. The rings are operating independently from each other in order to provide two different beams in the same or in different therapy rooms. The main parameters of the synchrotron are listed in table 2.3.

Table 2.3 *The synchrotron parameters*

Specifications	
Injection energy	6 MeV/u
Output energy	100 MeV/u – 800 MeV/u
Maximum intensities for light ions	10^{11} ppp
Repetition rate	0.3 – 1.5 Hz
Charge-to-mass ratio	0.5
Vacuum	$5 \cdot 10^{-9}$ Torr

Both rings are identical and supply H^{q+}, He^{q+}, C^{q+}, O^{q+}, Ne^{q+}, Ar^{q+}, Fe^{q+}, Kr^{q+} and Xe^{q+} ions with different charge states q in the energy range from 100 MeV/u to 800 MeV/u. Each synchrotron consists of 12 dipole magnets, 12 focusing quadrupole magnets and 12 defocusing quadrupole magnets. The two rings have a multiturn injection channel and slow extraction channels.

The upper ring is designed to have also a fast extraction channel and the lower ring has a fast injection channel to receive the ions accelerated by the upper ring. The extraction beam system [2.1] transports slowly extracted ions from each ring to the High Energy Beam Transport (HEBT) system where the fine beam tuning is done before delivering the accelerated highly-charge ions to the experimental area or the therapy rooms.

2.2 The ion beam

For the present experiments relativistic beams of H-like and He-like Ar ions have been supplied by the HIMAC facility. Ar^{8+} ions have been accelerated up to 6 MeV/u by the sequence of linacs (RFQ and Alvarez type) and striped to H-like or He-like charge state passing a 100 mg/cm^2 C foil at the end of the Alvarez linac, before the injection into the synchrotron. The ions, accelerated by the synchrotron up to the requested energy, are extracted from the ring and transported via High Energy Beam Transport (HEBT) system to the experimental area.

The present experiments require a narrow, parallel ion beam to satisfy the resonance conditions. Due to radiation therapy needs the HEBT is equipped with numerous beam profile monitors and steering magnets in order to provide precise beam positioning on a target. The narrow beam was prepared by passing a lead collimator in the beam line. The collimator, with a diameter of about 6 mm, was placed at the entrance of the target chamber. Figure 2.2 shows the beam profile registered by a fluorescence screen placed at 10 mm in front of the crystal target.
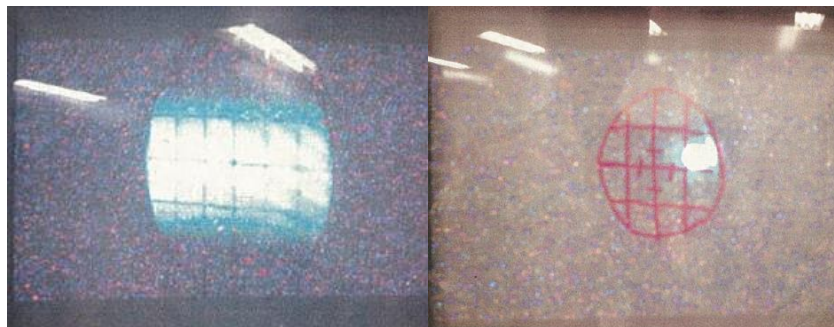

Figure 2.2 *Profile of Ar ion beam on a fluorescent screen installed before the target, inside the vacuum chamber: left – without collimator, right – with collimator.*

The maximum beam intensity of about 3×10^8 ppp was used for the X-ray measurements and for the ion charge-state measurements the intensity has been reduced to 10^5 ppp due to the limitations of the particle detector.

2.3 The setup

In the present experiment the interaction of the highly-charged Ar ions with the Si-crystal was studied by measuring the projectile X-ray emission and the charge-state distribution of the ions after passing the target.

The scheme of the experimental setup is shown in figure 2.3. A Si-crystal target was mounted perpendicular to the beam direction in the support of a 5-axis goniometer under vacuum. The goniometer allows the alignment of the target relatively to the beam direction in such a way that the resonant conditions for the ion excitation can be found with high precision.
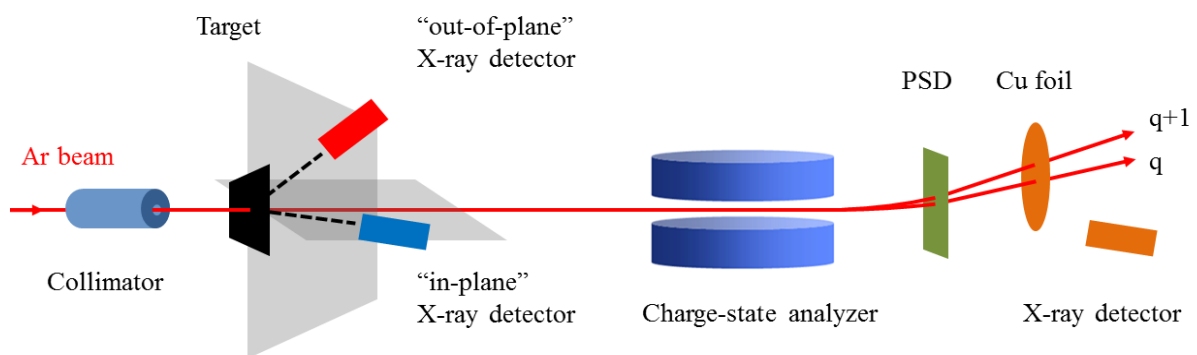

Figure 2.3 *The scheme of the experimental setup: placement of the "in-plane" and "out-of-plane" X-ray detectors and Position Sensitive Detector (PSD).*

Photons emitted from the target and projectile ions were registered by solid state silicon detectors installed "in-plane" and "out-of-plane" behind the crystal-target, inside the goniometer vacuum chamber. The projectile ions, after passing the crystal, are transported by a dipole magnet installed behind the goniometer chamber, and their different charge-states crated in the crystal are separated accordingly. At the end of a 5 m long flight path, the ions are detected by a two-dimensional position sensitive silicon detector. Due to the fact that for high beam intensities the particle detector cannot be used for beam monitoring (see section 2.4) at the end of the beam line a copper foil was installed. Ions passing the foil excite the Cu atoms and the resulting X-ray yield is proportional to the intensity of the penetrating ion beam. Emitted photons from the foil were measured by a third X-ray detector and used for a relative normalization of the RCE photons accumulated during different time intervals. The normalization also corrects possible variations in the beam intensity.

2.3.1 The vacuum chamber

A custom stainless steel chamber, designed for the RCE experiments, was installed in the beam line. The vacuum chamber, 59 cm height and 67 cm diameter, was mounted on a stainless steel frame which provides access inside of the chamber trough the opening in the bottom of the chamber. The exact position of the chamber relatively to the beam axis has been adjusted using a telescope. The goniometer is fixed on the upper flange of the chamber. The numerous ports though the wall of the chamber are used for the cabling of the detectors and electronics installed inside the chamber, for the vacuum pump and as a view port inside the chamber. A picture of the vacuum chamber is presented in figure 2.4
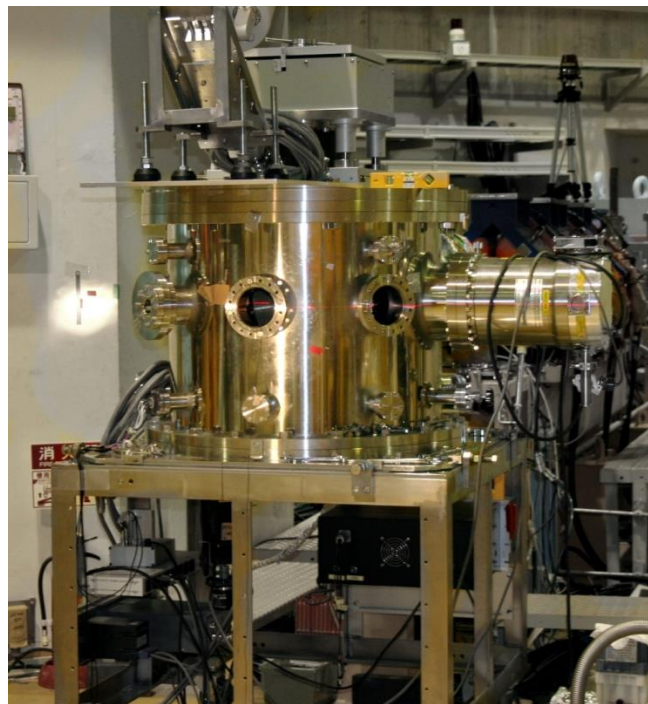

Figure 2.4 *The goniometer vacuum chamber.*

2.3.2 The high precision goniometer

The goniometer is essential for the precise alignment of the target-crystal relatively to the beam direction. The resonance conditions are found in these experiments by careful tuning of the crystal position instead of changing the ion energy.

The goniometer has five moving axes. The different axes are driven by independent step motors. The motor stepping is transformed in the movement along or around the three axes by a combination of different screw-like shafts.

The goniometer moves the target in five directions: it can be translated along X and Y directions (perpendicular to the beam direction) and it rotates around X, Y and Z axes; these

rotations are φ, θ, and ω angles (see figure 2.5). Axis Z coincides with the beam direction. Accecible ranges are listed in table 2.4.
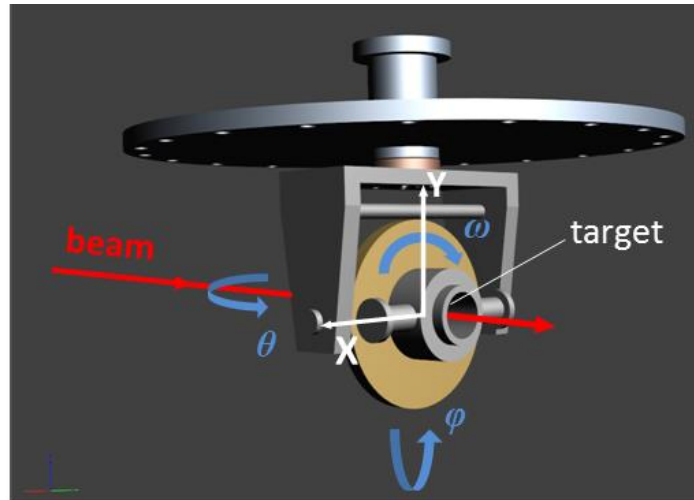

Figure 2.5 *Scheme of the possible target translations and rotations using the goniometer.*

Table 2.4 *Motion range of the goniometer*

	X-axis	*Y*-axis	θ	φ	ω
Range	± 20 mm	± 20 mm	360°*	360°*	± 5°

*In reality the range is limited by the geometrical orientation of the detectors installed inside the chamber and the available free space.

The accuracy of rotation and translation movements is different from one axis to the other and is given by the resonant conditions. In principle, the accuracy of the goniometer steps should be at least of the same order as the momentum distribution of the ion beam and it`s divergence. The energy spread $\Delta E/E$ was about 2.4×10^{-4} [2.1].

The translation made by the step motor in mm or degrees along the five axes is performed by the encoders RON 806. The angular encoders are based on light transmission through periodic grating patterns made of gold on glass plates and are installed in the vacuum chamber. The goniometer motors and the encoders are controlled by a Visual C++ based program which runs on a PC under Windows 2008. During the experiment the goniometer is remotely controlled from outside the cave. The goniometer controller is connected to the data acquisition program.

After the rough adjustment of the goniometer using the telescope, the target position, should be defined precisely. This is done by the identification of a known planar crystal orientation by fine scanning of θ and φ angles (see details in section 2.5)

2.3.3 Si-crystal target

In the present work a silicon crystal-target was used. In figure 2.6 the unit cell of a Si crystal is denoted with solid circles. Si crystal is a diamond-like, cubic system type. In this case, the lattice vectors **a** are orthogonal and of equal length. The lattice system of the Si-crystal is formed by two face-centered Bravias lattices interpenetrating in such a way that the second lattice (marked with green in figure 2.6) is shifted relatively to the first one (marked with blue in figure 2.6) along its main diagonal with a distance equal to the quarter of this diagonal. The lattice of a silicon crystal can be considered as face-centered structure with four additional atoms, situated in the centers of the four quarters of the cub volume.
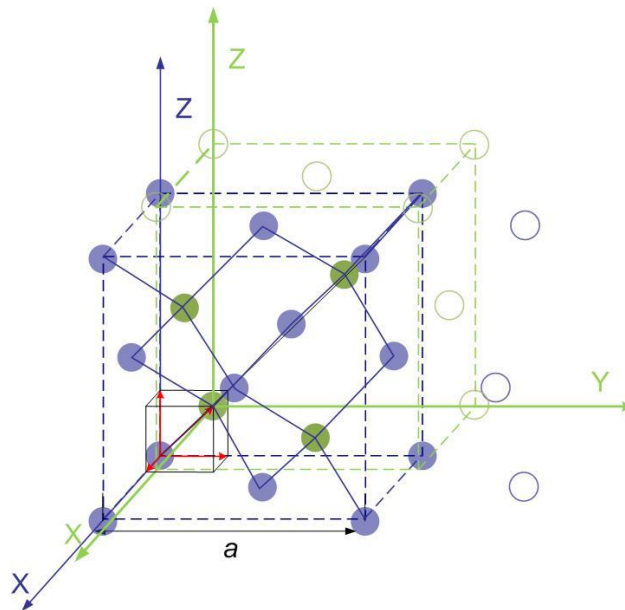

Figure 2.6 *Schematic representation of the Si-crystal unit cell formed by two interpenetrating lattices marked with blue and green colors. The bounds between the atoms are represented by solid blue lines.*

The crystal used in the experiments was produced by the Virginia Semiconductor Incorporated (VSI) [2.3]. The target, 1 μm thick, was mounted on a square aluminum frame and fixed with a drop of silicon vacuum grease (figure 2.7). This frame is mounted on a circular support. Finally the support was fixed on the goniometer under 45 degrees in the azimuthal direction (φ angle in figure 2.5). Therefore the effective target thickness is about 1.4 μm. The target should be thin in order to reduce the energy loss and angular straggling of the penetrating ions which destroy the coherence, especially at the non-channeling conditions. On the other hand, it should be enough thick to induce excitation of the projectile ions. The thickness of 1 μm was chosen according to the previously performed experiments with Ar ion passing a Si crystal.
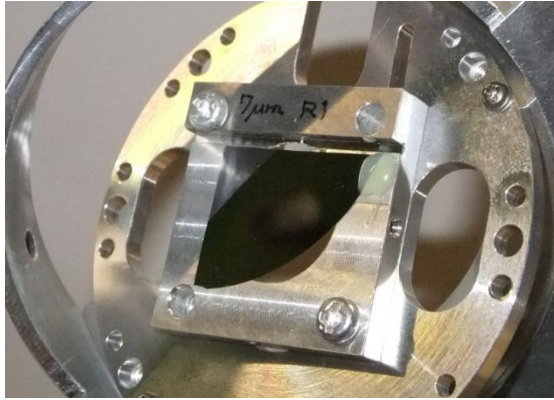
Figure 2.7 *Si-crystal mounting frame.*

The circular target support is foreseen also with three large holes which allow the beam adjustment with and without target. The target support and frame are made of aluminum to avoid producing additional X-ray background by accidentally hitting the frame with the ion beam.

2.4 Detection

In this section the instrumentation used for the detection of the X-ray and the heavy ions penetrating the Si-crystal target are described. The working principle, construction and operation mode of the detectors used in the present work will be presented.

2.4.1 Silicon Drift X-ray Detector (SDD)

The detectors used for the "in-plane" X-rays direction and for the beam monitoring are solid state Silicon Drift Detectors (SDDs) produced by Ketek GmbH company [2.4]. The main feature of this detector type is its cooling. The "Ketek" detectors can operate at room temperature and do not need liquid nitrogen for cooling. This gives the possibility to install the detectors also inside the vacuum chamber, close to the photon emission point.

The "Ketek" SDD consists of a 80 mm^2 large and 450 μm thick high purity n-type silicon crystal with a very low leakage current. In figure 2.8 the Si-crystal (a) and the associated electronics (b) are shown. The detector crystal is mounted under vacuum and is separated from the atmosphere by a 25 μm thick beryllium window.
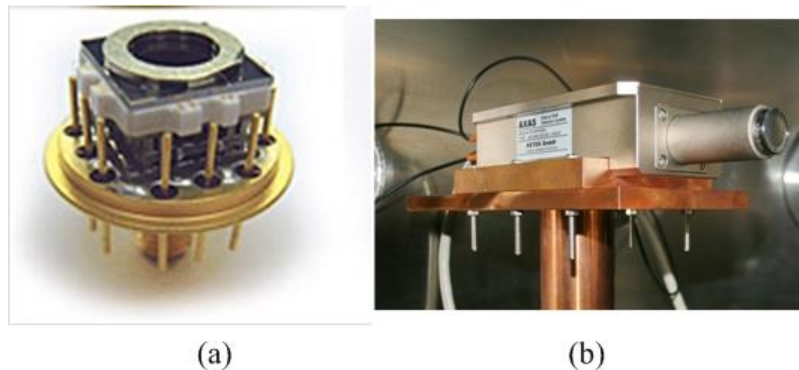

(a)   (b)

Figure 2.8 *The "Ketek" Silicon Drift Detector: (a) the Si-crystal, (b) the detector body on the copper support*.

The internal geometry of a SDD is shown in figure 2.9. The detector has two electrodes: a cathode on one side (red in the drawing) and a small-size collecting anode on the other side (dark blue). The cathode is made out of a thin gold foil (about 100 Å) to avoid absorption and scattering of the photons. The anode is surrounded by increasingly-reverse biased field stripes (red rings in the drawing) which generate an electric field with a strong component parallel to the device surface. The device is covered by guard rings used for the isolation (green rings in the drawing).

The detector crystal (yellow in figure 2.9) becomes fully depleted by applying a negative bias voltage to both sides of the detector. The radiation enters the detector from the

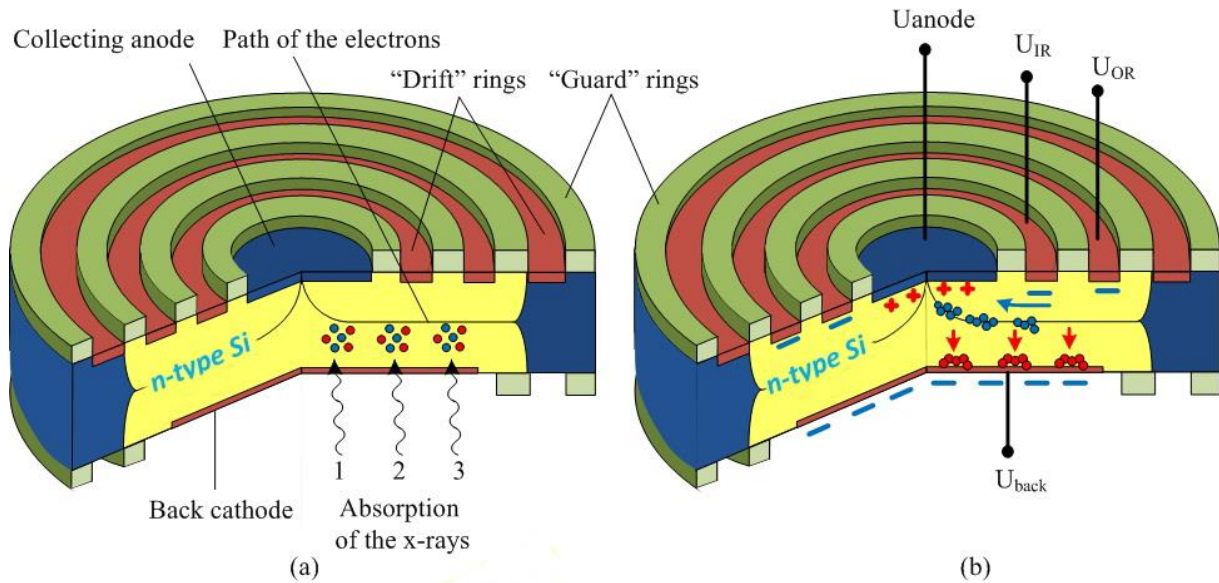cathode side. When a photon hits the crystal atoms, photoelectrons are knocked out from the silicon atoms.

Figure 2.9 *Geometry and operation of the silicon drift detector: (a) radiation absorption; (b) charge collection by applying voltage on the anode (U_{anode}) and cathode (U_{back}) and on the "drift rings" in such way that voltage on the inner ring is higher than voltage on the outer ring ($|U_{IR}| < |U_{OR}|$).*

The cloud of electron-holes pairs generated in a depleted detector volume is separated under the internal electrical field. The positively charged holes are travelling directly to the cathode. The electrons will travel towards the anode along a path which corresponds to their potential minimum defined by the value of the voltages on the electrodes on both sides of the crystal. This provides a certain delay in time for the signals created by the particles hitting the detector on larger distances from the anode (In figure 2.9 (b)). Thus, the "drift" concept reduces the dead time of the detector.

The measurement of the photon energy by this detector is based on the proportionality between its energy and the charge collected at the anode. The detector shows about 200 eV energy resolution at about 5 keV (see chapter 3).

The "in-plane" detector was mounted on a copper support which gives a possibility to place the detector at 170, 180 or 190 mm distance from the target and under different observation angle, inside the vacuum chamber. In the present experiments the detector was installed at 170 mm distance to the target and at 41° relatively to the beam direction. Thermal grease was used for a better thermal contact between the detector body and the support. The heat produced by the detector, was transferred through the copper support to the bottom of the chamber (figure 2.10).

40

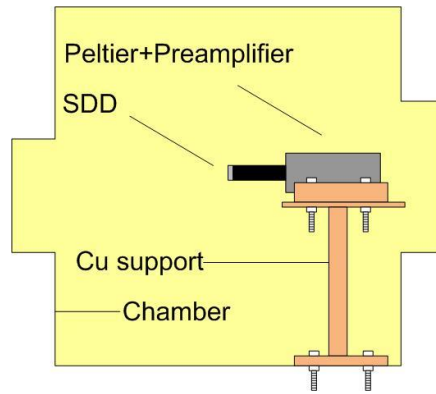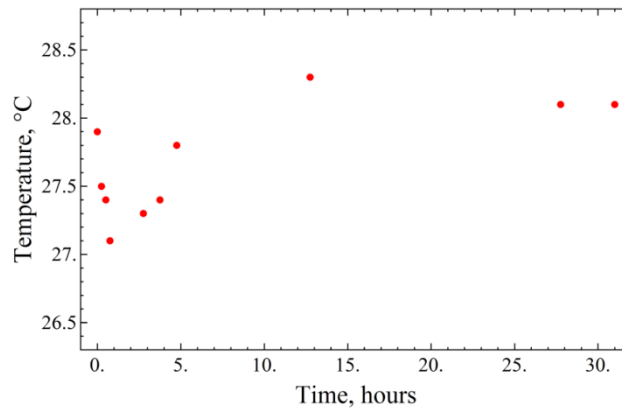Figure 2.10 *The scheme of SDD mounting in the vacuum chamber*

Figure 2.11 *Temperature on the SDD detector during the experiment*
.

The detector temperature was monitored during the experiment with a thermocouple. The results presented in figure 2.11 show only 1 degree variation of the detector temperature during 30 hours operation in vacuum which does not affect the detector parameters (noise level, energy resolution).

2.4.2 Lithium-Drifted Silicon X-ray Detector

For the measurement of the X-rays emitted from the crystal-target in "out-of-plane" direction a PGT LS30135DS Lithium-Drifted Silicon Detector (SiLi) was used [2.5]. The detector consists of a 6 mm thick silicon-lithium diode with an active area of 30 mm^2, separated from the atmosphere by 8 μm beryllium window.

The scheme of a "SiLi" detector is shown in figure 2.12. The detector crystal is a silicon semiconductor having a compensated intrinsic i-type region sandwiched between p-type and n- type regions. The compensated region is produced by diffusion of lithium into p-type silicon. The lithium compensates impurities and dopants already present in the crystal. The detector has two electrodes: a cathode (blue in the figure) on the side where the radiation enters and an anode (red in the figure) on the opposite surface.
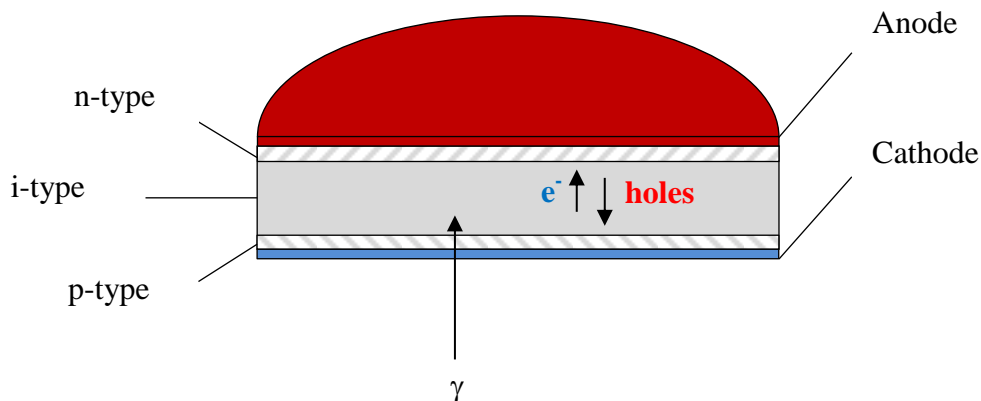

Figure 2.12 *Scheme of the "SiLi" detector.*

The radiation enters the detector from the p-type layer side. This layer called the "dead layer", is thin and does not contribute to the detection process directly. The radiation sensitive volume of the detector is the compensated i-type layer. When a reverse-bias potential is applied across the detector, the compensated zone becomes depleted of electron-hole free-charge carriers, the electrons and holes being drawn to the p-type and n-type regions, respectively [2.6]. This provides a higher resistivity of the detector material which improves the detection resolution and expands the detection energy range by means of increasing the detector thickness. This detector has about 200 eV energy resolution at about 5 keV (see chapter 3).

A disadvantage of such a detector is a thermally generated leakage current which can create a significantly high noise. Therefore, the detector-crystal has to be cooled with liquid nitrogen.

The geometry of the experiment allows to install the "SiLi" detector from the top of the goniometer vacuum chamber. The detector tip was mounted inside the chamber through a vacuum sealed flange, under 45 degrees observation angle relative to the beam axis (figure 2.13).

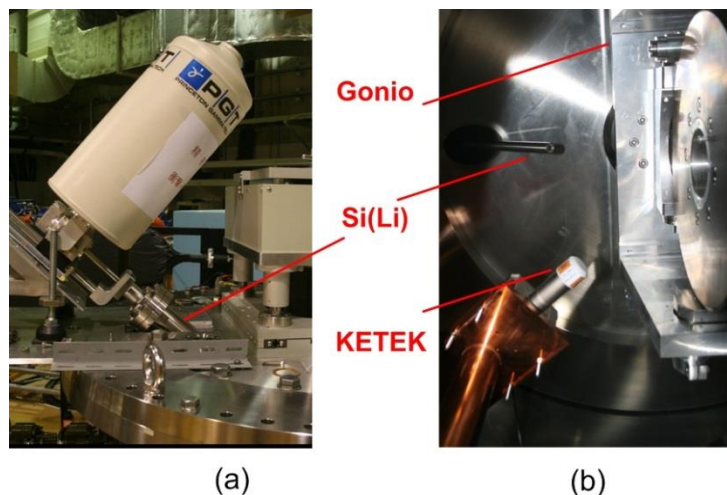Figure 2.13 *The "SiLi" detector installed in the goniometer vacuum chamber: (a) the detector seen from outside; (b) "SiLi" and "SDD" detectors placed around the target in the chamber*

Unfortunately, during one of the performed experiment this detector did not work properly. Due to the very high level of noise it was not possible to distinguish any line in the region of interest of the spectrum.

2.4.3 Ion detection

The charge-state distribution of the ions was measured with a two-dimensional position sensitive silicon DL400-7 detector produced by the First Sensor Technology GmbH [2.7]. This is a square p–i–n -type diode with an active area of 400 mm^2.

The radiation sensitive layer, the i-type silicon, is a lightly doped intrinsic semiconductor. When an incident particle penetrates the i-layer it produces electron-hole pairs. A reverse bias accelerates the charge carriers moving towards the electrodes. The detector has four electrodes on its surfaces: two anodes on the front side and two cathodes on the back side (figure 2.14).
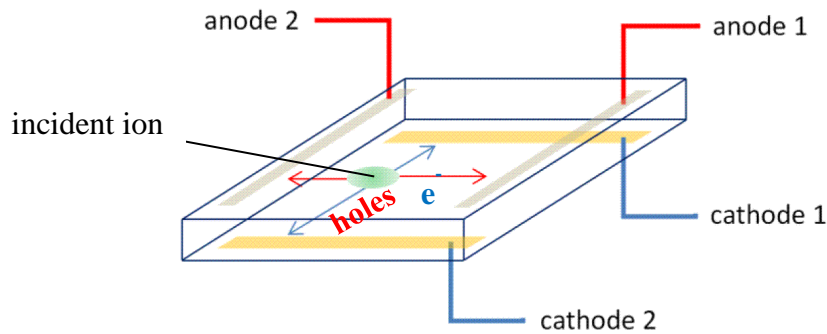

Figure 2.14 *Scheme of the particles detection on the DL400-7 detector [2.7].*

The signal created by the drifting charge is divided into four parts: signals from electrons are collected on the two anodes and signals from holes on the two cathodes. Since the resistivity of the doped layers of the crystal is uniform, the current collected by an electrode is inversely proportional to the distance between the incident position and the electrode. Therefore, using the signals created by the spread charge, one can reconstruct the position of the ion incidence on the detector. The X and Y coordinates are calculated using the charges collected on the cathodes Q_1 and Q_2 and the ones collected at the anodes Q_3 and Q_4:

$$X = \frac{Q_2}{Q_1 + Q_2} \qquad Y = \frac{Q_3}{Q_3 + Q_4}. \tag{2.1}$$

The spatial resolution of the PSD detector was tested offline, before the experiment, using an ^{241}Am α-source and a PCB mask. For this, the detector was installed in the same position as for the experiment, in the beam line, under vacuum. In figure 2.15 the detector with the mask installed in the beam line is shown. The spectrum measured over 30 minutes is presented in figure 2.16. The structure of the mask can be well identified from the performed test measurement.
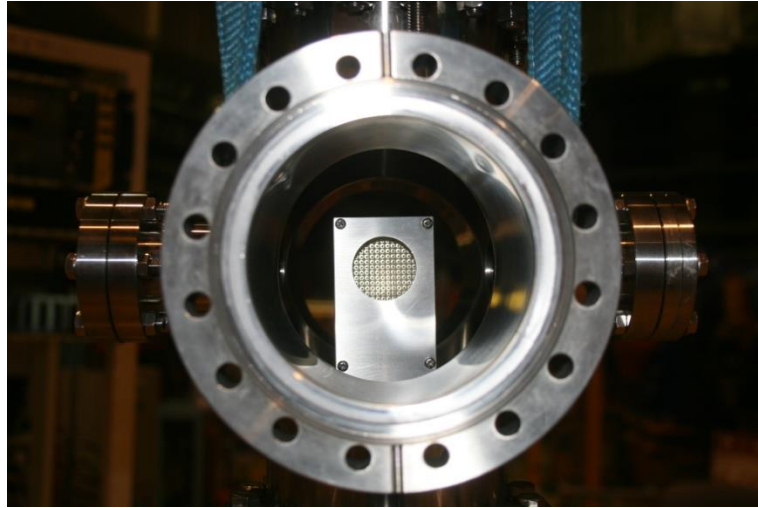
Figure 2.15 *The PSD detector installed with the test mask in the beam line*

The observed deformations around the detector edges are caused by the field distortions. The projections of the 2D spectrum on X and Y axes are shown in the figures 2.16 (b) and (c). From this measurement the position resolution on both direction of about 1 mm was defined. This is more than sufficient for a clear separation of the different charge states in this experiment.

(a)   *(b)*
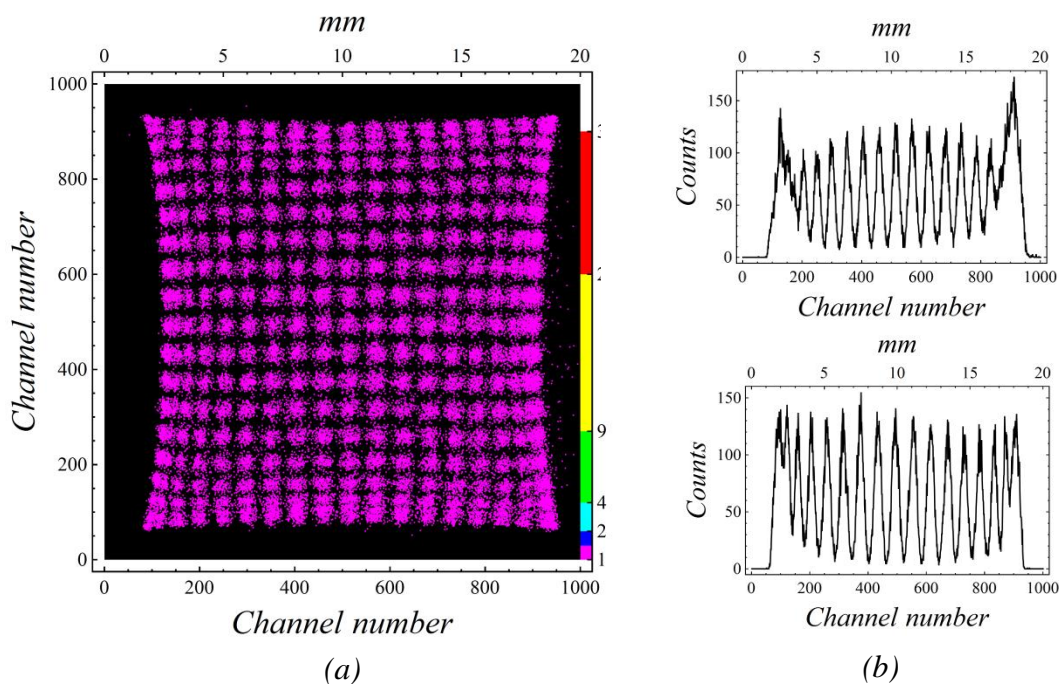
Figure 2.16 *The mask image obtained by irradiation of the PSD detector with an ^{241}Am α-source: (a) two-dimensional image; (b) and (c) are X and Y projections of the two-dimensional image. One channel corresponds to 0.02 mm.*

The detection efficiency of the silicon detector is rate dependent: higher the beam intensity, lower the detection efficiency. Various tests with beams of heavy ions showed that the detection efficiency is 100% for count rates below five thousand ions per second. Due to

the high probability of the RCE process, this count rate permits to perform measurements with good statistic in reasonable time (see chapter 4).

2.4.4 Data acquisition

The data acquisition software used for the measurements connects the goniometer controller to the electronics used to register the detector signals and allow also a fast preliminary data analysis.

In the present experiments, the measurements of the charge-state distribution and the photon yield could not be performed coincidently. The reason is the difference in detection efficiency of the particle and photon detectors. In the limited volume of the vacuum chamber only two X-ray detectors could be installed around the target. The solid angle of the X-ray detectors (in order of 10^{-3}) is relatively small due to the detector size and the experiment geometry. Therefore, the detection efficiency for the X-rays is much lower than the one for the ion yield. To reduce the measurement time the beam intensity was increased to 2×10^8 pps (3×10^6 pps after the collimation). The particle detector collects the full beam intensity. But its detection efficiency drops dramatically as mentioned before.

In figure 2.17 the scheme of the data acquisition system used for the charge-states measurement is presented. The two anode and two cathode signals from the particle detector are fed in the main amplifier ORTEC 855. The amplifier signals are transferred to the computer via ADC. The position of the ion on the detector is reconstructed according to the relation 2.1 (chapter 2.4.2).

The goniometer controller and the data acquisition program are connected in such a way that the scanning of the angular ranges is done automatically after a certain measurement time or number of counts in the detector for each angular value.

A similar scheme (see figure 2.18) is used for the X-ray measurements. Due to the fact that the beam intensity is not constant in time, a beam intensity monitoring for the X-ray measurements is necessary.

For this, a third X-ray detector was installed behind a Cu foil mounted in the end of the beam line. The number of emitted photons is proportional to the number of ions passing the foil and it was used for a relative normalization of the X-ray spectra. Each measurement was made during 300 seconds at the fixed target position.
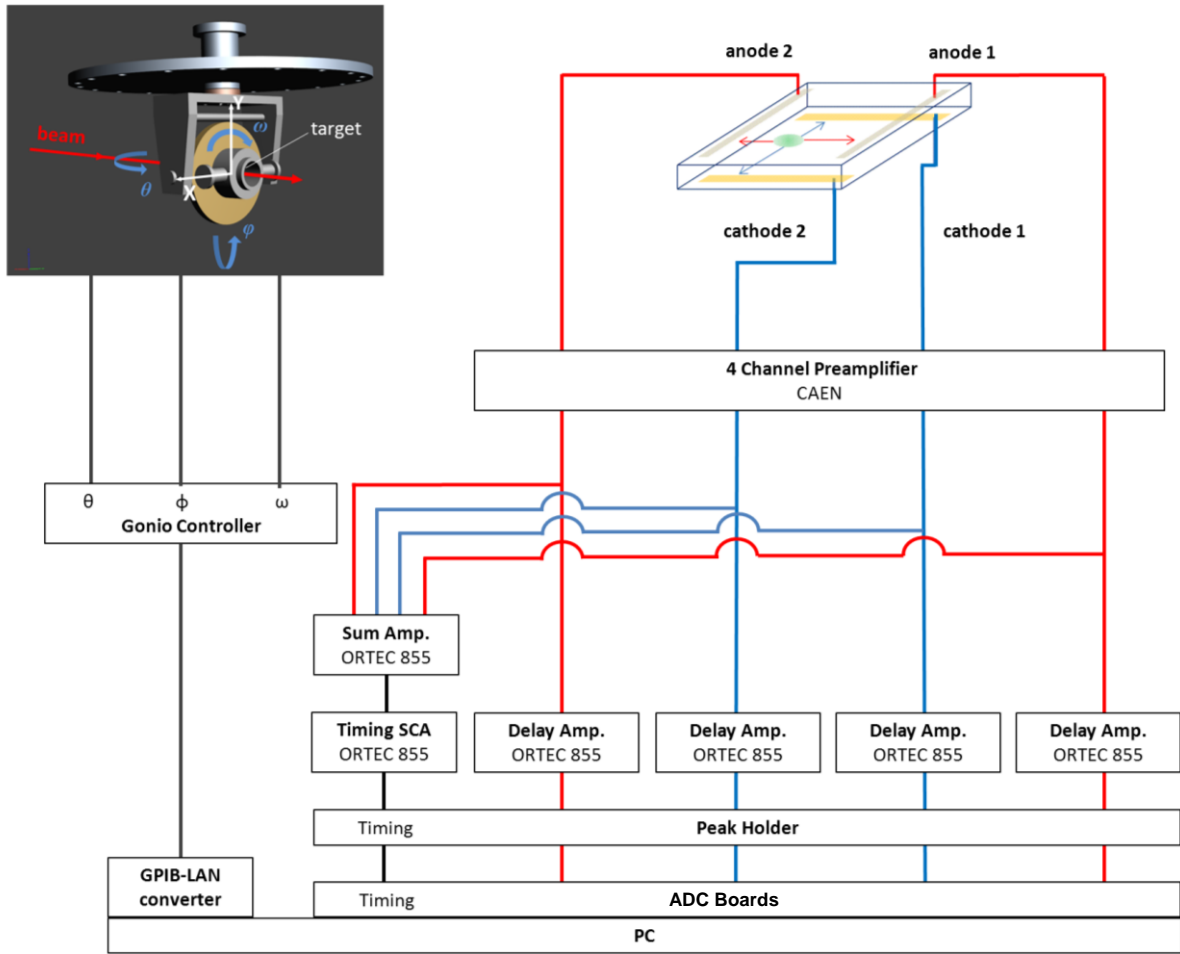
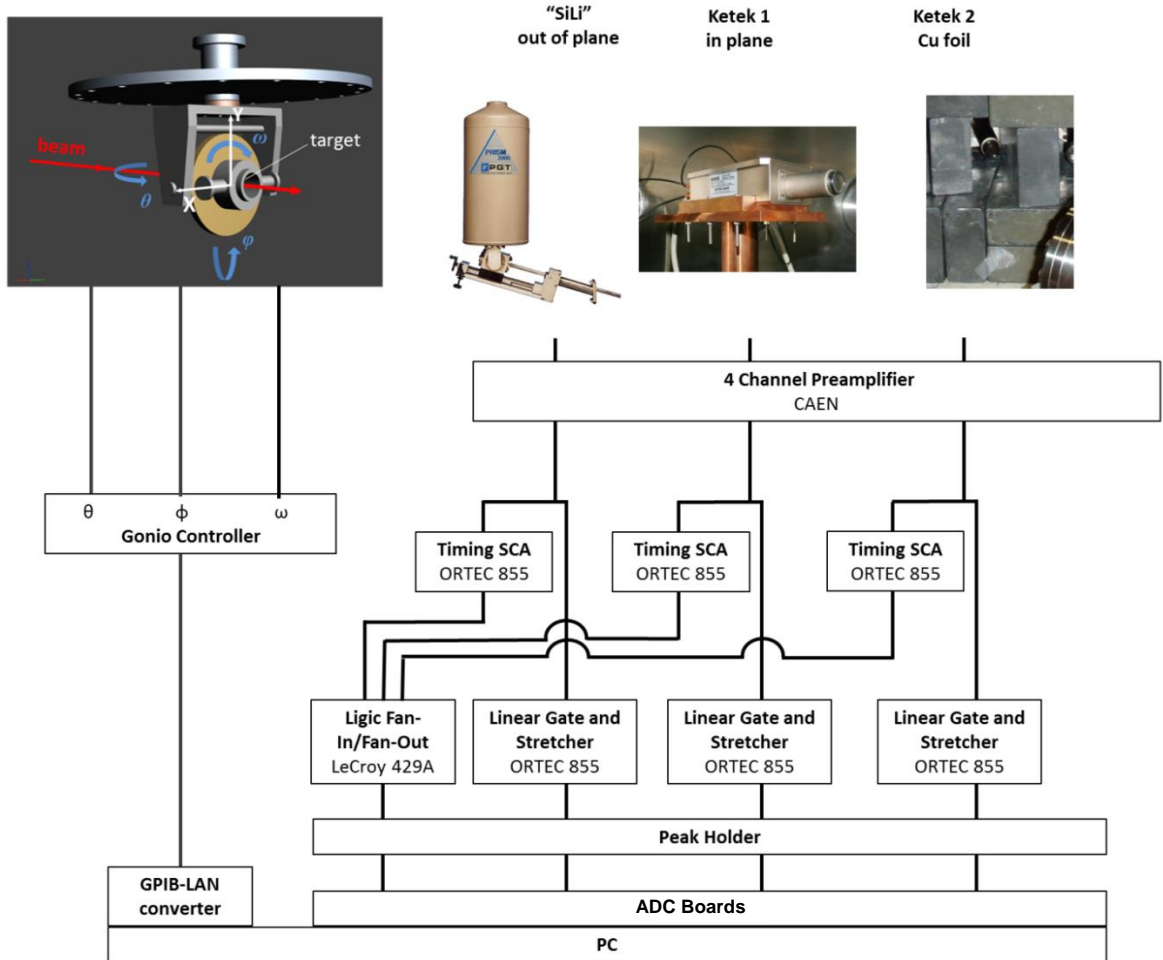Figure 2.17 *Electronic scheme used for the charge-state measurements.*

Figure 2.18 *Electronic scheme used for the acquisition of the X-rays.*

2.5 Experimental conditions

The occurrence of the resonance coherent excitation of the projectile ions in a crystal is indicated by the variations in the charge-state distribution of the projectile ions and of the photon yield emitted from the decay of the excited states of the ions measured as a function of the target orientation relatively to the beam direction.

The first important step of an RCE experiment is the precise adjustment of the target position in the goniometer. This is done by a simple measurement of the initial charge-state fraction of the ions passing the target at channeling conditions. The second step is the precise definition of the beam energy by an estimation using the resonance formula and the angular position of the peak in the charged-state resonance curve obtained for the ion transition into a level which does not have fine splitting.

2.5.1 Crystal position adjustment

A roughly known axial or planar crystal orientation of the target can be defined more accurately by a measurement of the survival charge-state fraction of the ions, penetrating the target, as a function of the target position relatively to the beam direction.

The structure and orientation of the target is approximately known from the producer. In the case of the present work, the crystal was cut in such a way that the (220) planes are oriented horizontally, if the target is mounted under $\varphi = 45$ degrees to the beam direction. To adjust the crystal position more precisely, the RCE of the ions at the (220) planar channeling orientation is identified. The measurement of the ion charge-state distribution as a function of the incident angle of the beam on the target was done by scanning the angular position of the target, in one direction, keeping the other two constant. In figure 2.19 the result of a preliminary measurement with a step of 0.01 degree is presented. Red and blue points are the fraction of the H-like and bare argon ions, respectively. The ion yield has been measured by the particle detector for a constant number of projectiles ions per measurement. When the channeling condition is satisfied, maxima of the initial charge-state fraction and corresponding minima of the bare fraction are observed due to the suppression of interactions between the projectiles and target atoms. Five planar channeling conditions are detected in the angular range scanned during presented in figure 2.19 measurement. The φ values of the peak positions in the observed spectrum, at fixed θ, have to be compared with values known from the crystal structure.
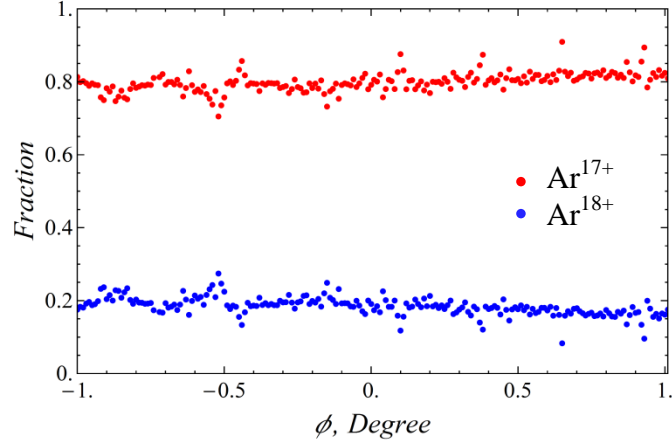
Figure 2.19 *Charge-state distribution of 455 MeV/u H-like Ar ions after passing the 1 μm Si-target measured at θ= -1°.*

To improve the precision of the crystal positioning the measurement can be repeated with a finer step for the angular scanning around roughly known position. The examples of the fine scanning performed around presumed angular coordinates of the (220) and (004) planar orientations, are presented in figure 2.20 and 2.21.

In the present case, four fine scanning were performed: a scanning of the φ angle at $\theta = \pm 1°$ (corresponds to (220) orientation) and a scanning of the θ angle at $\varphi = 0°$ and $2°$ (corresponds to (004) orientation). To identify the value of the φ angle with a higher precision a Gauss fit of the experimentally obtained peaks has been performed. Using values of the two pairs of the θ and φ coordinates for each orientation, a linear relation between θ and φ angles can be described by the following equations set:

$$\begin{cases} A_{(220)}\, \theta_1 + B_{(220)} = \varphi_1 \\ A_{(220)}\, \theta_2 + B_{(220)} = \varphi_2 \\ A_{(004)}\, \theta_3 + B_{(004)} = \varphi_3 \\ A_{(004)}\, \theta_4 + B_{(004)} = \varphi_4 \end{cases} \tag{2.2}$$

Using the values of the $A_{(220)}, B_{(220)}, A_{(004)}$ and $B_{(004)}$ coefficients from the system (2.2), the equation of the interception line between (220) and (004) planes can be found as:

$$\begin{cases} A_{(220)}\, \theta + B_{(220)} = \varphi \\ A_{(004)}\, \varphi + B_{(004)} = \theta \end{cases} \tag{2.3}$$

Solving equation (2.3) the θ and φ coordinates of the interception line were found, $\theta = -0.610034°$ and $\varphi = 0.925366°$. These values define the position of the $[\bar{1}10]$ crystallographic axis of the target relatively to the beam direction. In the present work the crystal orientations was always defined relatively to the $[\bar{1}10]$ axis. To find out the absolute value of the ions incident angle, the coordinates of the $[\bar{1}10]$ axis have been subtracted from the coordinates given by the goniometer.
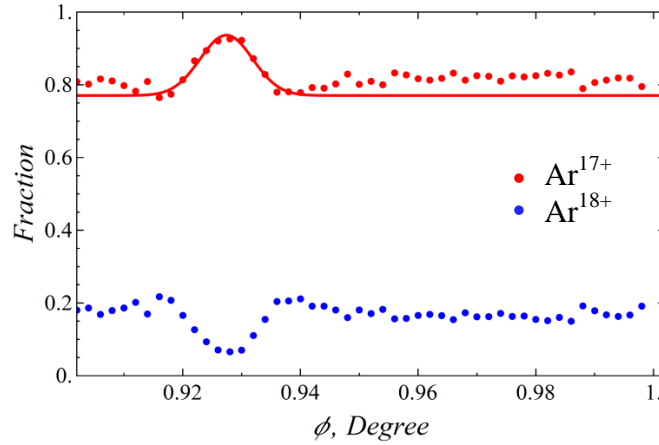
Figure 2.20 *Charge-state distribution of 455 MeV/u H-like Ar after passing the 1 μm Si-target. Scanning of the φ angle with a 0.002°step was performed at θ =-1°.*
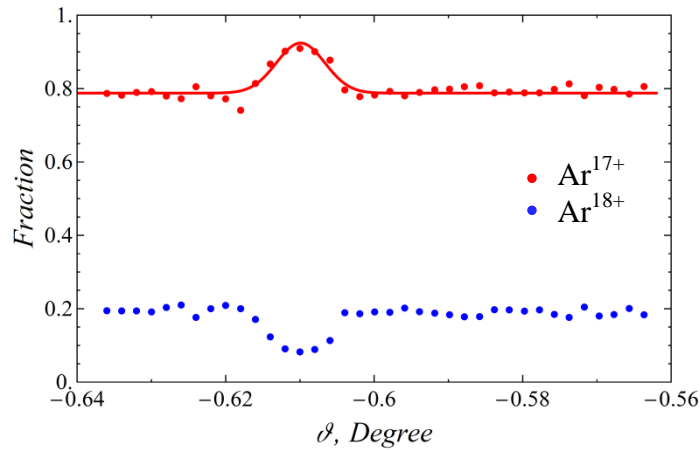
Figure 2.21 C*harge-state distribution of 455 MeV/u H-like Ar after passing the 1 μm Si-target. Scanning of the θ angle with a 0.002° step was performed at φ = 2°.*

2.5.2 Resonance conditions adjustment

From the resonance condition formula (see chapter 1) follows that atomic transitions with energies E_{ij} in the projectile ion can be excited by adjusting the absolute value and the direction of the velocity vector $\boldsymbol{v}$. The absolute value of the velocity is given by the ion beam accelerator with a precision mostly limited by the momentum distribution of the ion beam and the unknown energy loss of the projectile along its path in the target. Therefore the final, precise adjustment of the resonance conditions should be done by changing the ion entrance angle into the target. Any further consideration of the resonance conditions must be done individually for the specific target which is going to be used in the experiment.

As already mentioned before, in the present work a silicon-crystal was used as a target. The unit cell of a Si crystal is shown in figure 2.22.

Figure 2.22 *Si-crystal unit cell: a (220) green and (004) yellow planes and axial orientations in XYZ coordinate system. Red arrow is the velocity vector $\boldsymbol{v}$ of the ion penetrating the crystal.*

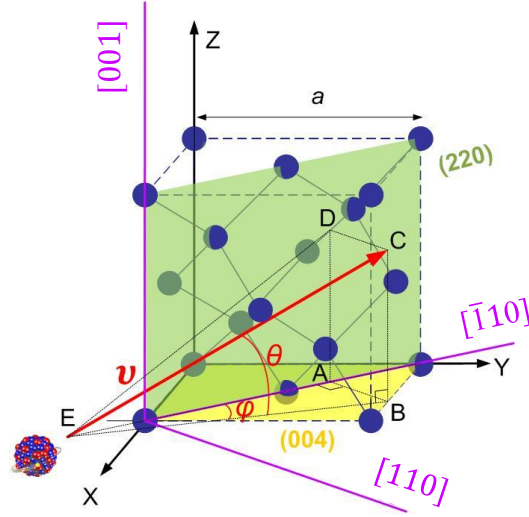With green and yellow the (220) and (004) planes orientations are indicated in the XYZ coordinate system. The most convenient geometrical references of this target are the (220) planar and $[\bar{1}10]$ axial orientations, roughly known from the producer [2.3]. Therefore, it makes sense to consider the velocity projections in a new orthogonal coordinate system based on the $[\bar{1}10]$, $[110]$ and $[001]$ axes of the crystal (marked with magenta in figure 2.22).

In the new coordinate system with unit vectors $\boldsymbol{a}_{\langle\bar{1}10\rangle}$, $\boldsymbol{a}_{\langle110\rangle}$ and $\boldsymbol{a}_{\langle001\rangle}$ the velocity vector can be written as,

$$\boldsymbol{v} = v \left(a_{\langle\bar{1}10\rangle} v_{\langle\bar{1}10\rangle} + a_{\langle110\rangle} v_{\langle110\rangle} + a_{\langle001\rangle} v_{\langle001\rangle} \right), \tag{2.4}$$

where $\boldsymbol{v}$ is the absolute value of the ion velocity and $v_{\langle\bar{1}10\rangle}$, $v_{\langle110\rangle}$ and $v_{\langle001\rangle}$ are the velocity projections on the axes of the new coordinate system. The coefficients $\boldsymbol{a}$ are integer numbers defined in the previous subchapter as the Miller indices k, l and m.

In figure 2.17 the velocity projections $v_{\langle\bar{1}10\rangle}$, $v_{\langle110\rangle}$ and $v_{\langle001\rangle}$ are denoted as, AE, AB and AD correspondently. Considering the right triangles BCE and ABE the velocity projections can be found as,

$$v_{\langle\bar{1}10\rangle} = AE = v \cos\theta \cos\varphi \,,$$
$$v_{\langle001\rangle} = AD = v \sin\theta \,, \tag{2.5}$$
$$v_{\langle110\rangle} = AB = v \cos\theta \sin\varphi \,,$$

where θ is the angle between the velocity vector $\boldsymbol{v}$ and its projection on the (004) plane, φ is the angle between the vector`s $\boldsymbol{v}$ projection on the (004) plane and $[\bar{1}10]$ axis.

From the crystal geometry the periodicity constant d can be found for all three directions as:

$$[\bar{1}10] \text{ direction:} \, d = a/\sqrt{2},$$

$$[001] \text{ direction:} \, d = a, \qquad (2.6)$$

$$[110] \text{direction:} \, d = a/\sqrt{2},$$

where a is the lattice constant of the crystal.

Taking into account the relation (2.5) and (2.6), the resonance condition (1.23) can be written as:

$$E_{ij} = \frac{\hbar \gamma \boldsymbol{v}_{ion}}{d} = \hbar \gamma v_{ion} \left(k \, cos\theta \, cos\varphi \, \frac{\sqrt{2}}{a} + l \, sin\theta \, \frac{1}{a} + m \, cos \, \theta \, sin\varphi \, \frac{\sqrt{2}}{a} \right). \qquad (2.7)$$

Thus, the transition energy E_{ij} is a function of the ion velocity v_{ion} and of the crystal orientation given by the angles θ and φ and the Miller indices k, l and m. Therefore, the resonance condition can be tuned by changing the ion velocity or by changing the crystal orientation. If a specific atomic transition of energy E_{ij} should be excited, the relation (2.7) can be used to find out the needed incoming energy of the ion, for the established crystal geometry and orientation. An example of such calculation is given in figure 2.23 where the formula (2.7) is applied for some transitions in H-like Ar ions passing through a Si-crystal at (220) planar orientation.

The different groups of lines belong to different values of the Miller indices: $k \in (1; 3)$, $l \in (-5; 5)$ and $m \in (-10; 10)$. For a fixed k, depending on l and m values, different lines give the resonant condition for the same transition energy. Groups of lines correspond to different k value and contain 10 lines obtained from different l indexes. Higher k index values correspond to lower beam energy. The extinction rule of the resonance, induced by a frequency of the oscillating crystal field, is $k + m + l =$ even or $2k + l = 4j + 2$, where j is an integer. This rule is a limiting factor in choosing the value for the Miller indices. The calculation were made considering channeling conditions (2D), therefore $\varphi = 0$. Value of m does not matter in the case of planar channeling because $\varphi = 0$.

To specify the angular range for the measurements a relation between φ and θ angles is calculated for a chosen value of the projectile energy. Figure 2.24 shows the angular diagram calculated with $k = 1$, $l \in (-3; 6)$ and $m = \in (-5; 5)$ for transitions in H-like Ar at 455 MeV/u, passing a Si-crystal at non-channeling conditions ($\varphi \neq 0$). The groups of lines on the abscise axis correspond to different l index values and contain lines obtained from different m values.

The present simulation was obtained for allowed transitions in H-like Ar denoted by different colors at the graph.
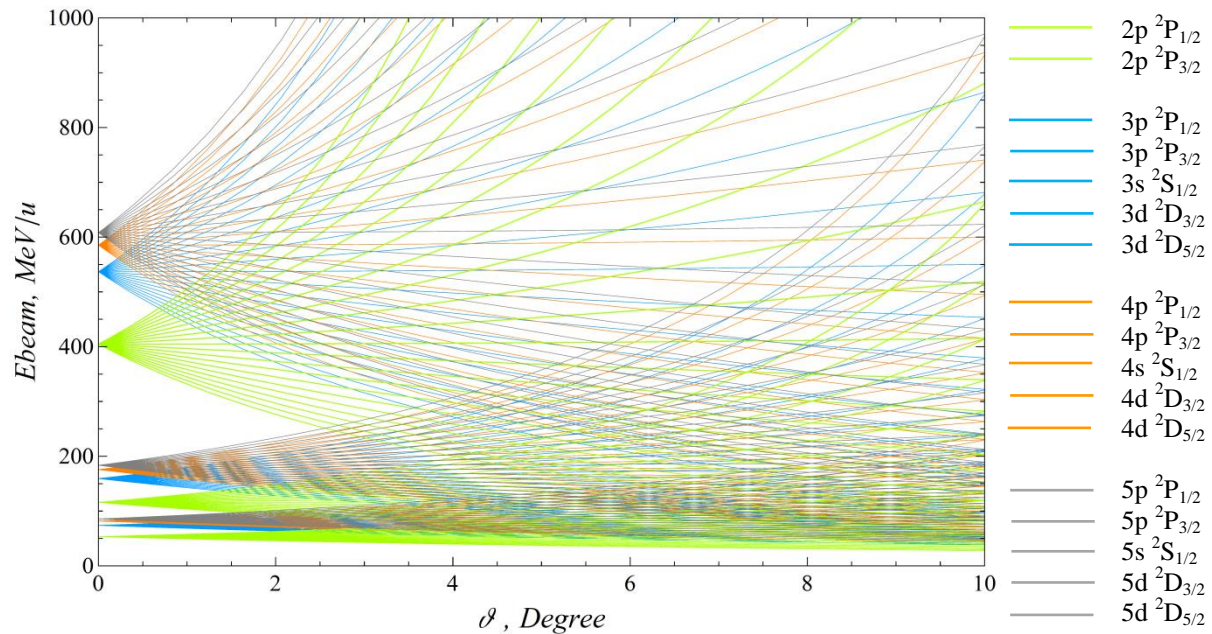
Figure 2.23 *Beam energy as a function of θ angle calculated for (220) planar crystal orientation at φ = 0 (2D) satisfying the resonant conditions for different transitions in H-like Ar (denoted with different colors)*
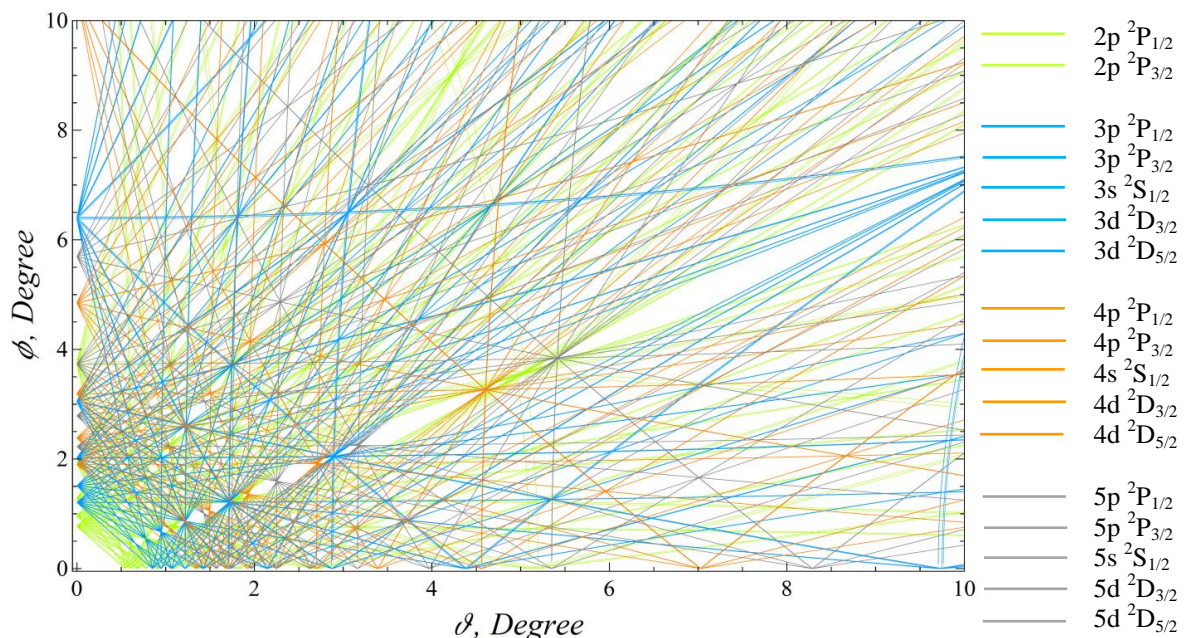
Figure 2.24 *Resonant conditions diagram calculated for transitions in H-like Ar at 455 MeV/u in a Si-crystal.*

Any point satisfying the function $\theta(\varphi)$ corresponds to a condition on which a resonant excitation is possible. Due to the multi parametric dependence of the resonant conditions, it is possible that for the same crystal orientation, defined by the values of θ and φ, the conditions

54

for transitions to the different levels j_1 and j_2 are simultaneously satisfied. Hence a double resonant coherent excitation, DRCE, of the ion can occur.

The DRCE condition corresponds to the crossing points of two $\theta(\varphi)$ functions calculated for the specific transition energies. A DRCE is a two-step electron transition in the projectile from the ground state i into first excites state j_1 and then into second excited state j_2.

Theoretically there are many possible crystal orientations which can be chosen so that selected resonance condition is satisfied. However there are some experimental limitations which reduce the number of possible combinations.

Considering the field induced by the higher order crystal orientations, there is a practical limit for the m values. These values are defining the distance between the planes of the considered crystal orientation. If m value is too high, the distance between the planes is large and the potential field is too weak to induce the excitation of the ions. Therefore, in the present experiments the range for the m values was limited to less than 4.

2.5.3 Beam energy estimation

After fixing the target position and the resonant conditions, a precise definition of the beam kinetic energy is requested. If the beam energy defined by the accelerator is not known with sufficient accuracy, it can be determined by inducing the resonant coherent excitation of a well-known transition in the projectile ions. Considering a well-known crystal orientation and the transition energy, the beam energy can be calculated from the position of the minimum in the resonance curve. In the case of H-like Ar beam, the resonance curve for the RCE transition from the ground state into the $n = 2$ level was obtained by measuring the initial charge fraction of ions as a function of crystal orientation. Figure 2.25 presents the resonance curve for the $1s \rightarrow 2p\ ^2P_{3/2}$ excitation with a transition energy of 3322.9919 eV [2.8].
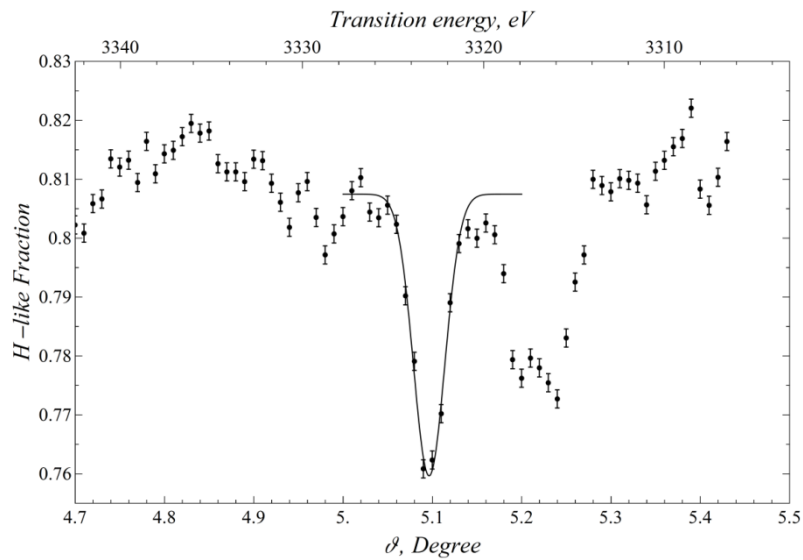
Figure 2.25 *Charge-state resonance curve of H-like Ar ions coherently excited into $2p\,^2P_{3/2}$ state in 1 μm Si-crystal.*

A sharp decrease of the initial charge-state fraction induced by the field of the $(1\bar{1}0)$ planar orientation is observed at $\theta = 5.0963°$. The θ position of the resonance peak was obtained from the Gauss fit. Considering this θ value and the transition energy, the kinetic energy of the beam was calculated to be 455.3 MeV/u. Depending on the transition energy and crystal orientation the influence of the accuracy of the beam energy on the resonance position can be very sharp and may significantly change the resonance condition diagram.

Apart of the natural width of the resonance related to the finite lifetime of the excited state, some processes destroying the coherence contribute into the peak width. For instance, angular straggling of the ions in the target, divergence and momentum spread of the ion beam. Typically, the FWHM of the resonance peak for the RCE into the $n = 2$ state is about 0.05° (1.7 eV).

3 Data analysis

In the present chapter the detailed analysis of the ion charge-state distributions and the X-ray spectra is presented. To obtain the resonance curves from the ion charge-state distributions, the integration of the measured charge spectra was performed. The analysis of the X-ray spectra includes the energy calibration, Doppler correction and the X-ray yield normalization. The experimental evidence of the RCE and DRCE is based on both data: charge-state distribution and X-ray measurements.

3.1 Charge-state distribution of the ion yield

To obtain the resonance curves based on the charge-state distribution of the ions interacting with the crystal-target, the absolute measurement of the number of ions passing the crystal is required. Therefore, the particle detector should be able to measure the whole beam intensity with 100% efficiency. As shown in chapter 2, the Si particle detector is limited in count rate, therefore these measurements have been performed with low beam intensity. The charge states of the ions released from the crystal-target are detected after the magnetic separation, as separated spots on the particle detector. The charge separation depends on the dipole magnet properties and the position resolution of the detector (see chapter 2.4.2)

By passing the crystal the Ar projectile ions change their initial charge-state due to the electron capture or ionization in collisions with the target atoms. For the case of 455.3 MeV/u Ar ions penetrating a 1 μm Si target the electron capture probability is not significant. Therefore, only the initial charge-state, the H-like, and the ionized fraction were measured by the PSD. For the measurements, the angular step was adjusted from 0.02 up to 0.005 degrees depending on the resonance profile. Figure 3.1 shows H-like Ar ions detected by the PSD after passing the Si target at non-resonance orientation but without charge separation. In this case, all charge-states are registered by the detector in one spot. When the dipole magnet is turned on, the charge-states are separated into different trajectories (figure 3.2) and on the detector two spots are registered corresponding to the initial charge-state (Ar^{17+}) and the ionized ions (Ar^{18+}).
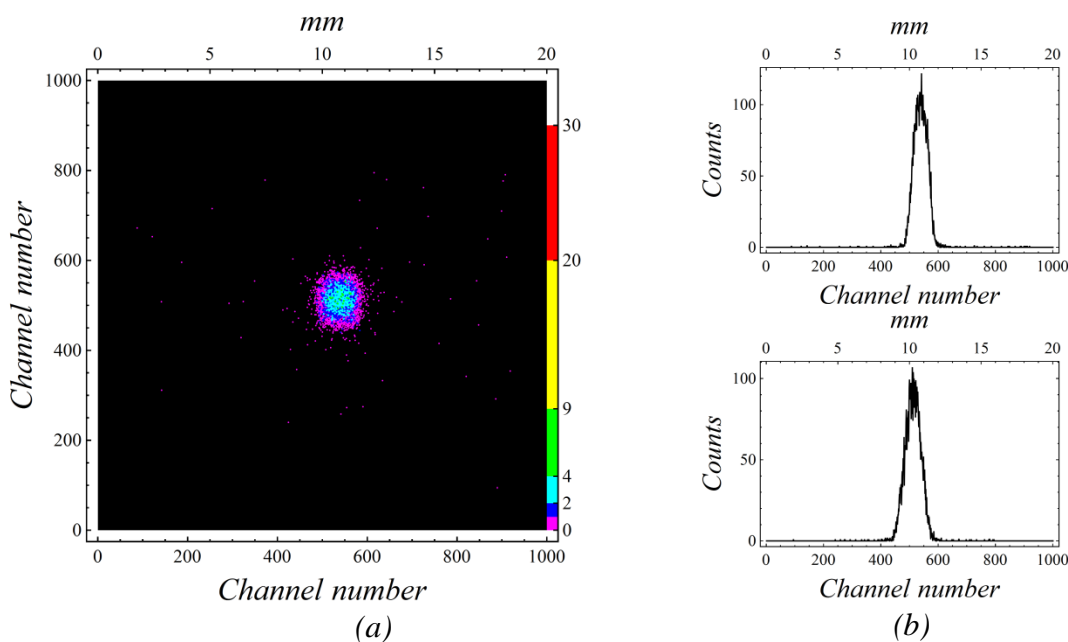

Figure 3.1 *The Ar^{17+} beam profile: (a) two-dimensional image in logarithmic scale; (b) beam projections on the X and Y axes.*
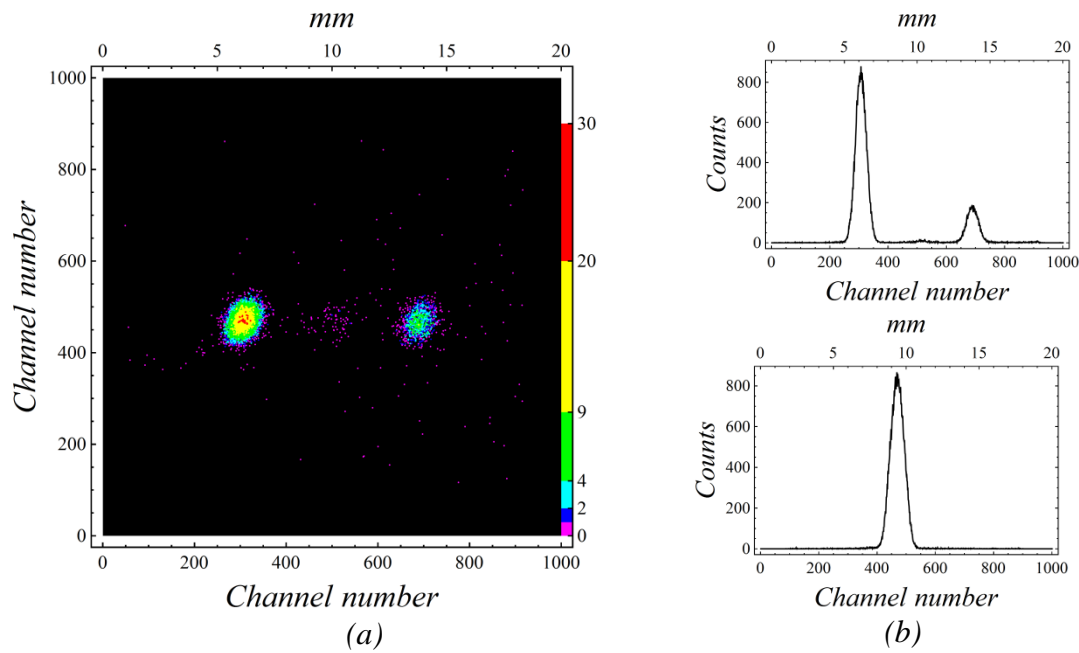
Figure 3.2 *Charge-state distribution of the 455 MeV/u Ar^{17+} after passing the Si-crystal at non-resonance orientation, magnet in turned on: (a) two-dimensional image in a logarithmic scale; (b) projections on the X and Y axes.*

Although the measurements presented in figure 3.1 and 3.2 have been performed with the same beam intensity, the accumulation time was different, therefore the total number of the registered ions should not be compared in these cases. The spot on the left part of the spectrum 3.2 (a) correspond to the initial charge-state of the beam, 17+. These ions have passed thought the crystal without excitation or were exited and de-excited via photo decay. Therefore, the final charge-state is the 17+. The ions with higher charge-state registered on the right part of the spectrum correspond to the bare argon fraction. These ions were directly ionized or excited by the crystal potential and de-excited via collisional ionization with target atoms. The low intensity spot in the middle is an electronic artifact.

For the ion yield estimation both peaks of the X projection are integrated and the result is used to obtain the fraction of the different charge-states. The variation of the charge-state yield, as a function of the crystal orientation relatively to the incoming ion direction (θ angle), is shown in figure 3.3. The upper curve represents the number of detected ions in the initial charge-state, 17+, and the lower one represents the ionized fraction, 18+. The presence of a resonance transition is indicated by the maximum number of Ar^{18+} and minimum number of the initial Ar^{17+} ions.
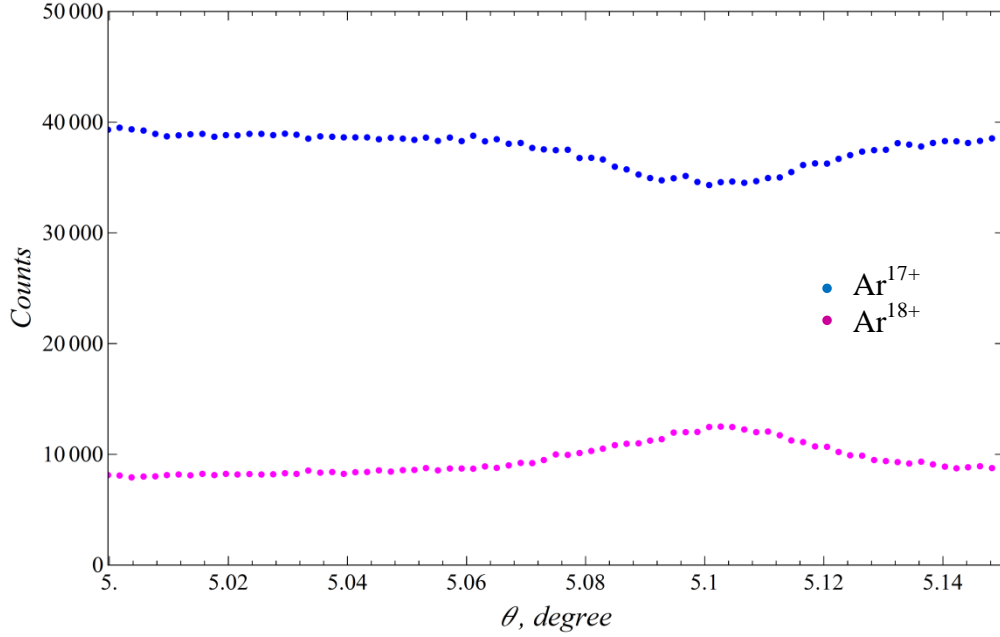
Figure 3.3 *Charge-state yield variation as a function of crystal rotation angle θ: Ar^{17+} (blue points) and Ar^{18+} (magenta points).*

The resonance curve is the variation of the fraction *F* of the initial charge-state defined as a function of the crystal rotation angle θ:

$$F = \frac{N_{17+}}{N_{ions}}, \tag{3.1}$$

where N_{17+} is the number of H-like Ar ions and N_{ions} is the total number of the ions accumulated on the PSD for each measurement.

An example of a typical resonance curve is shown in figure 3.4.
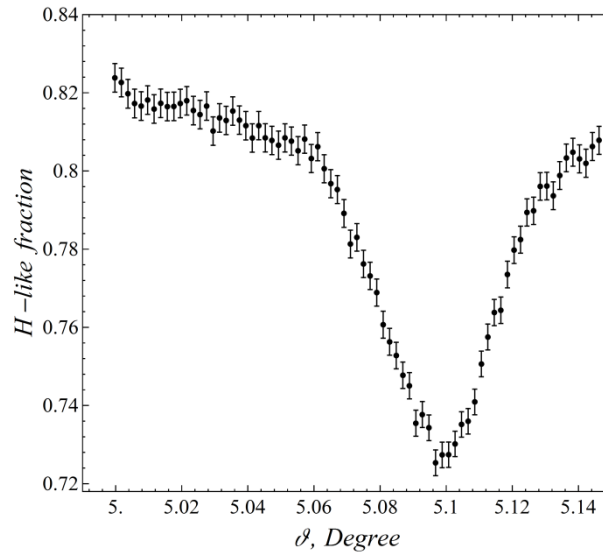
Figure 3.4 *The resonance curve for double excitation in 455.3 MeV/u Ar^{17+} ions in a 1 μm thick Si-crystal*

The error bars represent the statistical error dF of the obtained fraction calculated as:

$$dF = \sqrt{\left[\frac{N_{17+}}{N_{ions}}\right]^2 dN_{17+}{}^2 + \left[\frac{-N_{17+}}{N_{ions}{}^2}\right]^2 dN_{ions}{}^2}, \tag{3.2}$$

where $dN_{ions} = \sqrt{N_{ions}}/N_{ions}$ is the statistical error of the total number of the ions which is constant for every scan point and $dN_{17+} = \sqrt{N_{17+}}/N_{17+}$ is the statistical error defined for every measured fraction of N_{17+}.

The same analysis procedure was applied to all data concerning the charge-state measurements. The depth, the position of the minimum, the width and shape of the curve contain considerable information about the interaction of the ions with the crystal target. These aspects will be discussed in chapter 4.

3.2 X-ray spectra

Depending on the kind of measurement which was performed (X-ray yield at a specific crystal orientation or variation of the yield as a function of the rotation angle θ) the analysis steps are different. From the X-ray spectra one may obtain the information about the transition energy of the excited level and about the competition between possible excitation processes as a function of the ion trajectory through the crystal. In both kinds of measurements, the X-ray energy and the number of detected photons are extracted from the experimental data. Therefore, the detection efficiency and the energy resolution of the X-ray detectors are parameters which must be known. Further, the normalization of the different measurements and the Doppler correction of the detected X-ray energies are needed steps in the data analysis.

3.2.1 Energy calibration

The energy calibration of the X-ray detectors was performed using a ^{55}Fe X-ray source. The source was mounted in the vacuum chamber at the target position and the detectors were installed at the same positions as for the experiment.
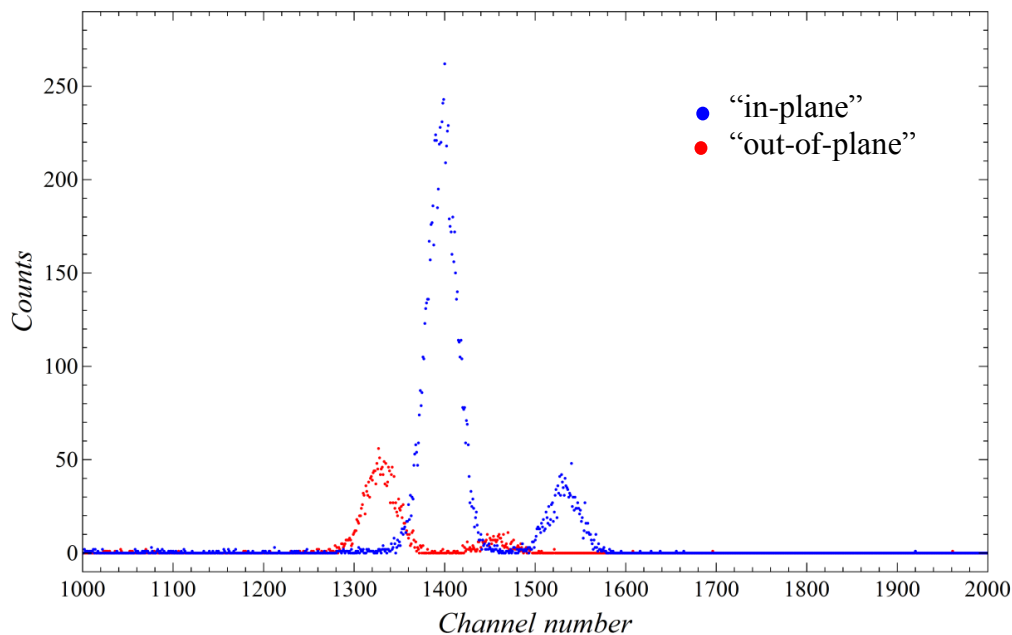
Figure 3.5 *X-ray spectra from the ^{55}Fe X-ray source measured by the "in-plane" and "out-of-plane" detectors.*

The X-ray spectra were registered during one hour, after the experiment. The acquisition of the calibration spectra was done with the same electronics as for the experiment (see section 2.4.3). Figure 3.5 shows an example of calibration spectra for the "SDD" and "SiLi" detectors. The ^{55}Fe source emits two lines in the energy interval of interest: $K_{\alpha 1}$ at

62

5.89875 keV and $K_{\beta1}$ at 6.49045 keV [3.1]. Energies and corresponding channel numbers used for the calibration are listed in table 3.1.

A linear fit has been used to obtain the energy calibration function:

$$E = a \times ch + b, \tag{3.3}$$

where E is the value of the energy, ch is the channel number in the spectrum and a and b are the fit parameters.

The obtained calibration functions are listed in table 3.1 and plotted in figure 3.6. The energy calibration was applied to all measured spectra for the identification of the registered lines. The same methods have been used for the energy calibration of the second "SDD" detector installed at the end of the beam line.
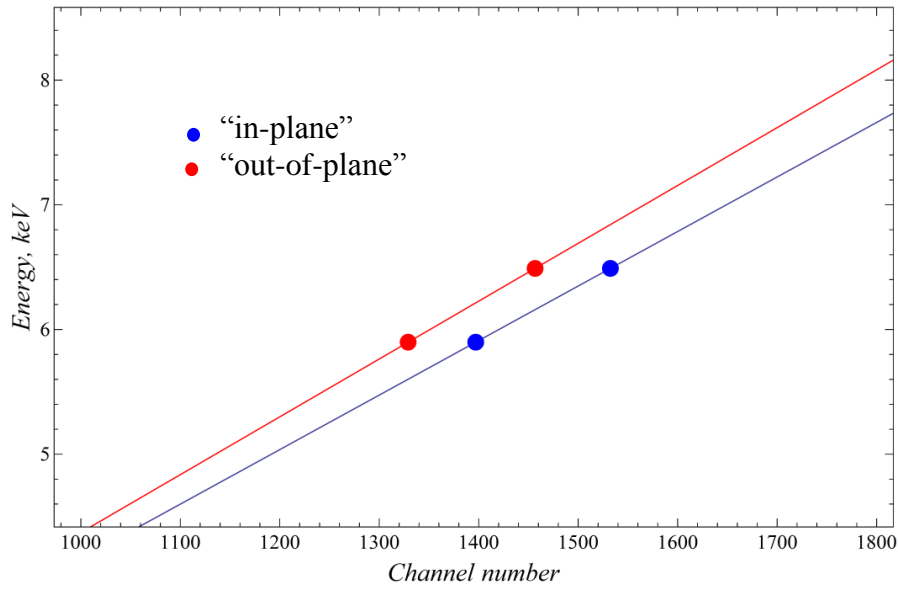
Figure 3.6 *Calibration curve for the "in-plane" and "out-of-plane" detectors.*

Table 3.1 *Energy calibration of the "SDD" and "SiLi" detectors*

^{55}Fe line	Energy, keV	Channel number		Calibration
		"SDD"	"SiLi"	
$K_{\alpha1}$	5.89875	1397.06	1329.11	$E = 0.0046\ ch - 0.27$
$K_{\beta1}$	6.49045	1532.37	1456.67	$E = 0.0044\ ch - 0.21$

The energy calibrated X-ray spectra emitted from the 455.3 MeV/u Ar^{17+} ions after the excitation in the Si-target registered by the "SDD" and "SiLi" detectors are shown in figure 3.7.
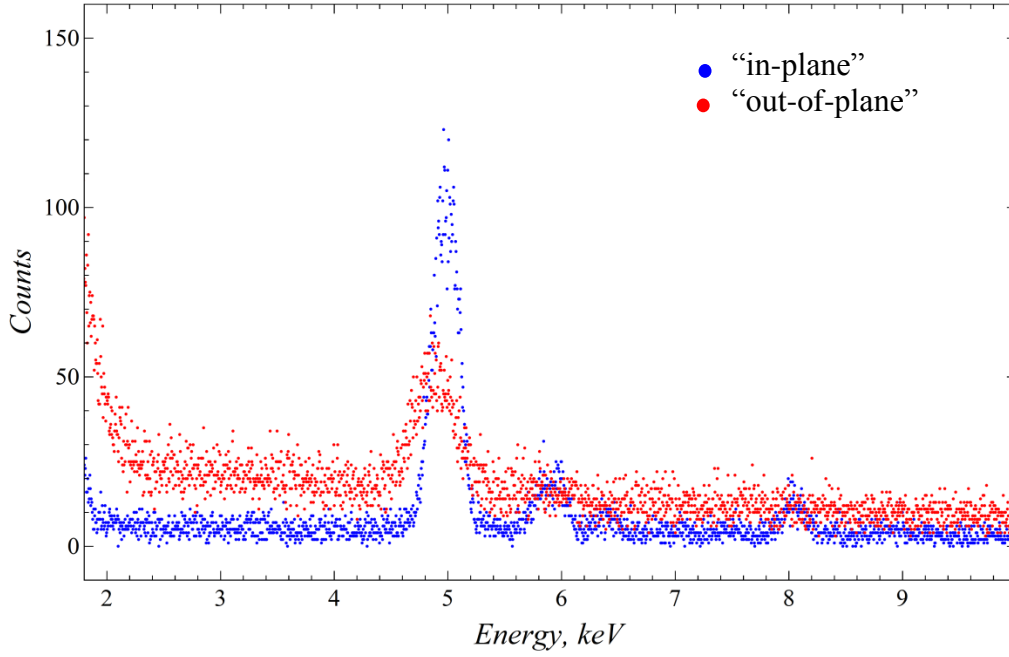
Figure 3.7 *X-ray spectra from 455.3 MeV/u Ar^{17+} ions excited in a 1 µm Si-crystal measured by the "in-plane" and "out-of-plane" detectors.*

The energy of the photons emitted from the decay of the excited Ar ions can be identified from the spectrum after the Doppler correction which is described in the next subchapter.

2.2.2 Doppler correction

In the case of an emitter moving with relativistic velocity, the emitted radiation will be registered by an observer at rest with a different wave length (energy):

$$E_{lab} = \frac{E_\gamma}{\gamma(1 - \beta cos\theta_l)}, \tag{3.4}$$

where E_γ is the energy in the emitter system, E_{lab} is the energy registered by the observer, γ is the Lorentz factor, $\beta = \upsilon/c$, υ is the projectile velocity and θ_l is the observation angle of the detector relative to the emitter direction.

This relativistic effect is known as Doppler shift. For the proper identification of the transition energy the correction for the Doppler shift of the measured spectra is needed. An example of this correction is presented in figure 3.8 showing the X-ray spectra, corrected and not corrected, emitted from the 455.3 MeV Ar^{17+} ions passing the crystal and registered by the "SDD" detector, placed "in-plane" under an observation angle $\theta_l = 41°$ relative to the beam direction.
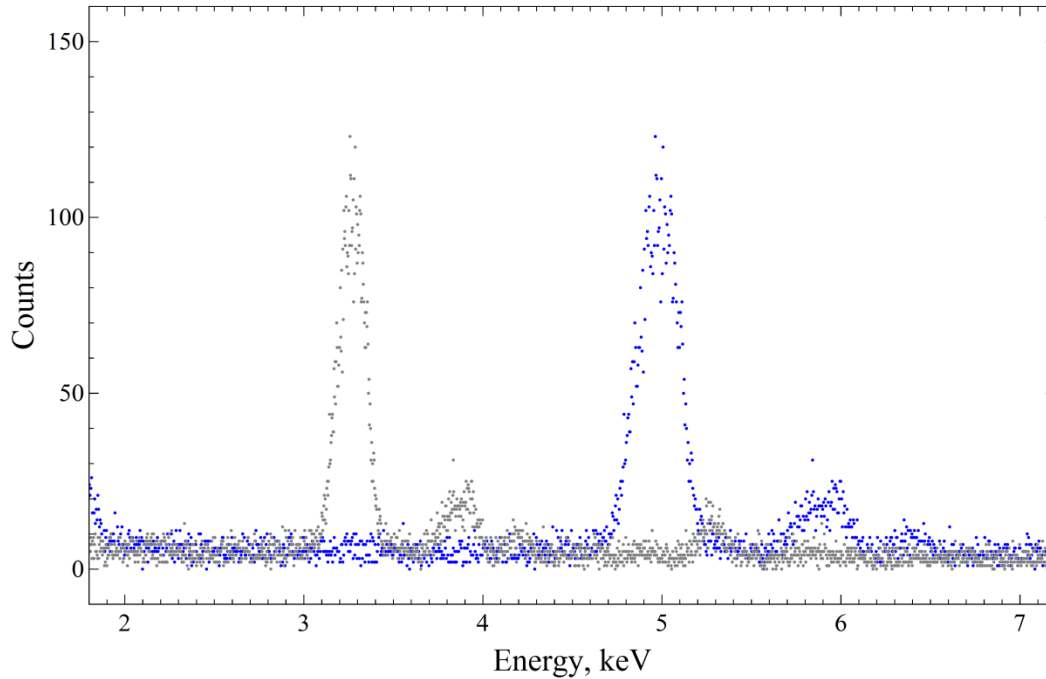
Figure 3.8 *X-ray emission from 455.3 MeV/u Ar^{17+} ions excited in a 1 μm Si-crystal: blue is the spectrum measured by the detector and grey is the Doppler corrected spectrum.*

3.2.3 Normalization of the X-ray spectra

A normalization of the X-ray spectra was necessary due to the different experimental conditions. Generally, the X-ray spectra have been accumulated with different number of ions per measurement because of different excitation probability of the transitions to the higher states. The second aspect is the variation of the beam intensity during one measurement and from one measurement to the other. Therefore, the total number of ions passing the target can be different from measurement to measurement even if the accumulation time is the same. For a quantitative comparison of the X-ray yields observed at different crystal orientations, a relative normalization of the measured spectra was done. A measurement of the X-rays emitted by a copper foil installed at the end of the beam line was always done in parallel to the main measurement (see chapter 2). In figure 3.9 the Cu spectrum recorded by the second SDD is shown.

For the normalization the two lines (K_α at 8.047 keV and K_β at 8.904 keV [3.1]) have been used. Both peaks in the spectrum were fitted with Gauss functions and integrated over an interval of $\pm 3\,\sigma$ which includes about 99.99% of the counts in the peak. Considering the proportionality of the Cu X-ray yield and the beam intensity, the number of photons counted in the two lines is used for a relative normalization of the Ar X-ray spectra (see figure 3.10).

Figure 3.9 *X-ray emission from the Cu foil bombarded by 455.3 MeV/u Ar^{17+} ions measured by the SDD used for beam monitoring. The red line is the Gauss fit of the K_α and K_β lines.*
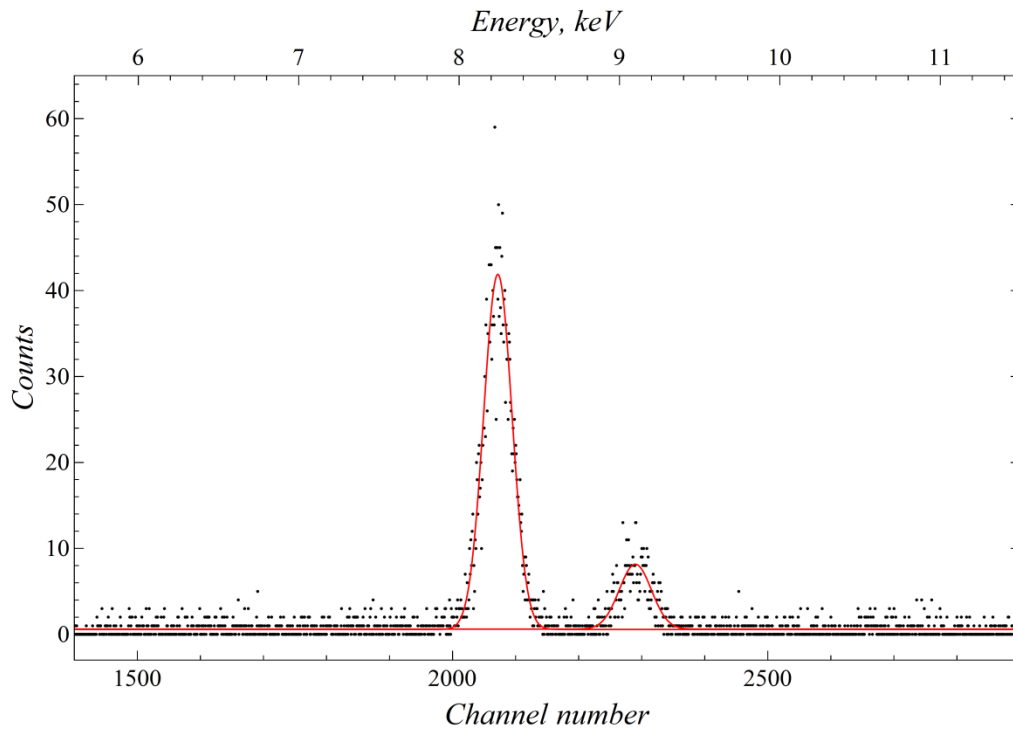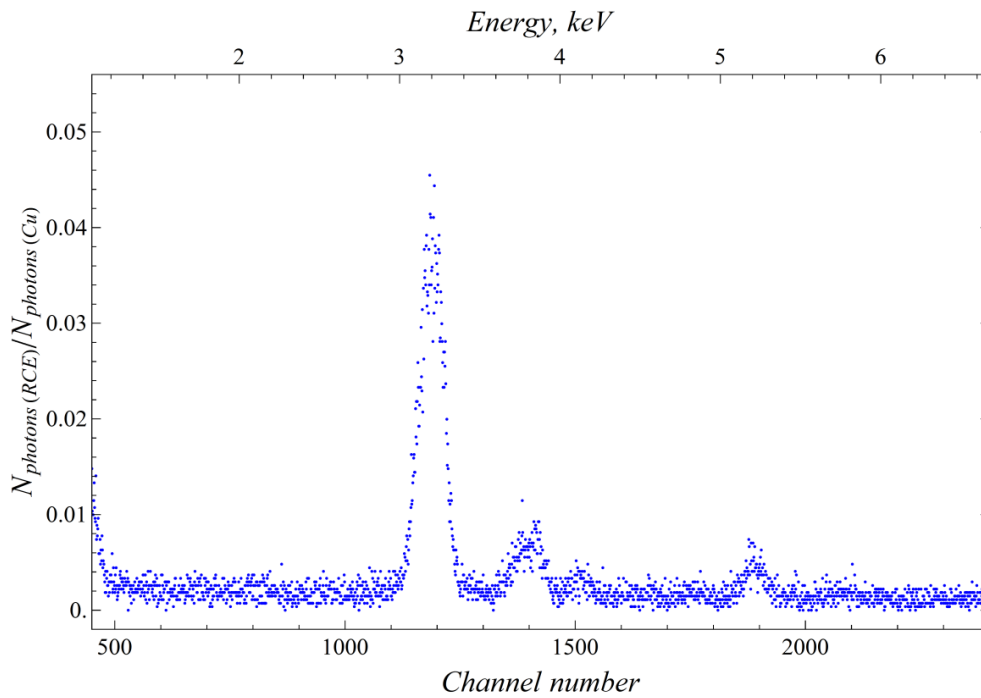

Figure 3.10 *X-ray emission from 455.3 MeV/u Ar^{17+} ions excited in a 1 μm Si-crystal measured by the SDD detector, normalized to the number of photons emitted by the Cu foil.*

3.2.4 Background correction

For a correct evaluation of the photon yield from the X-ray spectra a background correction was done. The background is formed by the bremsstrahlung radiation, electronic noise and a certain amount of photons produced by ion excitations in close collisions with target atoms, regardless of the crystal orientation. The number of photons resulting from close collisions depends on the target thickness. The range of the rotation angle for scanning is typically less than 1°. In this case, the length of the ions path through the crystal target is considered as equal for all measurements of the scanning. Therefore the background was defined as an averaged spectrum obtained from several measurements performed out of resonance conditions.

In figure 3.11 two spectra obtained from the 455.3 MeV/u H-like Ar are presented. The blue spectrum corresponds to the measurement at a resonance conditions and the orange spectrum corresponds to the averaged background spectrum obtained from 9 measurements at non-resonance conditions, normalized to number of photons emitted by the Cu foil. Such a curve is subtracted from every measured X-ray spectrum before the final integration. In both spectra the peak at about 5.2 keV seems to have electronic origin because it appears only for this detector, always at the same position.
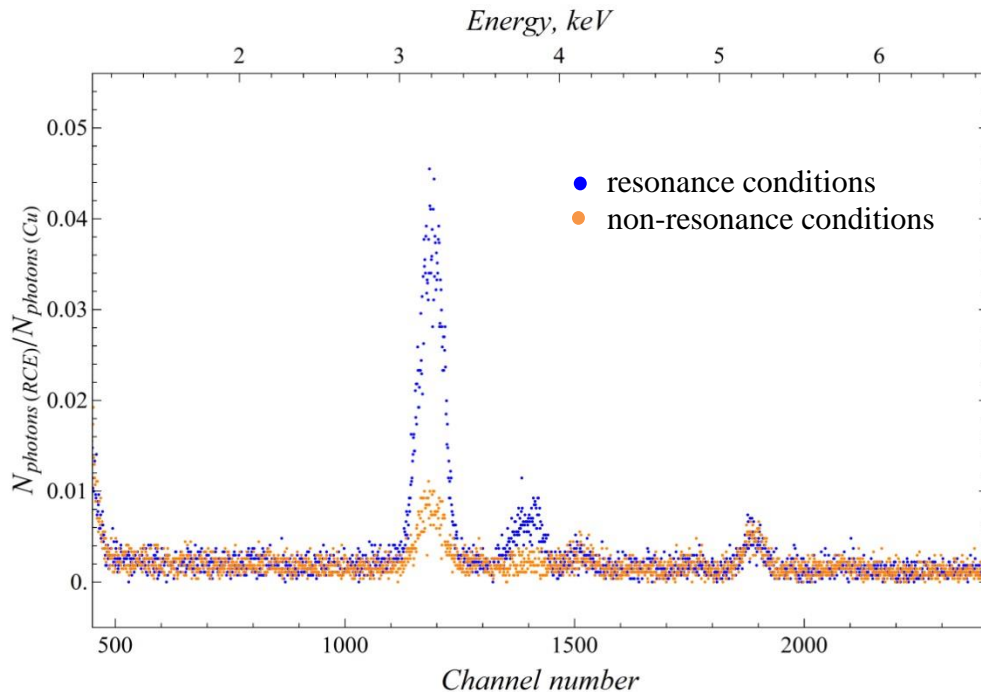
Figure 3.11 *X-ray emission from 455.3 MeV/u Ar^{17+} ions resonantly excited in a 1 μm Si-crystal and X-ray emission measured at non resonance conditions (orange).*
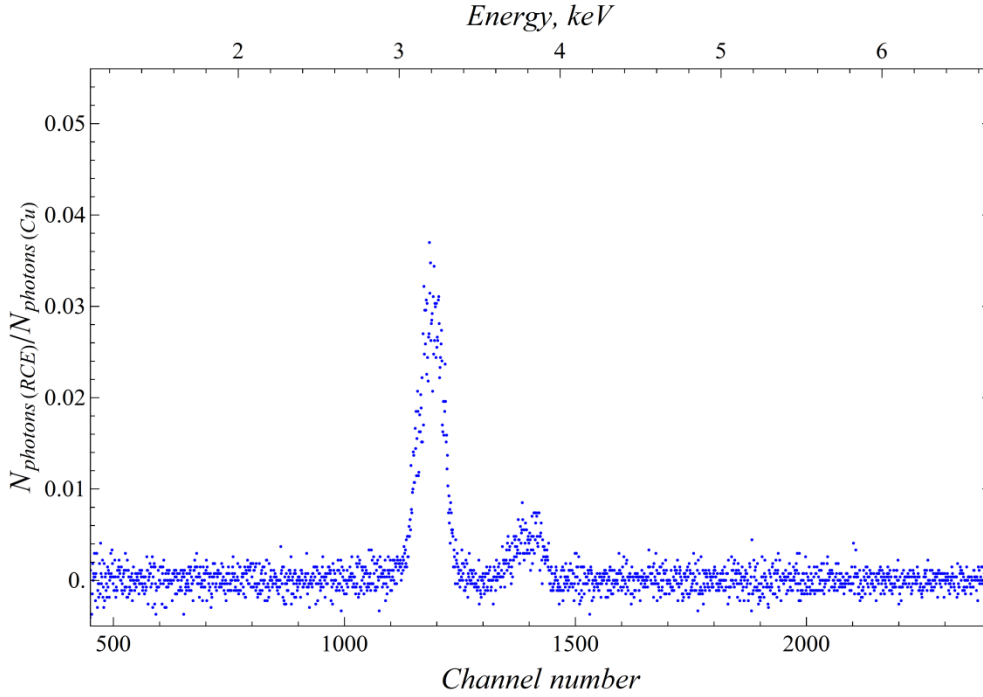
Figure 3.12 *X-ray emission from the decay of the 2p $^2P_{3/2}$ state of 455.3 MeV/u Ar^{17+} ions excited in the 1 μm Si-crystal, after the averaged background subtraction and the Doppler correction.*

The spectrum obtained after the averaged background subtraction is shown in figure 3.12. The resulting spectrum contains only photons emitted due to the decay of the resonantly excited states of Ar projectile ions in the crystal target. The subtraction must be done for all measured X-ray spectra at the resonance conditions.

3.2.5 Efficiency of the X-ray detectors

Another important property of an X-ray detector is the detection efficiency, ε, which is defined by the geometry of the experiment and the absorption probability ε_{ab} of the X-rays.

$$\varepsilon = \varepsilon_g \, \varepsilon_{ab}, \tag{3.5}$$

where ε_g is the geometrical efficiency of the detector.

The geometrical efficiency is calculated, by considering the experimental geometry and the Doppler correction for the solid angle. The detectors have been mounted in the vacuum chamber at a distance R from the target center under the angle θ_l. The geometrical efficiency ε_g is calculated via following formula:

$$\varepsilon_g = \frac{\Omega}{4\pi}, \tag{3.6}$$

where $\Omega_{lab} = S/R^2$ is the detector solid angle in the laboratory system and S is the area of the detector crystal.

The solid angle of the detector seeing the photons emitted from the relativistic ions is:

$$\Omega = \left(\frac{E_{lab}}{E_\gamma}\right)^2 \Omega_{lab}, \tag{3.7}$$

where E_γ is the photon energy in the rest frame of the ions and E_{lab} is the energy registered by the detector.

The absorption probability is a function of the photon energy and the detector material. It is given by the transmission through the Be-window T_{Be} and the absorption A_{Si} in the detector. These values are listed in [3.2] for different photon energies and materials. For the X-rays at about 6 keV (the photon energy in the laboratory system) transmission in beryllium is $T_{Be} = 0.979999$ and absorption in silicon is $A_{Si} = 0.9999$ for the SDD detector:

$$\varepsilon_{ab} = T_{Be}\, A_{Si} \,. \tag{3.8}$$

The solid angle (in the laboratory system) for a detector with the surface of 80 mm^2 installed on a distance of 170 mm to the target is about 2.7×10^{-3} *sr* and the resulting absolute detector efficiency of such detector installed under 41 degrees relative to the beam axis is:

$$\varepsilon = \varepsilon_g\, \varepsilon_{ab} = 2.6\times10^{-3} \tag{3.9}$$

This low value is due to the small active area of the detector and the geometrical constrains inside the target chamber. Therefore, the X-rays acquisition time was relatively long comparing to the measurement of the charge-states.

The X-ray detectors have been placed for the present experiments at different positions and the distance from the target to the detector window could not be measured precisely. Therefore a geometrical correction factor, m, between the "in-plane" and "out-of-plane" detectors was introduced. For the definition of this geometrical factor, the isotropy of the K$_\alpha$ emission from the projectile ions, at non-resonance orientation was used. The factor m between the detectors was estimated as:

$$m = \frac{\sum N_{ph(Ketek)}}{\sum N_{ph(SiLi)}} \tag{3.9}$$

The number of the K$_\alpha$ photons, $N_{ph(Ketek)}$ and $N_{ph(SiLi)}$, was obtained from the integration of the K$_\alpha$ peak from the averaged non-resonance spectrum after the subtraction of the exponentially fitted bremsstrahlung background.

The bremsstrahlung background fitted with an exponential function was subtracted from both averaged X-ray spectra. Figure 3.13 shows an example of the averaged background spectra, after the bremsstrahlung subtraction, for both detectors. Such spectra are typically used for estimation of the *m* factor.
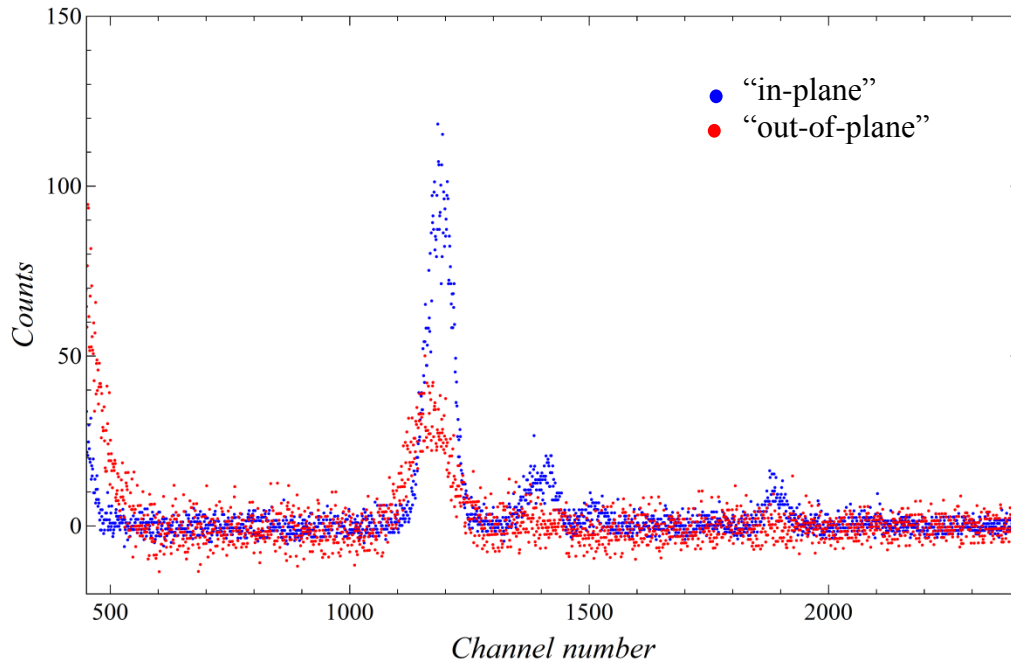
Figure 3.13 *The averaged "non- resonance" spectra after the bremsstrahlung background subtraction.*

3.2.6 Integration of the X-ray spectra.

Depending on the experiment, the X-ray emission of the excited Ar ions has been measured in different ways: at the crystal orientation where the charge-state measurement indicated the best conditions for the resonance (minimum in the charge-state resonance curve) or, similar with the charge-states, by scanning a range for the rotation angle θ. By the integration of the specific X-ray line, resonance curves for X-ray yield were obtained.

The spectrum from the decay of the $n = 3$ excited state in H-like Ar measured at the $\theta = 1.912°$ and $\varphi = 0.1°$ is shown in figure 3.14. After the energy calibration and the Doppler correction, the two peaks in the measured spectrum are identified as K_α and K_β lines emitted from the de-excitation of the $n = 2$ and 3 states of the H-like Ar ions.
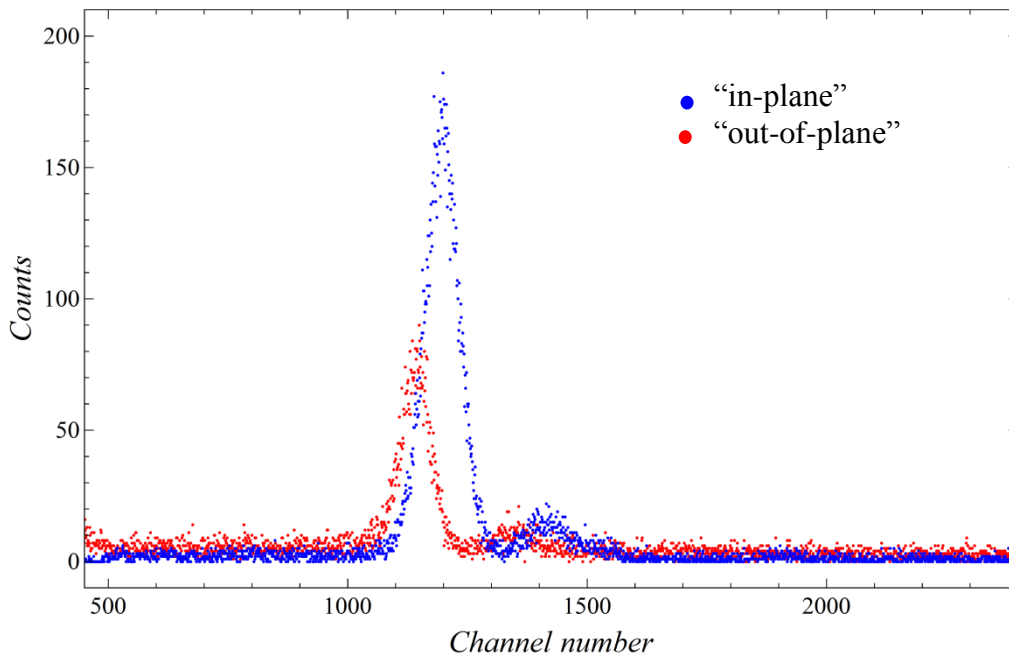
Figure 3.14 *X-rays from the decay of the excited $3s^2\,S_{1/2}$, $3d\,^2D_{3/2}$ and $3d\,^2D_{5/2}$ states in H-like Ar ions measured by the "in-plane" and "out-of-plane" detectors.*

The K_β photons emitted from different fine structure components of the excited levels could not be separated due to the energy resolution of the detectors. As a consequence the measured lines are asymmetric. Therefore the range for the integration of the peaks was defined, in this case, by eye. The integration intervals chosen from the spectrum for the K_α and K_β lines are listed in table 3.2.

Table 3.2 *Integration intervals for the X-rays*

Detector	Integration intervals	
	K_α	K_β
SiLi	1028-1244	1279-1450
SDD	1057-1315	1330-1571

The K_α and K_β resonance spectra, obtained by the integration of the X-ray spectra measured as a function of the θ angle at $\varphi = 0.16°$ are shown in figure 3.15.
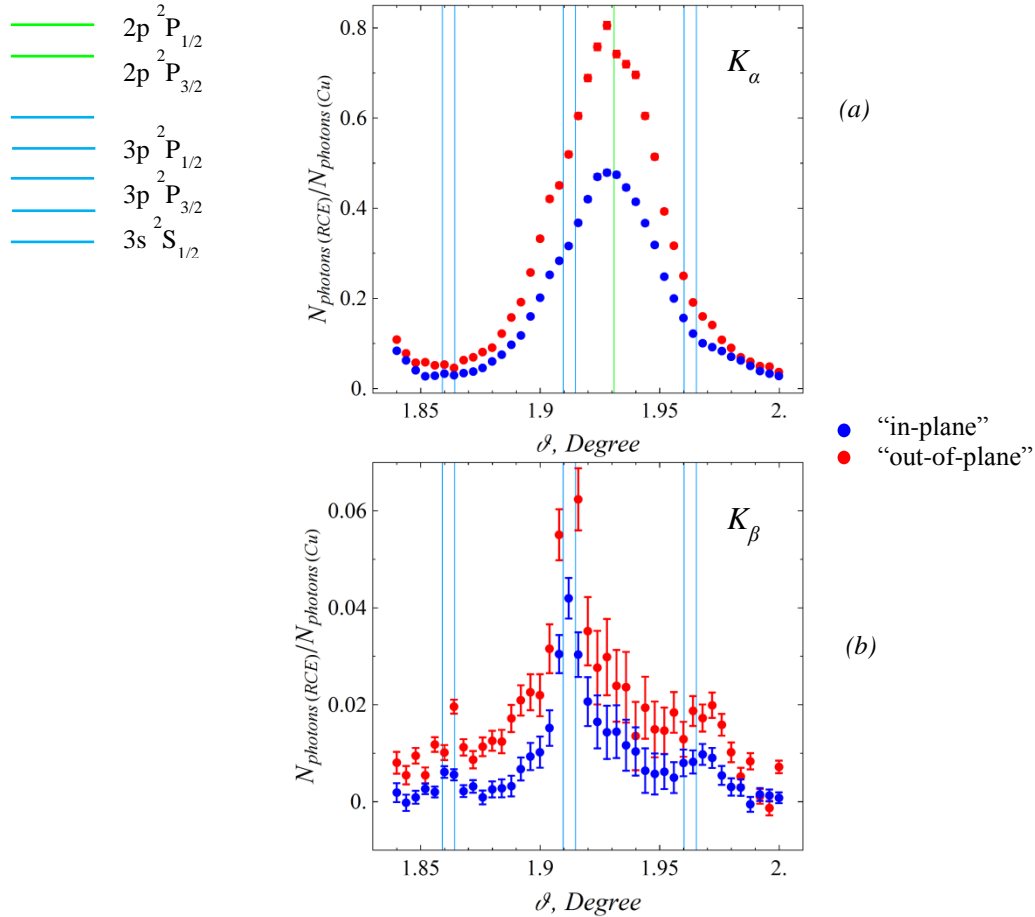
Figure 3.15 *X-ray resonance spectra from the decay of the 3s $^2S_{3/2}$, 3d $^2D_{3/2}$ and 3d $^2D_{5/2}$ excited states of the 390 MeV/u Ar^{17+} ions coherently excited in a Si crystal: K_α (a) and K_β (b) X-ray emission measured as a function of θ rotation angle. The error bar is given by the statistical error of the measurements.*

This algorithm was used to obtain all resonance X-ray spectra from H-like Ar presented in the next chapter. In the case of He-like projectiles the measured X-ray spectra are more complex and contain photons emitted from the decay of the excited states in He-like and H-like ions as well. The H-like ions are created due to ionization in random collisions. The ionization of the excited states of He-like ions has comparable probability as the photon decay.

Typical X-ray spectra emitted from He-like ions are shown in figure 3.16. In these spectra contributions from the K_α, Ly_α, K_β and Ly_β can be seen but cannot be clearly separated due to the limited energy resolution of the detectors. Therefore, for the evaluation of the X-ray

emission from the He-like ions a sum the K_α and Ly_α emission has been obtained instead of considering the Ly_α yield. A wide range of the spectrum was integrated to obtain sum of the K_β and Ly_β lines. The integration intervals are listed in table 3.3.

Table 3.3 *The integration intervals*

Detector	Integration intervals		
	K_α	$K_\alpha + L_\alpha$	$K_{\beta+}\ Ly_\beta$
SiLi	875-975	885-1085	1085-1285
Ketek	1000-1150	980-1280	1280-1580
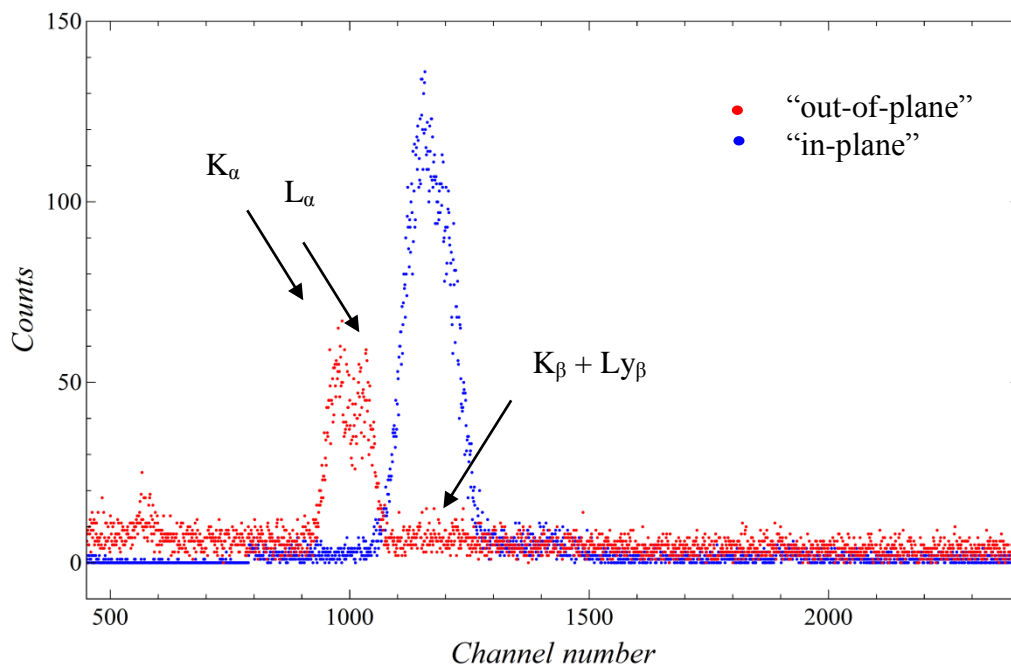
Figure 3.16 *X-ray spectra from the decay of the excited 3p $^2P_{3/2}$, 3s $^2S_{1/2}$, 3d $^2D_{3/2}$ and 3d $^2D_{5/2}$ states in He-like Ar ions measured by "in-plane" and "out-of-plane detectors.*

4 Results

In the present work the Resonant Coherent Excitation (RCE) and Double Resonant Coherent Excitation (DRCE) of relativistic H-like and He-like Ar ions from the ground state into the n = 2, 3, 4 and 5 states were observed by means of the interaction of the ions with a 1 μm Si-crystal target. The RCEs and DRCEs have been indicated from the resonance curves obtained by measuring the charge-state distribution of the ions after passing the crystal and the photon yield emitted from the decay of the excited states, depending on the crystal orientations. The obtained resonant curves for the charge-states and X-rays are summarized in the present chapter. The charge-state resonance curve represents the survival fraction of the ions initial charge-state measured as a function of the angle θ between the $[\bar{1}10]$ axis in the (220) plane and the incident beam direction. The X-ray resonance curves are the yields of the K_α or K_β X-rays from the decay of the projectile excited states measured also as a function of the angle θ. The charge-state and the X-ray resonance curves have been measured at the same resonance conditions and mostly within the same θ angular range with a step of 0.01° or 0.0025° depending on the structure of the expected resonance profile. However, the two measurements could not be performed simultaneously due to the different beam intensity required for the ion and photon yield accumulation and the rate-dependent efficiency of the particle detector (see details in chapter 3). For some of the excited states in H-like Ar the X-ray emission has been measured only at the maximum of the resonance due to the low count rate and limited experimental time. The method used to obtain the charge-state and the X-ray resonance spectra from the raw data were presented in chapter 3, "Data analysis".

4.1 Resonant Coherent Excitation in 455 MeV H-like Ar

The process of RCE into the $n = 2, 3, 4$ and 5 levels in H-like Ar ions passing a 1 μm Si-crystal has been investigated using the ion beam at 455 MeV/u. The beam energy was chosen according to the excitation energy of the different levels of projectile ions. The orientation of the target used for the measurements was defined from the calculation of the resonance conditions performed for different transitions in Ar^{17+} using the resonance equation (2.7). The transition energies used for this calculation were taken from the NIST database [4.1] (see table 4.1 below).

Table 4.1 *Transition energies from the ground state in Ar^{17+} [4.1]*

Level	Energy, eV
2p $^2P_{3/2}$	3322.9919
3p $^2P_{1/2}$	3934.29322
3p $^2P_{3/2}$	3935.72056
3s $^2S_{1/2}$	3934.34020
3d $^2D_{3/2}$	3935.718064
3d $^2D_{5/2}$	3936.190044
4p $^2P_{1/2}$	4149.37430
4p $^2P_{3/2}$	4150.33984
4s $^2S_{1/2}$	4149.75781
4d $^2D_{3/2}$	4150.338769
4d $^2D_{5/2}$	4150.537956
5p $^2P_{1/2}$	4249.37430
5p $^2P_{3/2}$	4249.682358
5s $^2S_{1/2}$	4249.38451
5d $^2D_{3/2}$	4249.681812
5d $^2D_{5/2}$	4249.783800

The angular range scanned in the present measurement is shown in figure 4.1. The lines with different colors correspond to the angular orientations of the target satisfying single resonance conditions for the coherent excitation of different levels in the projectile ions. If two different resonant conditions are satisfied by the same angular orientation a DRCE may occur. The arrows on the right-hand side of figure 4.1 show the condition of the φ angle for each θ scan. The charge-state measurements have been done as a function of the angle θ with a step of 0.0025° over an angular range of 0.25° kipping φ constant. The ion yield was accumulated by the PSD for 5×10^4 incoming particles for each angular orientation. These measurements have been performed using strongly reduced beam intensity (see chapter 2).
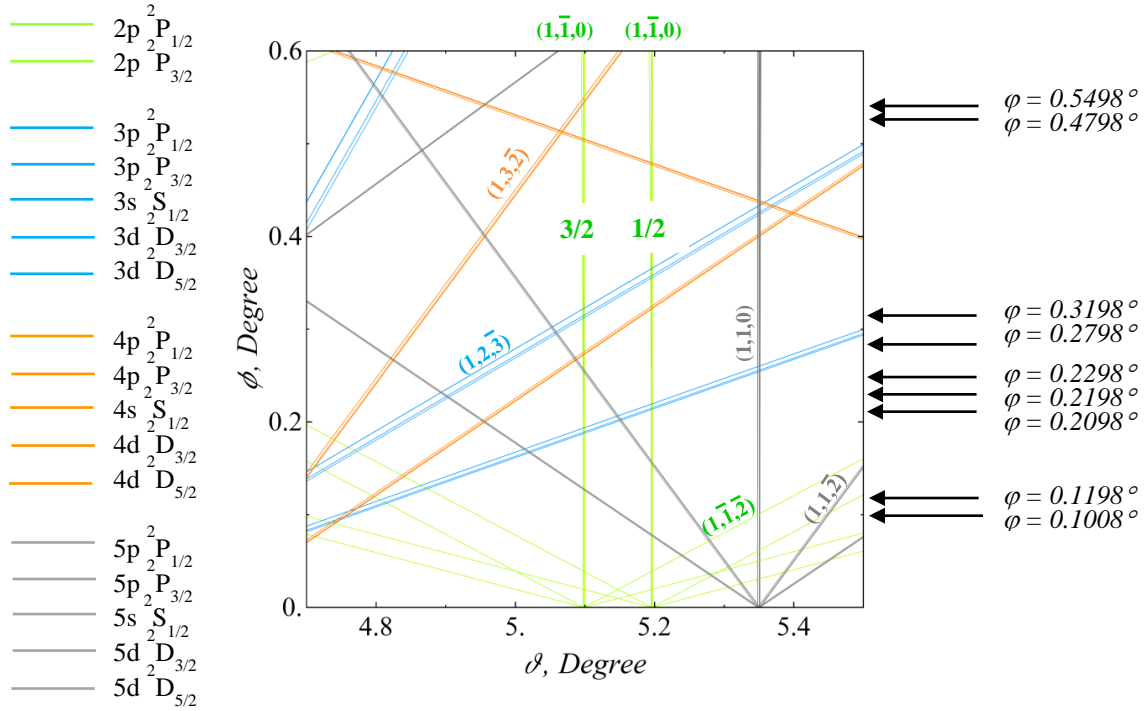
Figure 4.1 *Resonance conditions for transitions from the ground state in 455 MeV/u Ar^{17+}.*

The mechanism of RCE and DRCE in H-like Ar is shown in figure 4.2. Considering the electric dipole transitions, an RCE from the ground state 1s $^2S_{1/2}$ is possible into the np $^2P_{1/2}$ and np $^2P_{3/2}$ excited states, where n is the principal quantum number. Possible transitions up to $n = 3$ are represented in the figure. A DRCE in H-like ions may occur as a sequential excitation via one of the 2p states: 1s $^2S_{1/2} \rightarrow$ 2p $^2P_{1/2}$/2p $^2P_{3/2} \rightarrow$ ns $^2S_{1/2}$, nd $^2D_{3/2}$ and nd $^2D_{5/2}$.
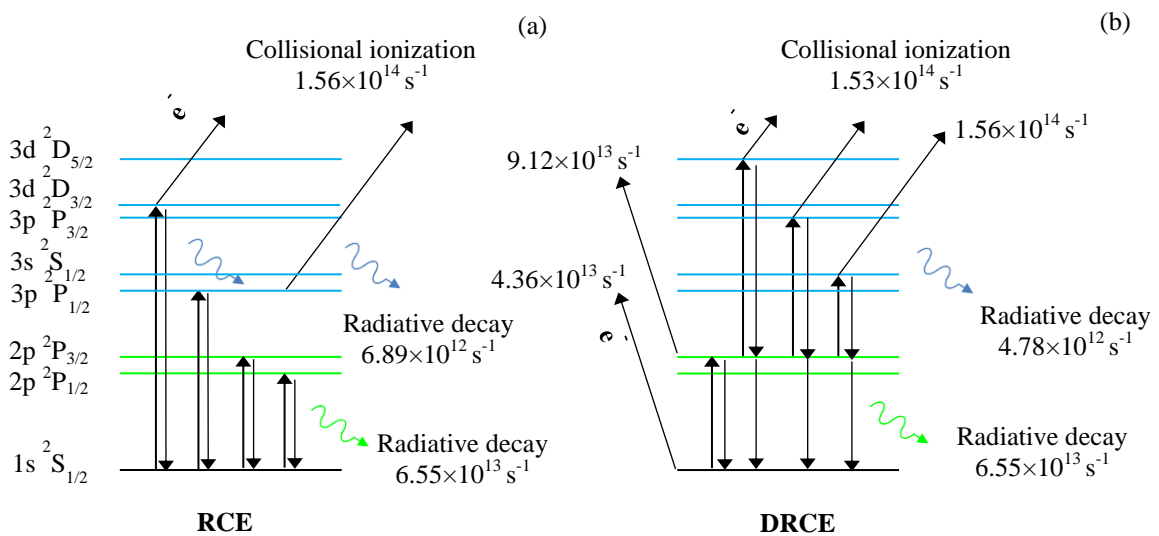
Figure 4.2 *RCE (a) and DRCE (b) in 455 MeV/u Ar^{17+}. The rates for the collisional ionization are based on a cross section of [1.13] (see sections 1.2.4).*

4.1.1 The charge-state resonance

In figure 4.2 the probabilities of the collisional ionization and the decay rates are noted for every state (the calculated numbers were obtained in section 1.2.4). One can see that the ionization probability is increasing for the higher states therefore, a decrease of the initial charge state fraction at the resonance conditions is expected. The experimentally observed RCEs will be examined by comparing the resonance depths defined as a difference between the initial charge-state fractions F_{random}^{17+} at non-resonance conditions and $F_{resonance}^{17+}$ at the resonance profile minimum.

4.1.1.1 Excitation into the $n = 2$ state

An RCE of H-like Ar ions from the ground into the 2p ^{2}P$_{3/2}$ state induced by the $(1,\bar{1},0)$ crystal harmonic has been observed from the charge-state distribution of the ions yield. The charge-state resonance curve is represented in figure 4.3.
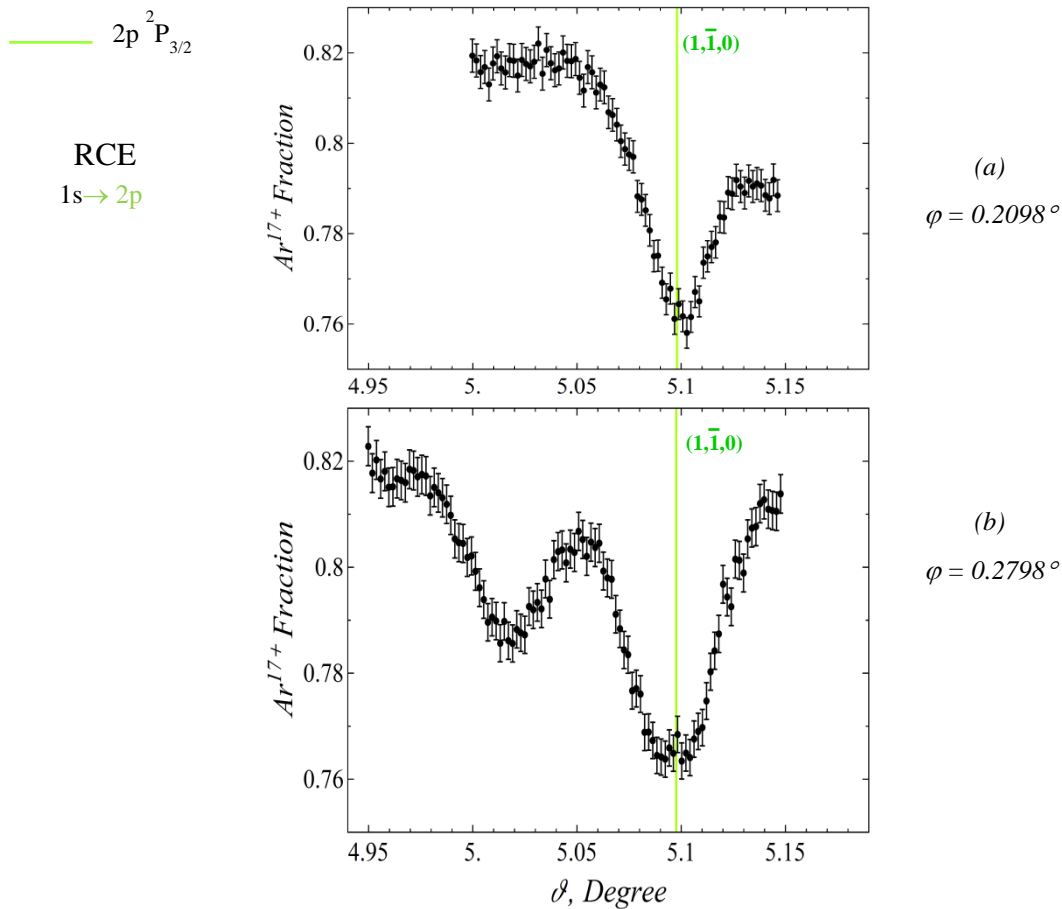
Figure 4.3 *Charge-state resonance curves for 455 MeV/u Ar^{17+} ions passing a Si crystal:*
(a) – RCE for the 1s ^{2}S$_{1/2}$ → 2p ^{2}P$_{3/2}$ transition at $\varphi = 0.2098$°;
(b) – RCE for the 1s ^{2}S$_{1/2}$ → 2p ^{2}P$_{3/2}$ transition at $\varphi = 0.2798$°.

The scanning of the angle θ was performed at two different values of the φ angle, 0.2098° (a) and 0.2798° (b), within the interval from 5° to 5.15°. The resonance curve represents the variation of the number of projectile ions in the initial charge-state (H-like) as a function of the crystal rotation angle θ.

In both measurements, the resonance has an offset and an almost symmetric profile with a minimum at $\theta \approx 5.1°$ (green line in the figure). The offset represents 18% of the total ions and is produced by the projectile ionization in random collisions with the crystal atoms. At the resonance minimum the yield of the H-like projectiles is reduced by another 6%. This can be explained by the fact that the ionization probability (9.12×10^{13} s^{-1}) from an excited state is higher compared with the probability of ionization (4.36×10^{13} s^{-1}) from the ground state. The excited ions which have not been ionized in the crystal decay via photo emission.

The resonance depth is about 6% in both cases. This shows that the probability of the occurrence of an RCE does not change with the crystal orientation in φ direction (for the potential induced by the same crystal harmonic).

4.1.1.2 Excitation into the $n = 3$, 4 and 5 states

A DRCE in H-like Ar ions from the ground state into the $n = 3$ level was observed by the interaction of the projectiles with $(1,\bar{1},0)$ and $(1,2,\bar{3})$ crystal harmonics at the same crystal orientation. Figure 4.4 (a) represents the charge-state resonance curve for the DRCE in Ar^{17+} ions sequentially exited from the 1s $^2S_{1/2}$ into 2p $^2P_{3/2}$ state and further into the 3s $^2S_{1/2}$, 3d $^2D_{3/2}$ and 3d $^2D_{5/2}$ states. The scanning of the angle θ was performed at fixed value of the φ angle, 0.3198°, within the interval from 5° to 5.15°.

The resonance has again an offset of 18% due to the collisional ionization of the ions from the ground state. At the resonance minimum $\theta \approx 5.1°$ the yield of the H-like projectiles is reduced by another 10%.

The ions sequentially excited from the ground state into the 2p $^2P_{3/2}$ state and then into the 3s $^2S_{1/2}$, 3d $^2D_{3/2}$ and 3d $^2D_{5/2}$ states contribute to the resonance peak. The difference between the transition energies is less than 1 eV and the fine structure of the resonance cannot be experimentally observed here.

For a comparison, both components of the DRCE, $n = 2$ and $n = 3$, have been separately studied by performing the scanning at a different φ, 0.2798°, where two transitions occur at different θ values. Two independent RCEs can be seen in the charge-state resonance curve showed in figure 4.4 (b): the left peak is related to the RCE for the 1s $^2S_{1/2} \rightarrow$ 3p $^2P_{1/2}$

and 3p $^2P_{3/2}$ transition at around $\theta \approx 5.01°$ (blue line in the figure) and the right peak is related to the RCE for the 1s $^2S_{1/2} \rightarrow$ 2p $^2P_{3/2}$ transition at around $\theta \approx 5.1°$ (green line in the figure). The resonances appear again on an offset of about 18%, originating in the random collisional projectile ionization process.

The depths of the two different resonances are 3.5% for the transition into the $n = 3$ and 6% for the transition into the $n = 2$ states. In contrast, the observed resonance profile at DRCE conditions was 10%. Which can be explained by the higher collisional ionization probability (2×10^{14}) from the $n = 3$ excited states than from the $n = 2$ state (9.12×10^{13}). The enhancement of the resonance depth at the DRCE conditions, comparing to the RCE into the $n = 2$ state, is the first evidence of the DRCE occurrence.

Figure 4.4 *Charge-state resonance curves for 455 MeV/u Ar^{17+} ions passing a Si crystal:*
(a) – DRCE for the 1s $^2S_{1/2} \rightarrow$ 2p $^2P_{3/2} \rightarrow$ 3s $^2S_{1/2}$, 3d $^2D_{3/2}$ & 3d $^2D_{5/2}$ transitions;
(b) – RCE for the 1s $^2S_{1/2} \rightarrow$ 2p $^2P_{3/2}$ (right peak) and for the 1s $^2S_{1/2} \rightarrow$ 3p $^2P_{1/2}$ and 3p $^2P_{3/2}$ (left peak) transitions;

The RCE and DRCE into the $n = 4$ states observed in H-like Ar ions by the fields of the $(1,\bar{1},0)$ and $(1,3,\bar{2})$ crystal harmonics are summarized in figure 4.5. The deepest resonance profile of 8% is observed at $\theta \approx 5.1°$ and $\varphi = 0.5498°$. It corresponds to a fraction of 0.74 of the initial charge-state (figure 4.5 (a)). This is a sequential DRCE from the 1s $^2S_{1/2}$ into the 2p $^2P_{3/2}$ state and then into the 4s $^2S_{1/2}$, 4d $^2D_{3/2}$ and 4d $^2D_{5/2}$ states. In this case, the resonance depth enhancement of 2% at the DRCE into $n = 4$ is observed comparing to the resonance depth at the RCE into the $n = 2$ state (figure 4.5 (b)).
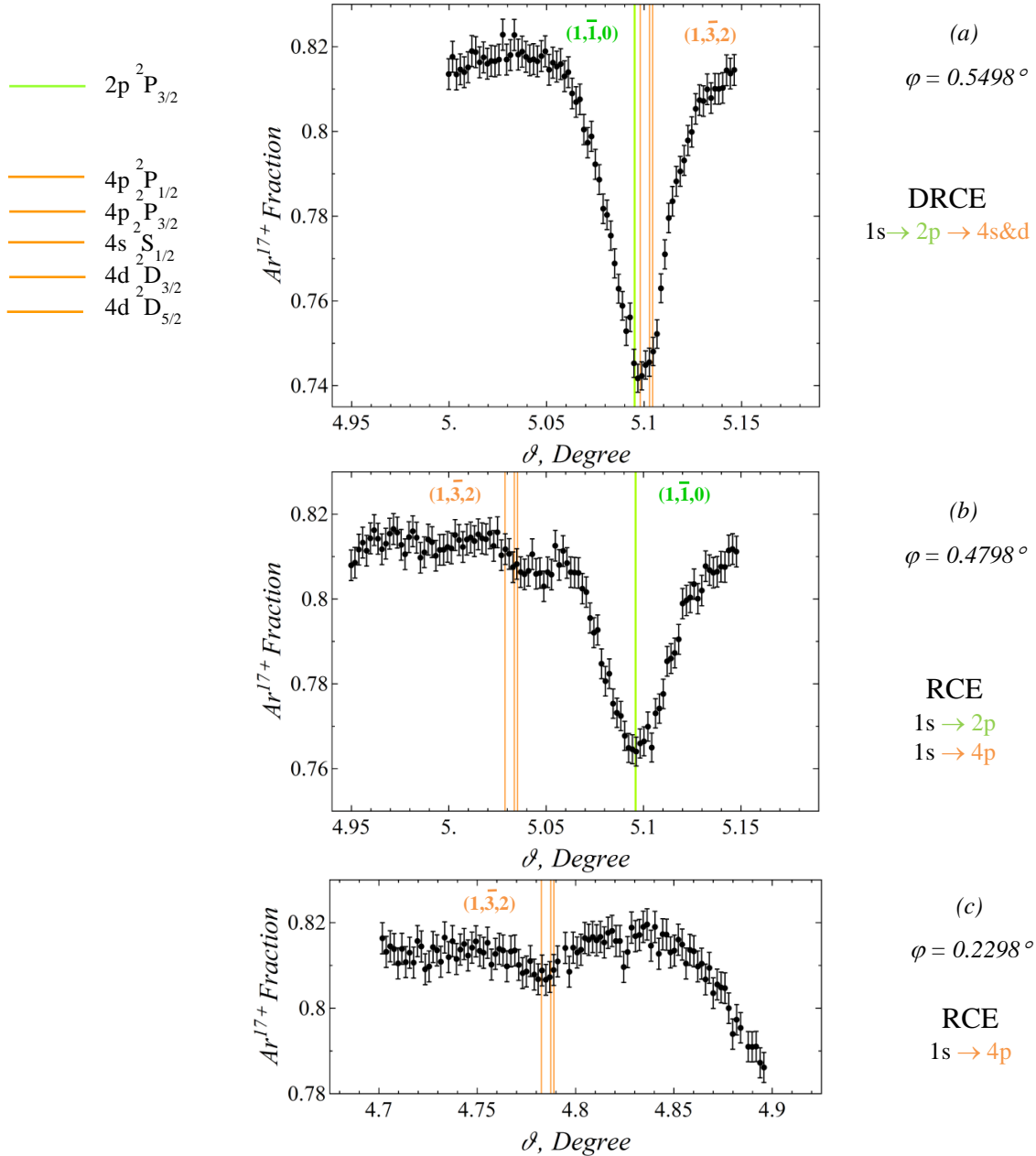
Figure 4.5 *Resonance charge-state curves for 455 MeV/u Ar^{17+} ions passing a Si crystal:*
(a) – DRCE for the 1s $^2S_{1/2} \rightarrow 2p\,^2P_{3/2} \rightarrow 4s\,^2S_{1/2}$, 4d $^2D_{3/2}$ & 4d $^2D_{5/2}$ transition;
(b) – RCE for the 1s $^2S_{1/2} \rightarrow 2p\,^2P_{3/2}$ (right peak) and for the 1s $^2S_{1/2} \rightarrow 4p\,^2P_{1/2}$ and 4p $^2P_{3/2}$ transitions (left peak);
(c) – RCE for the 1s $^2S_{1/2} \rightarrow 4p\,^2P_{1/2}$ and 4p $^2P_{3/2}$ transitions

At $\varphi = 0.4798°$ the coherent excitation occurs as two independent processes of an RCE from the ground state into the 4p $^2P_{1/2}$ and 4p $^2P_{3/2}$ states at $\theta \approx 5.04°$ and RCE into the 2p $^2P_{3/2}$ state $\theta \approx 5.1°$ (figure 4.5 (b)). Figure 4.5 (c) shows the result of another RCE observation into the 4p $^2P_{1/2}$ and 4p $^2P_{3/2}$ states at $\varphi = 0.2298°$. This measurement demonstrates only about 1% additional reduction of the survival fraction.

The DRCE for the 1s $^2S_{1/2} \rightarrow$ 2p $^2P_{3/2} \rightarrow$ 5p transition was obtained using the same projectile beam and within the θ interval from 5.2° to 5.5° keeping $\varphi = 1.008°$ (figure 4.6 (a)). The DRCE from the 2p $^2P_{3/2}$ into the 5p states is observed at $\theta \approx 5.35°$ and was induced by the $(1,3,0)$ and $(1,\bar{1},2)$ crystal harmonics (left peak in figure 4.6 (a)). The $^2S_{1/2}$, $^2D_{3/2}$ and $^2D_{5/2}$ components are contributing to the resonance peak.

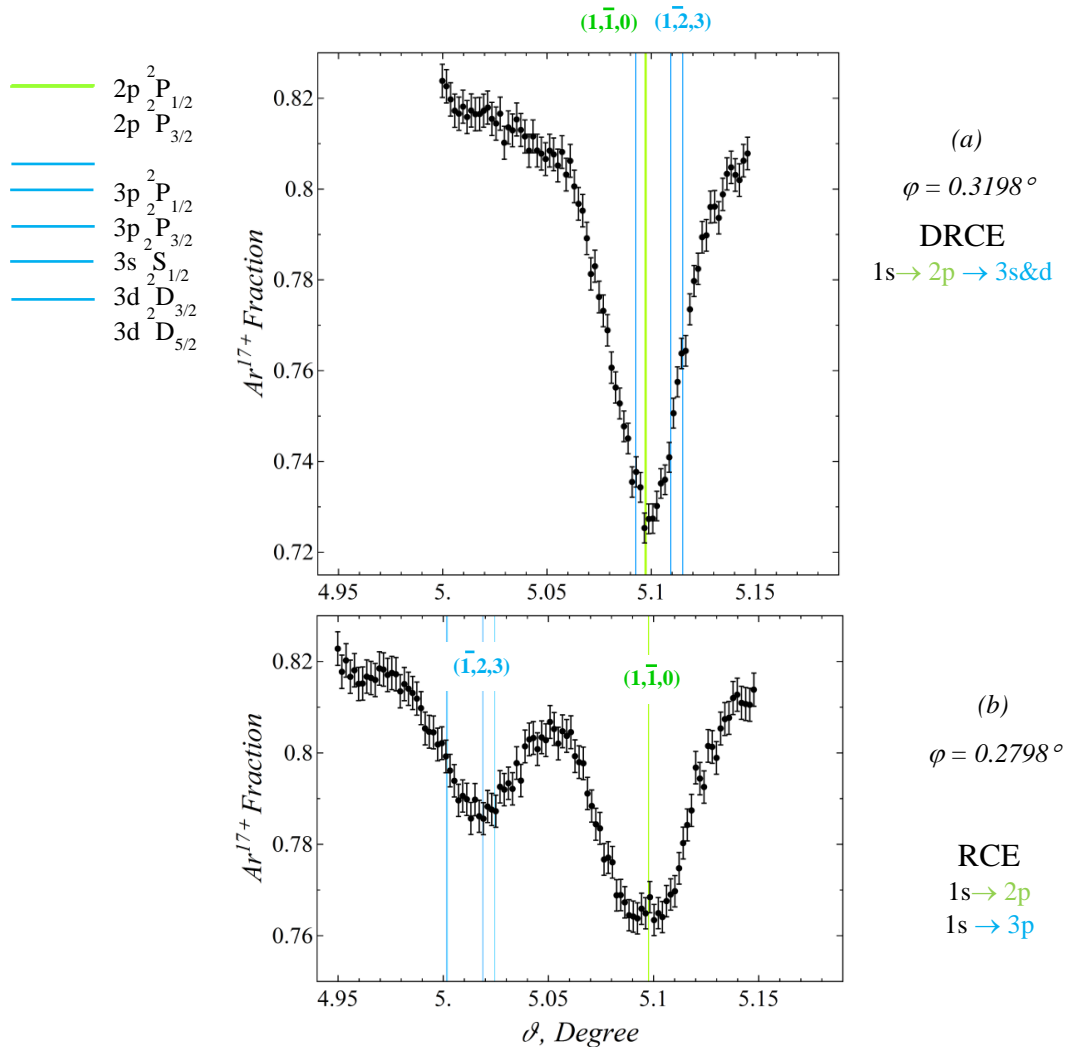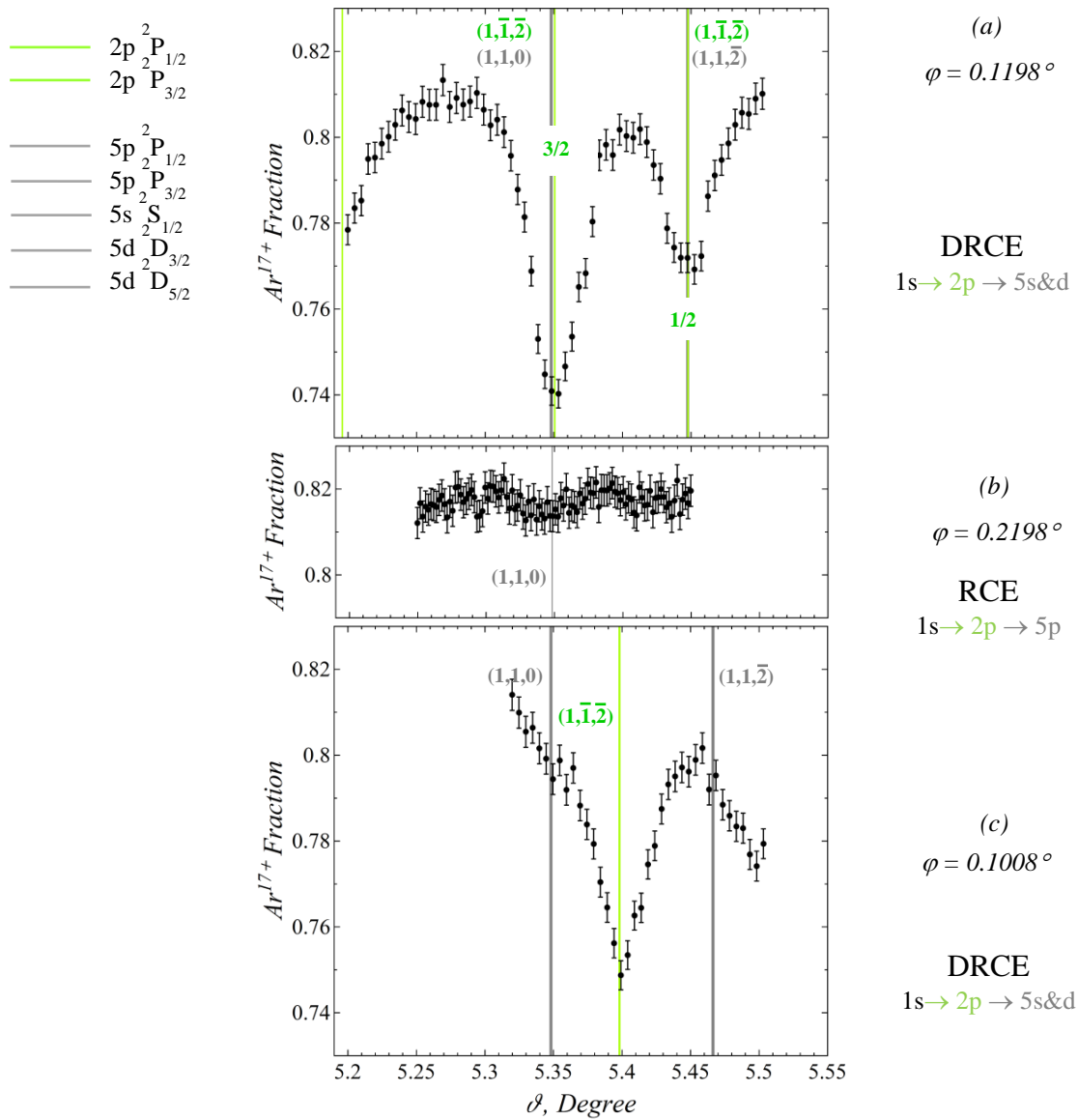Figure 4.6 *Charge-state resonance curves of 455 MeV/u Ar^{17+} ions in the S crystal: (a) and (b) – DRCE for the 1s $^2S_{1/2} \rightarrow$ 2p $^2P_{1/2} \rightarrow$ 5s $^2S_{1/2}$, 5d $^2D_{3/2}$ & 5d $^2D_{5/2}$ (left peak) and for the 1s $^2S_{1/2} \rightarrow$ 2p $^2P_{3/2} \rightarrow$ 5s $^2S_{1/2}$, 5d $^2D_{3/2}$ & 5d $^2D_{5/2}$ (right peak) transitions; (c) – RCE for the 1s $^2S_{1/2} \rightarrow$ 5p $^2P_{1/2}$ and 5p $^2P_{3/2}$ transitions.*

82

A second DRCE into the $n = 5$ level induced by $(1,\bar{1},2)$ and $(1,3,\bar{2})$ crystallographic planes was detected at $\theta \approx 5.45°$ for the same φ value (right peak in figure 4.6 (a)). This DRCE is an excitation via the 2p $^2P_{1/2}$ state. The DRCEs occur with different probabilities as seen from the difference in the depth of the two curves: 7% and 4%. This difference can be explained by the polarization direction of the oscillating field. When the polarization of two harmonics inducing a DRCE is not parallel, the probability of the second step of the sequential excitation is decreasing [4.2].

A direct excitation into the 5p states was tried to detect at $\varphi = 1.2198°$ (see figure 4.6 (b)). The peak is expected at $\theta \approx 5.34°$ but in the experimental spectrum no clear signature of the excitation in the initial charge-state fraction could be observed.

The first DRCE (left peak in figure 4.6 (a)) observed at $\theta \approx 5.35°$ have been measured at a different value of $\varphi = 1.1198°$. Here the $n = 5$ peak can be seen at $\theta \approx 5.35°$ separately from the $n = 2$ component (figure 4.6 (b)). The resonance depth is about 2%. This means that a DRCE can be observed if two resonances at least are overlapping within their width. In principle, the exact coincidence of the two resonance conditions is not required. A summary of the double and single excitations discussed above is given in table 4.2.

Table 4.2 *Experimentally observed RCEs and DRCEs in H-like Ar*

Transition			Res. depth, %	(k,l,m)	$\theta,°$	$\varphi,°$
RCE	1s $^2S_{1/2} \rightarrow$ 2p $^2P_{3/2}$		6	$(1,\bar{1},0)$	5.1	0.2098
RCE	1s $^2S_{1/2} \rightarrow$	3p $^2P_{1/2}$ 3p $^2P_{3/2}$	4	$(1,2,\bar{3})$	5.0	0.2798
DRCE	1s $^2S_{1/2} \rightarrow$ 2p $^2P_{3/2} \rightarrow$	3s $^2S_{1/2}$ 3d $^2D_{3/2}$ 3d $^2D_{5/2}$	10	$(1,\bar{1},0)$ $(1,2,\bar{3})$	5.1	0.3198
RCE	1s $^2S_{1/2} \rightarrow$	4p $^2P_{1/2}$ 4p $^2P_{3/2}$	1.5	$(1,3,\bar{2})$	4.79	0.2298
DRCE	1s $^2S_{1/2} \rightarrow$ 2p $^2P_{3/2} \rightarrow$	4s $^2S_{1/2}$ 4d $^2D_{3/2}$ 4d $^2D_{5/2}$	6	$(1,\bar{1},0)$ $(1,3,\bar{2})$	5.1	0.5498
RCE	1s $^2S_{1/2} \rightarrow$	5p $^2P_{1/2}$ 5p $^2P_{3/2}$	< 1	$(1,1,0)$	5.1	1.2198
DRCE	1s $^2S_{1/2} \rightarrow$ 2p $^2P_{3/2} \rightarrow$	5s $^2S_{1/2}$ 5d $^2D_{3/2}$ 5d $^2D_{5/2}$	6	$(1,1,0)$ $(1,\bar{1},\bar{2})$	5.35	1.0080

4.1.2 The X-ray resonances

If the enhancement of the resonance depth is related to the DRCE phenomenon, a simultaneous reduction of the K_α emission is expected due to the population transfer from the $n = 2$ into the higher excited state. Therefore, the X-rays emitted from the decay of the coherently excited $n = 2, 3, 4$ and 5 states of the 455 MeV/u Ar^{17+} ions have been measured at the DRCE, RCE and non-resonance conditions. The resonance conditions were defined from the angular diagram (figure 4.1) and roughly compared with the previously obtained charge-state resonance spectra. The X-rays have been accumulated by the "in-plane" detector installed in the goniometer chamber under the 45 degrees observation angle relatively to the beam axis.

The energy calibration and the Doppler correction have been applied for all measured spectra using the algorithm explained in chapter "Data analysis". The accumulation time of the photons was adjusted depending on the transition probability therefore measured spectra had to be normalized by the number of photons registered by the detector installed at the end of the beam line, behind a Copper foil. The geometry of the X-ray detector was not precisely defined therefore, only a relative normalization of the X-ray spectra could be performed.

The X-ray yields from the decays of the 2p, 3p, 3s and 3d excited states in Ar^{17+} ions are presented in figure 4.7. The spectrum 4.7 (a) was measured at the double resonance conditions given by the $(1,\bar{1},0)$ and $(1,2,\bar{3})$ crystal orientations by placing the target at $\theta = 5.0962°$ and $\varphi = 0.3198°$ angles relatively to the beam axis. This is a sequential DRCE from the ground state into the 2p $^2P_{3/2}$ state and then into the 3s $^2S_{1/2}$, 3d $^2D_{3/2}$ and 3d $^2D_{5/2}$ states.

The spectrum 4.7 (b) is the X-ray emission from the directly excited 2p $^2P_{3/2}$ state by the potential of the $(1,\bar{1},0)$ crystallographic orientation. The spectrum 4.7 (c) was measured from the decay of the directly excited 3p $^2P_{1/2}$ and 3p $^2P_{3/2}$ states of the projectile ions induced by the $(1,2,\bar{3})$ crystallographic planes. The background caused by the photons emitted under the non-resonance orientation was subtracted from all X-ray spectra. Therefore these spectra contain only the photons emitted from the decay of the coherently excited states. In all three spectra a peak around 3.3 keV is observed. This energy corresponds to the energy of the K_α photons emitted by the decay of the 2p $^2P_{3/2}$ state into the ground state. The spectra 4.7 (a) and (c) show an additional peak at around 3.9 keV corresponding to the K_β photons emitted from the decay of the 3s $^2S_{3/2}$, 3d $^2D_{3/2}$ and 3d $^2D_{5/2}$ states with energy of 3934.34013 eV, 3935.717996 eV and 3936.189976 eV respectively [4.1]. To separate the fine structure components one requires an energy resolution of the X-ray detector better than 10^{-4}. The

energy resolution of the detector was estimated from the energy calibration to be at the level of 10^{-2} (see chapter 2).

The K_{α} X-ray emission at the DCRE conditions (spectrum (a)) is reduced comparing to the RCE into the $n = 2$ state (spectrum (b)). This reduction is caused by the population transfer from the 2p $^2P_{3/2}$ state into the 3s $^2S_{1/2}$, 3d $^2D_{3/2}$ and 3d $^2D_{5/2}$ states, i.e. due to the DRCE.
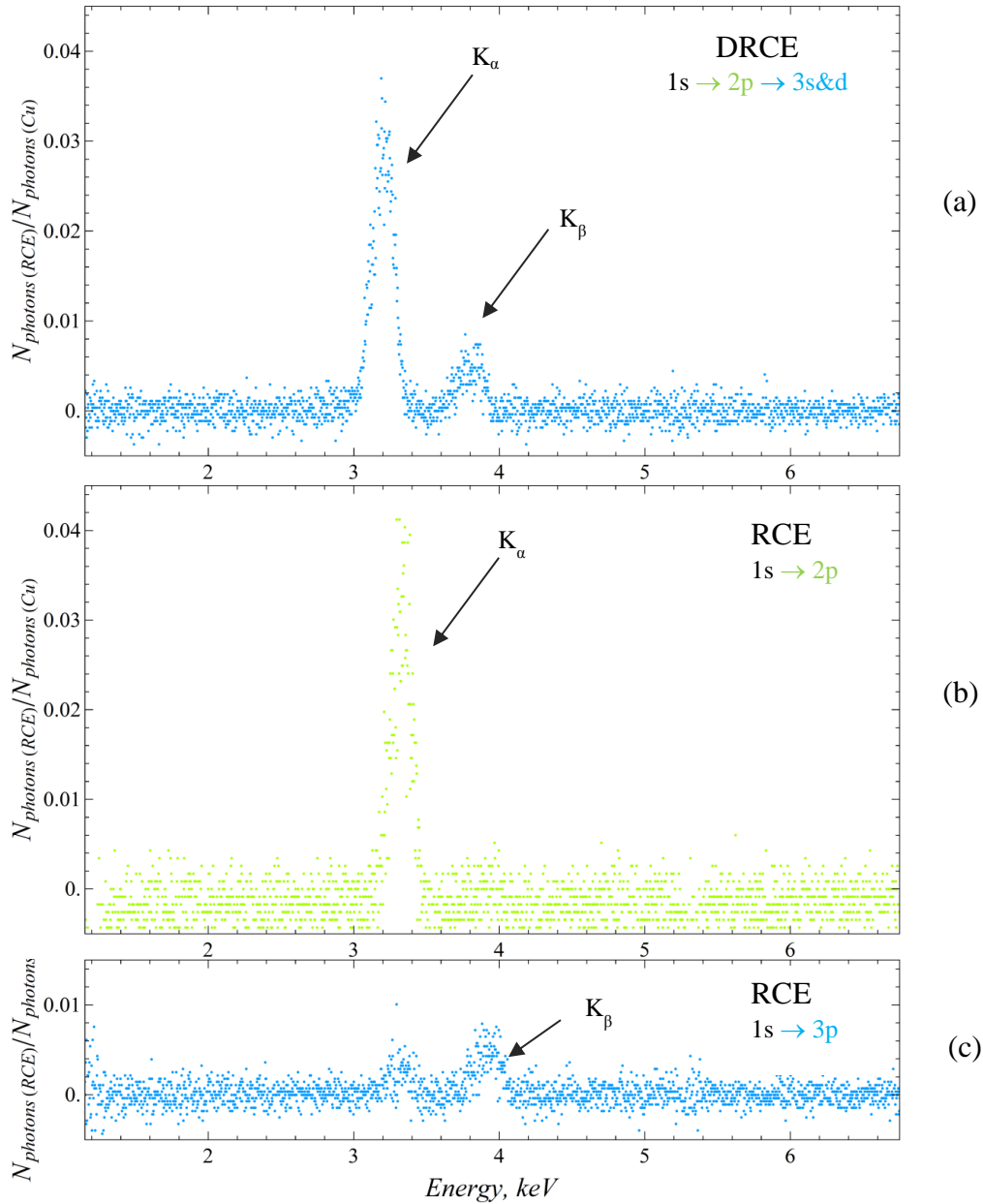

Figure 4.7 *X-ray emission spectra of the 455 MeV/u Ar^{17+} ions coherently excited in a Si crystal: decay of the excited states at the (a), DRCE conditions into the 2s and 3d states (b) RCE condition into the 2p $^2P_{1/2}$ and 2p $^2P_{3/2}$ states (c) RCE conditions into the 3p $^2P_{1/2}$ and 3p $^2P_{3/2}$ states.*

The K_β X-ray emission is observed in two cases: under the DRCE (spectrum 4.7 (a)) and under RCE conditions into the $n = 3$ state (spectrum 4.7 (c)). The K_β photons emitted at the DRCE conditions are related to the radiative decay of the 3p $^2P_{1/2}$ and 3p $^2P_{3/2}$ states. Because the resonance conditions for the 1s $^2S_{1/2} \rightarrow$ 3p $^2P_{1/2}$ and 3p $^2P_{3/2}$ direct transitions are satisfied simultaneously with the DRCE conditions due to the close values of the 3s, 3d and 3p level energies (see the resonance diagram in figure 4.1). Another possible origin of the K_β emission at the DRCE conditions is the decay of the 3p states produced due to the collisional mixing of the ions sequentially excited into the 3s and 3d states. The radiative decay rate from the $n = 2$ states (6.59×10^{13} s^{-1}) is significantly higher than from the $n = 3$ state (6.89×10^{12} s^{-1}) which explains a better statistics of the measured K_α X-rays comparing to the K_β X-rays detected in the same spectrum. The dynamics of the K_α and K_β X-ray emission as function of the crystal orientation can be studied by performing the scanning of the rotations angle, as is was done for the charge-states.

The photons emitted from the decay of the $n = 4$ excited sates of Ar^{17+} ions via DRCE induced by the $(1,\bar{1},0)$ and $(1,3,\bar{2})$ crystallographic planes in Si have been measured at $\theta = 5.0962°$ and $\varphi = 0.55°$. Figure 4.8 shows the measured X-ray spectrum.
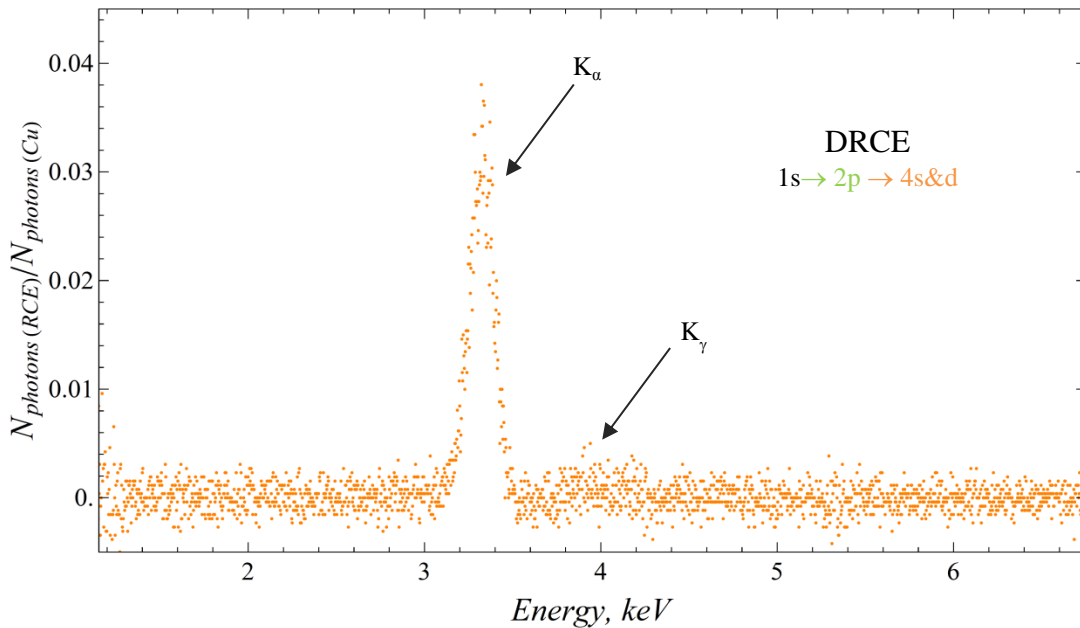
Figure 4.8 *Photon emission from the decay of the n = 4 states of Ar^{17+} ions coherently excited in a Si crystal at the DRCE conditions.*

The spectrum shows only one prominent line, at about 3.3 keV. No line around 3.9 keV was observed in this measurement where photons emitted by the decay of the 4s $^2S_{1/2}$ 4d $^2D_{3/2}$ and 4d $^2D_{5/2}$ states are expected. The reason for this result lays in the lower radiative decay rate of the $n = 4$ states (1.62×10^{12} s^{-1}) combined with the limitation of the measurement

statistics whereas the collisional excitation probability from these states is relatively high $(2.86 \times 10^{14}\ \text{s}^{-1})$.

To observe a DRCE into the 5p states of Ar^{17+} ions, the crystal target was positioned at $\theta = 5.36°$ and $\varphi = 0.101°$. The excitation potential was induced by the $(1,3,0)$ and $(1,\bar{1},2)$ crystal harmonics. The measured decay spectrum is presented in figure 4.9. This is a DRCE via another intermediate state, 3p $^{2}\text{P}_{1/2}$, therefore the K_{α} X-ray emission should not be compared with the one detected in the previous spectra. The K_{δ} X-ray emission is not registered at around expected position (3.9 keV) in the spectrum. A gain because of the increased collisional ionization probability $(3.17 \times 10^{14}\ \text{s}^{-1})$ and decreased radiative decay rate from the $n = 5$ states $(5.29 \times 10^{11}\ \text{s}^{-1})$.
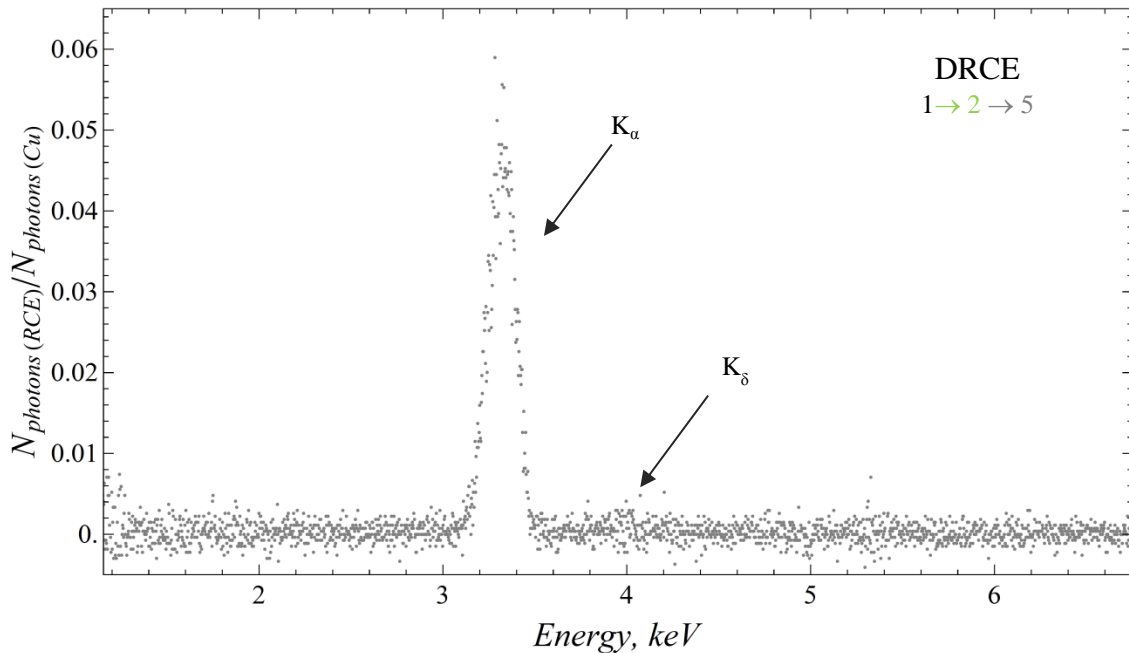
Figure 4.9 *X-ray emission from the decay of the n = 5 states of 455 MeV/u Ar^{17+} ions excited in a Si crystal at the DRCE conditions.*

The performed experiment has demonstrated an enhancement of the resonance profile depth at DRCE conditions into the $n = 3$, 4 and 5 states, compared to an RCE into the $n = 2$ level, simultaneously with the population transfer from the $n = 2$ excited state into the higher levels. The result suggests to investigate a variation of the K_{α} and K_{β} X-ray emission as a function of the rotation angle within the same range as the charge-states.

4.2 Resonant Coherent Excitation in 390 MeV/u H-like Ar

The experiment with H-like Ar was later repeated using different resonance conditions illustrated in figure 4.10. The angular diagram was calculated using formula (2.7) considering electric dipole transitions in H-like Ar for the $n = 2$ and $n = 3$ states. The levels energies were taken for this calculation from the NIST database [4.1] (see table 4.3).

Table 4.3 *Transition energies from the ground state in Ar^{17+} [4.1]*

Level	Energy, eV
2p ^{2}P$_{1/2}$	3318.1760
2p ^{2}P$_{3/2}$	3322.9919
3p ^{2}P$_{1/2}$	3934.29322
3p ^{2}P$_{3/2}$	3935.72056
3s ^{2}S$_{1/2}$	3934.34020
3d ^{2}D$_{3/2}$	3935.718064
3d ^{2}D$_{5/2}$	3936.190044

For these measurements the angle φ was fixed at 0.1° and the θ angle was varied from 1.69° to 2° and the beam energy was chosen to be 390 MeV/u in order to induce the second step of the DRCE by the high l Miller index harmonics which provide a narrower width of the measured resonance. This can be seen already from the angular diagram presented in figure 4.10. Blue lines are steeper than in the previous experiment (figure 4.1)

Figure 4.10 *RCE conditions for 390 MeV H-like Ar ions passing a Si-crystal. The calculation was performed for the Miller indices: k =1,-11 < l < 11 and -3< m < 3.*

4.2.1 The charge-state resonance

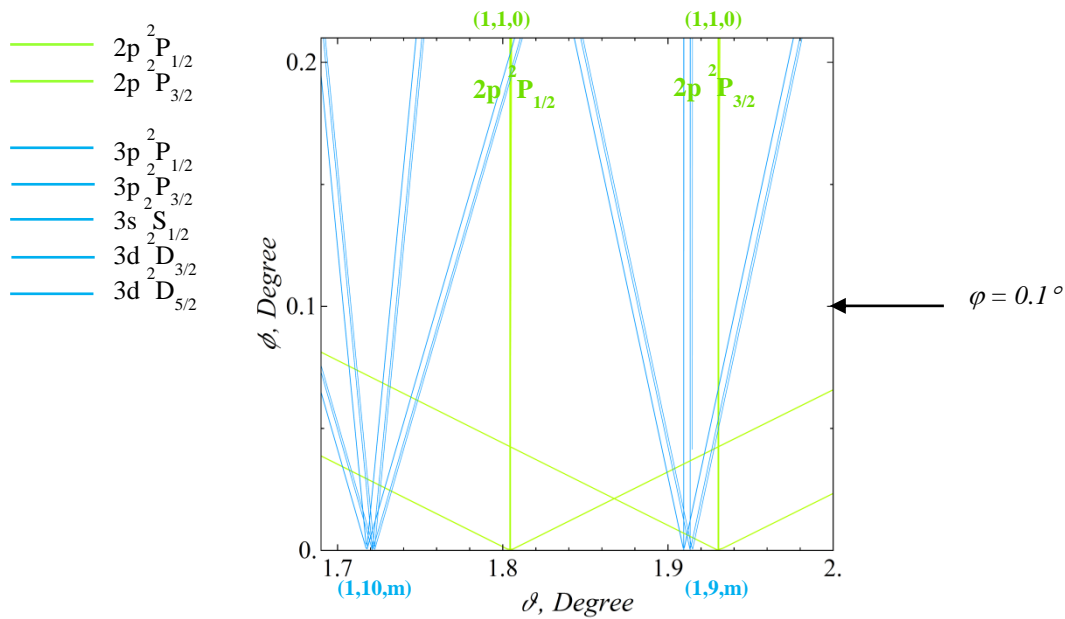The charge-state and X-ray resonance curves obtained by the scanning of the angle θ at $\varphi = 0.1°$ are presented in figure 4.11. The φ angle for the scanning has been chosen in such a way that the two resonances are satisfied within their width at this value but do not overlap at their maxima, as it was in the previous experiment. This allows to observe the DRCE 1s $\to$ 2p $\to$ 3s and 3d in the charge-state resonance curve separately from the direct RCE 1s $\to$ 2p.

Similar to the previous results, the charge-state resonance curve has an offset of about 19% caused by the ionization of the projectiles in random collisions with the target atoms. As it was calculated in section 1.2.4, the probability of the collisional ionization of H-like Ar ions from the ground state at 390 MeV/u (4.36×10^{13} s^{-1}) is slightly higher than at 455 MeV/u (4.44×10^{13} s^{-1}). Therefore, the offset of the charge-state resonance curves observed in this experiment is increased comparing to the previous one.

The resonance conditions for the 2p, 3p, 3s and 3d transitions are also marked over the resonance graphs (the 2p states – green lines, 3p, 3s and 3d states – blue lines). The fraction of the initial charge-state is reduced from about 0.810 to 0.754 at the $\theta \approx 1.915°$ which satisfies the RCE conditions for the 1s ^{2}S$_{1/2}$ $\to$ 2p ^{2}P$_{3/2}$ transition which is caused by the higher probability of the collisional ionization from the 2p excited state (9.34×10^{13} s^{-1}) than from the ground state (4.44×10^{13} s^{-1}). A reduction of about 1% of the initial charge-state fraction is observed at the resonance conditions for the 1s ^{2}S$_{1/2}$ $\to$3p ^{2}P$_{1/2}$ and 3p ^{2}P$_{3/2}$ transitions ($\theta \approx 1.70°$, 1.73°, 1.76° and 1.88°). The collisional ionization probability from the 3p states (1.60×10^{14} s^{-1}) is higher than from the 2p state (9.34×10^{13} s^{-1}), however, the probability of the 1s $\to$ 3p transition is lower than the probability of the 1s $\to$ 2p transition. Therefore, the resonance depth in the charge-state curve is only 1% in contrast to the resonance depth of 4% at the 2p conditions. The probabilities for different electric dipole transitions in highly-charged ions excited by a crystal field have been calculated in [4.2] and the collisional excitation probabilities at 390 MeV/u – in section 1.2.4 (see table 1.3).

A DRCE for the 1s ^{2}S$_{1/2}$ $\to$ 2p ^{2}P$_{3/2}$ $\to$ 3s ^{2}S$_{1/2}$, 3d ^{2}D$_{3/2}$ and 3d ^{2}D$_{5/2}$ transitions is expected at θ between 1.91° and 1.93° where the $n = 3$ and $n = 2$ resonance conditions are satisfied within their width. An additional enhancement of the resonance depth to 7.5% is observed at the $\theta \approx 1.91°$ which corresponds to the $n = 3$ condition.
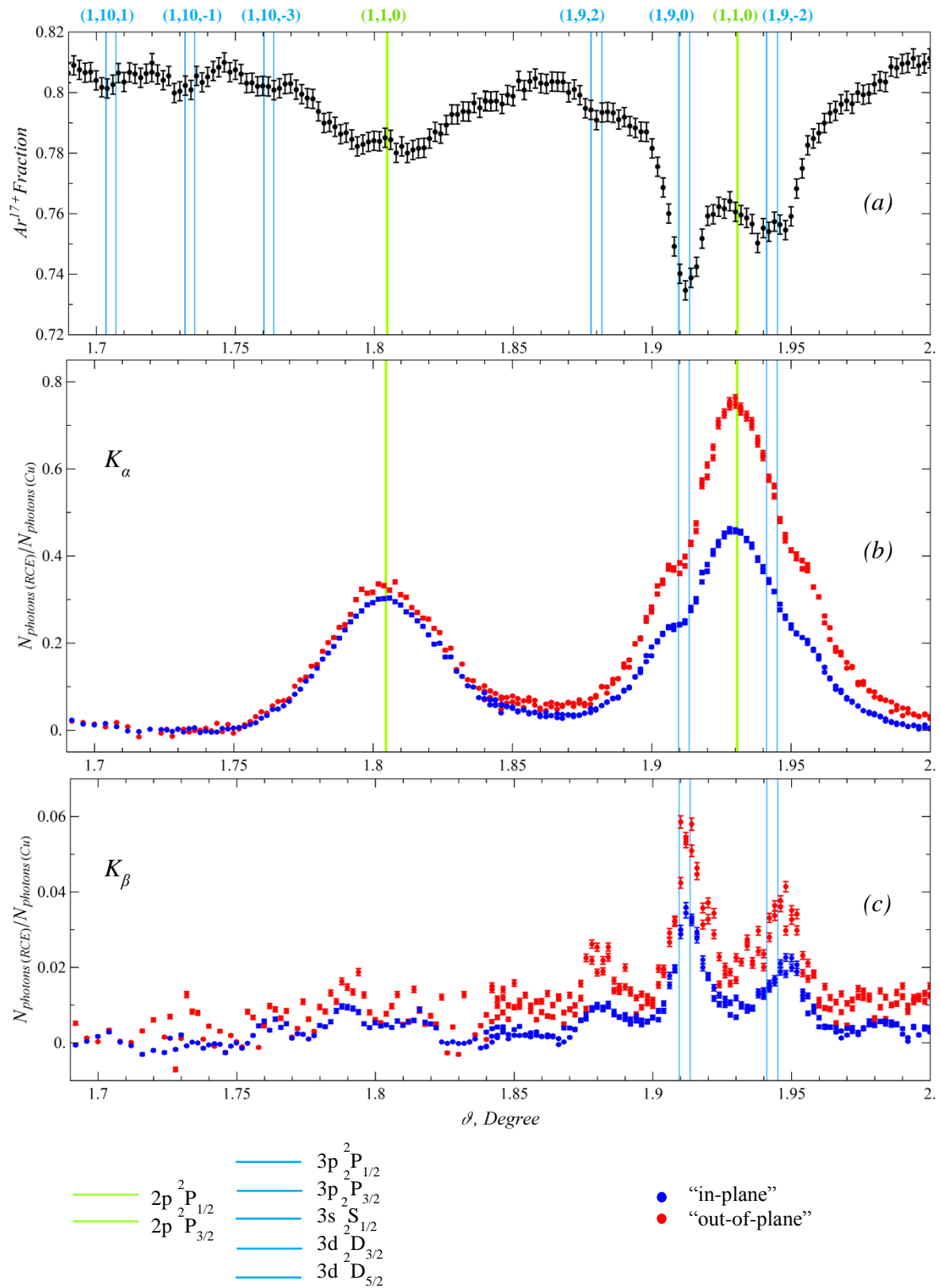
Figure 4.11 *Resonance curves for the 390 MeV/u Ar^{17+} ions excited in a Si crystal at $\varphi = 0.1°$:*
(a) - initial charge-state fraction measured as a function of the rotation angle θ;
(b) and (c) - K_α and K_β X-rays emitted from the decay of the excited n =2 and 3 states.

This is a clear evidence of the DRCE into the $n = 3$ state because the resonance depth for the direct RCE into this state was measured to be only 1-2% (at $\theta \approx 1.70°$, $1.73°$, $1.76°$ and $1.88°$) regardless the value of the Miller index $m = 0, 1, 2$ or 3.

The experimental result is also supported by the calculated probability of the second excitation step 2p $^2P_{3/2} \rightarrow$ 3s $^2S_{1/2}$, 3d $^2D_{3/2}$ and 3d $^2D_{5/2}$ which is few times higher than the probability of the 1s $\rightarrow$ 3p direct transition [4.2]. Therefore, one may conclude that a DRCE occurred here as a sequential excitation from the ground state into the 2p $^2P_{3/2}$ and then into the 3s $^2S_{1/2}$, 3d $^2D_{3/2}$ and 3d $^2D_{5/2}$ states.

4.2.2 The X-ray resonances

The X-ray resonance curves obtained from the decay of the excited states of the Ar ions are presented in figure 4.11 (b) and (c). The X-ray yields were measured within the same angular range as the charge-state distribution. The maximum of the K_α X-ray emission observed at $\theta \approx$ 1.93° value which satisfies the resonance conditions for the 2p $^2P_{3/2}$ transition induced by the $(1,1,0)$ crystallographic orientation. The K_α X-ray emission has a distribution mainly due to the lifetime of the excited state. Processes destroying the coherence, such as angular straggling of the ions in the target, momentum spread and divergence of the ions beam, contribute to the peak width as well.

Another maximum of the K_α X-ray emission observed at $\theta \approx 1.805°$ correspond to the resonance conditions for the 2p $^2P_{1/2}$ transition induced again by the $(1,1,0)$ orientation. A reduction of the K_α emission was registered at the positions for the $n = 3$ resonance condition around $\theta \approx 1.91°$ and $1.95°$. At the same angular orientation ($\theta \approx 1.91°$ and $1.95°$) an enhancement of the K_β X-ray emission was detected (figure 4.11(c)). The origin of the K_α emission reduction and enhancement of the K_β X-ray emission can be analyzed by a comparison of the FWHM of the peaks in eV units.

The θ rotation angle was transformed into the transition energy using the resonance equation (2.7) and the beam energy together with values of the Miller indices chosen for a specific transition. Figure 4.12 shows the K_α X-ray resonance curves in electronvolt scale obtained from the part of the scanning (from 1.79° to 2°) presented in figure 4.11.

The "out-of-plane" and "in-plane" peaks have been fitted with a Gauss function without consideration of the points where the reduction of the emission took place. The position of the maximum of the two peaks was fixed at the literature value fot the transition energy [4.1]. The FWHMs of the K_α peaks observed "out-of-plane" and "in-plane" are 1.88±0.01 eV and 1.89±0.01 eV, respectively. The difference in the peaks height is caused by

the anisotropy of the X-ray emission from the decay of the excited states which will be discussed in section 4.4.
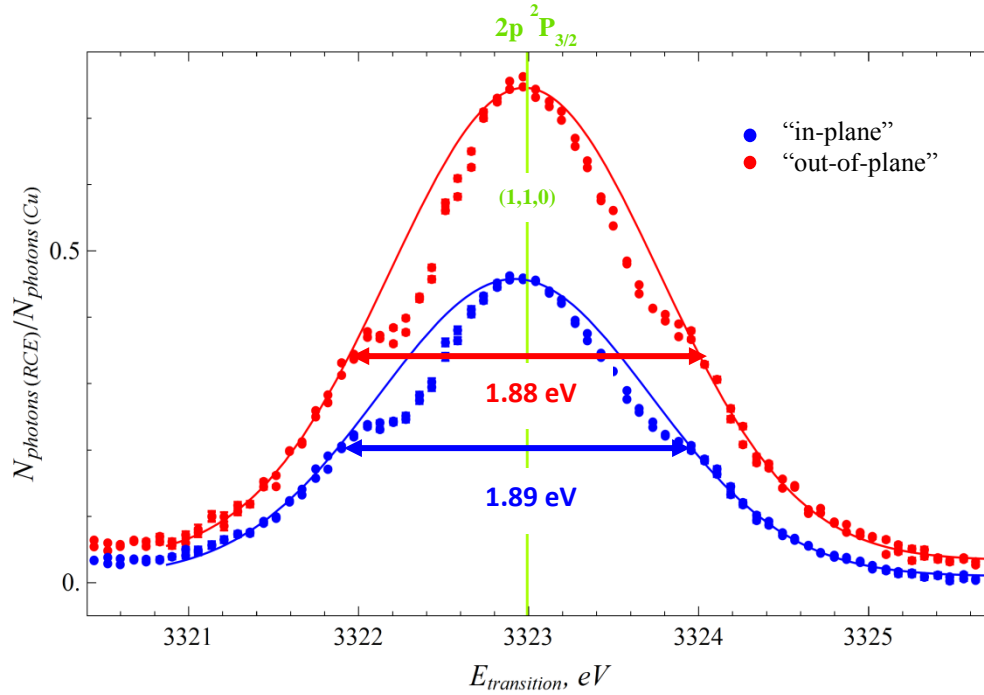
Figure 4.12 *X-ray K_α resonance curves for the 390 MeV/u Ar^{17+} ions excited in a Si crystal at $\varphi = 0.1°$*

A relative reduction $K_{\alpha\,red}$ of the $n = 2$ population has been estimated from the difference of the fit function $K_{\alpha\,fit}$ and the measured number of the K_α photons,

$$K_{\alpha\,red} = \frac{K_{\alpha(fit)} - K_\alpha}{K_{\alpha(fit)}}. \tag{4.1}$$

Figure 4.13 shows the relative reduction of the K_α X-ray emission calculated with formula (4.1) as function of the transition energy. For the calculation the (0,8,0) crystal harmonic induced the intermediate step of the excitation has been considered. Magenta points correspond to the reduction of the K_α X-ray "out-of-plane" emission and green points – to the "in-plane" emission. The peak around 613 eV appears in both spectra. According to the Gaussian fitting of the peaks, both have almost identical width and position (see the parameters in table 4.4). This means equivalence of the decrease of the K_α X-ray emission measured by the "out-of-plane" and "in-plane" detectors. The highest observed relative reduction of the K_α emission is about 25%.

As it was mentioned above, the population transfer from the 2p ^{2}P$_{1/2}$ occurs into the three higher states, 3s ^{2}S$_{1/2}$, 3d ^{2}D$_{3/2}$ and 3d ^{2}D$_{5/2}$. The difference between the energy of these levels is below 1 eV therefore the fine structure cannot be observed in the measurement.
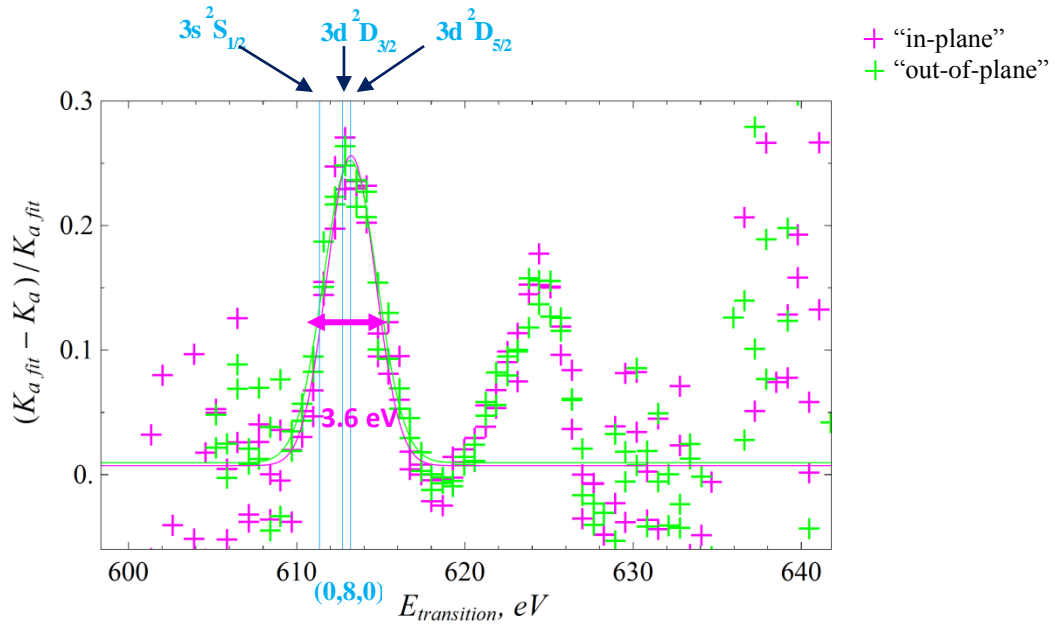
Figure 4.13 *Relative reduction in the K_α X-ray emission for the 390 MeV/u Ar^{17+} ions excited in a Si crystal at $\varphi = 0.1°$*

The peaks at around 622 eV in (figure 4.13) are related to the reduction of the K_α X-ray emission observed due to the DRCE induced by the $(1,9,\bar{2})$ and $(1,1,0)$ crystal harmonics. The asymmetry of the peaks shows different probability of the second excitation step caused by the better or worth overlapping the two conditions, $(1,9,\bar{2})$ and $(1,1,0)$, within their widths The reduction of the K_α X-ray emission does not occur if the two resonances do not overlap within their widths. The peaks position and FWHM can be evaluated in eV by performing the same transformation of the rotation angle into the transition energy considering the $(0,8,\bar{2})$ harmonic for the intermediate step.

The measured K_β X-ray resonance curve in electronvolt scale is shown in figure 4.14. The peak around 3936 eV appears in both curves, "out-of-plane" and "in-plane", and has almost the same FWHM of 4.7±0.3 eV and 4.4±0.2 eV, respectively. The photons emitted by the radiative decay of the directly excited 3p $^2P_{1/2}$ and 3p $^2P_{3/2}$ states equivalently contribute to the measured K_β X-ray emission because the radiative decay rates from these excited states are almost the same [1.35].

93
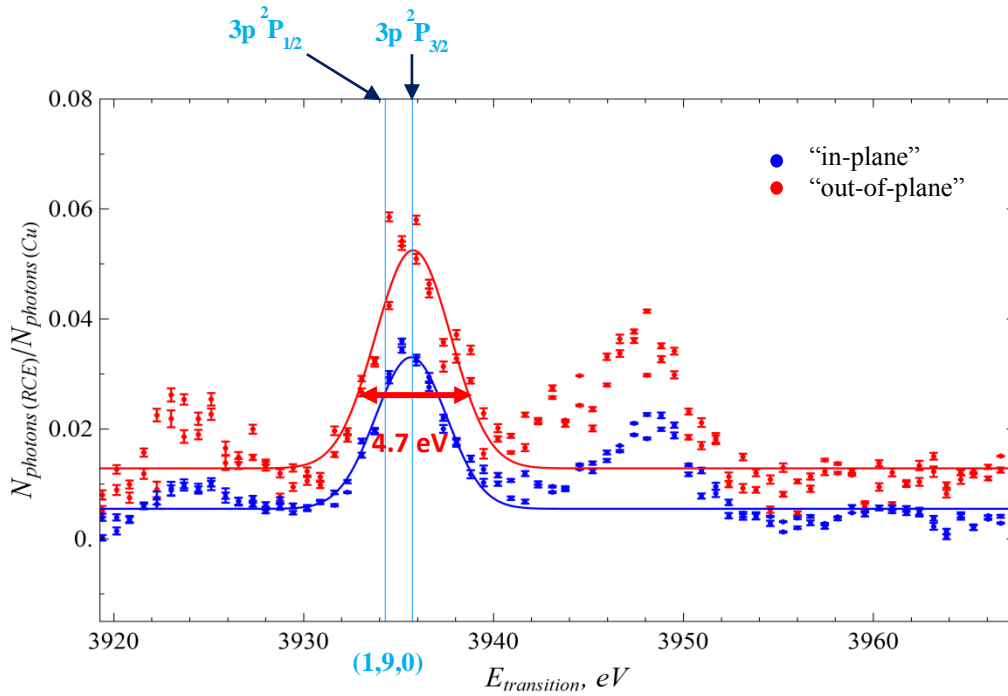
Figure 4.14 *X-ray K_β resonance curves for the 390 MeV/u Ar^{17+} ions excited in a Si crystal at $\varphi = 0.1°$*

Table 4.4 *Fit parameters of the peaks in the X-ray resonance curves in Ar^{17+} at 390 MeV/u*

Peak	Transition	(k,l,m)	Curve	FWHM, eV	Peak position, eV
Measured K_α (figure 4.12)	$2p \rightarrow 1s$	(1,1,0)	"out-of plane" "in-plane"	1.88±0.01 1.89±0.01	3322.98 (fixed)
K_α depth (figure 4.13)	$3s,3d \rightarrow 2p$	(0,8,0)	"out-of plane" "in-plane"	3.4±0.2 3.8±0.2	613.2±0.1 613.2±0.1
Measured K_β (figure 4.14)	$3p \rightarrow 1s$	(1,9,0)	"out-of plane" "in-plane"	4.7±0.3 4.4±0.2	3935.760±0.002 3935.66±0.001

Another scanning was performed by fixing angle φ at 0.16°. The resonance spectra obtained by the scanning of the θ angle within the range from 1.84° to 2° have shown similar results and listed in "Appendix" (figure A.1).

The performed experiment clearly demonstrated the DRCE occurrence of the relativistic H-like Ar ions as a two-step excitation process, sequentially from the ground state into the $n = 2$ and into the $n = 3$ states, by means of observing a sharp decrease of the initial charge-state fraction at the position satisfying the resonance condition for the second excitation step simultaneously with a reduction of the K_α X-ray emission. The decrease of the initial charge-state fraction related to the intermediate step of the sequential excitation was about 29% of the total depth in the resonance profile, whereas the highest population transfer

from the $n = 2$ into the $n = 3$ states of about 25% has been observed at the same crystal orientation.

Table 4.5 *Experimentally observed RCEs and DRCEs in H-like Ar at 390 MeV/u and $\varphi = 0.1°$*

Transition type			Resonance depth, %	Miller indices	$\theta,°$
RCE	$1s\,^2S_{1/2} \rightarrow$	$2p\,^2P_{3/2}$	4	(1,1,0)	1.93
RCE	$1s\,^2S_{1/2} \rightarrow$	$3p\,^2P_{1/2}$	1		1.70
		$3p\,^2P_{3/2}$	1		1.73
			1		1.76
DRCE	$1s\,^2S_{1/2} \rightarrow 2p\,^2P_{1/2} \rightarrow$	$3s\,^2S_{1/2}$	3	(1,1,0)	1.79
		$3d\,^2D_{3/2}$			1.82
		$3d\,^2D_{5/2}$			
RCE	$1s\,^2S_{1/2} \rightarrow$	$3p\,^2P_{1/2}$	1		1.84
		$3p\,^2P_{3/2}$	1		1.88
DRCE	$1s\,^2S_{1/2} \rightarrow 2p\,^2P_{3/2} \rightarrow$	$3s\,^2S_{1/2}$	7.5	(1,1,0)	1.91
		$3d\,^2D_{3/2}$	4		1.95
		$3d\,^2D_{5/2}$			

As it was mentioned above, the fine structure of the levels with $n > 2$ could not be separated in any of the experiments performed with H-like Ar ions. Therefore, for the next experiment the He-like Ar was chosen because of its simple dipolar X-ray emission.

4.3 Resonant Coherent Excitation in 381 MeV/u He-like Ar

The occurrence of the resonant coherent excitation was further investigated in He-like ions. For this an Ar^{16+} ion beam with energy of 381 MeV/u was used together with a 1μm thick Si-crystal. The measurements and the data analysis have been performed as in the case of H-like argon. The variation of the initial charge-state fraction and of the X-ray emission yield has been observed as a function of the crystal orientation relatively to the beam axis. The resonance conditions were calculated using the levels energies taken from the NIST database [4.1] listed in table 4.6.

Table 4.6 *Transition energies from the ground state in Ar^{16+} into n=2 and 3 states [4.1]*

Level	Energy, eV
1s2p $^1P_1$	3139.5823
1s3p $^1P_1$	3683.848
1s3s $^1S_0$	3679.461
1s3d $^1D_2$	3683.589

Figure 4.15 shows the resonance diagram for the transitions in Ar^{16+} and Ar^{17+} ions. He-like projectiles can be ionized in random collisions with the target atoms and then an RCE in H-like Ar may contribute into the charge-state and X-ray yields. Therefore, the resonance conditions in both, H-like and He-like, charge-states were taken into account. The solid lines in the figure denote the RCE conditions for the H-like and the dashed lines − for the He-like ions.
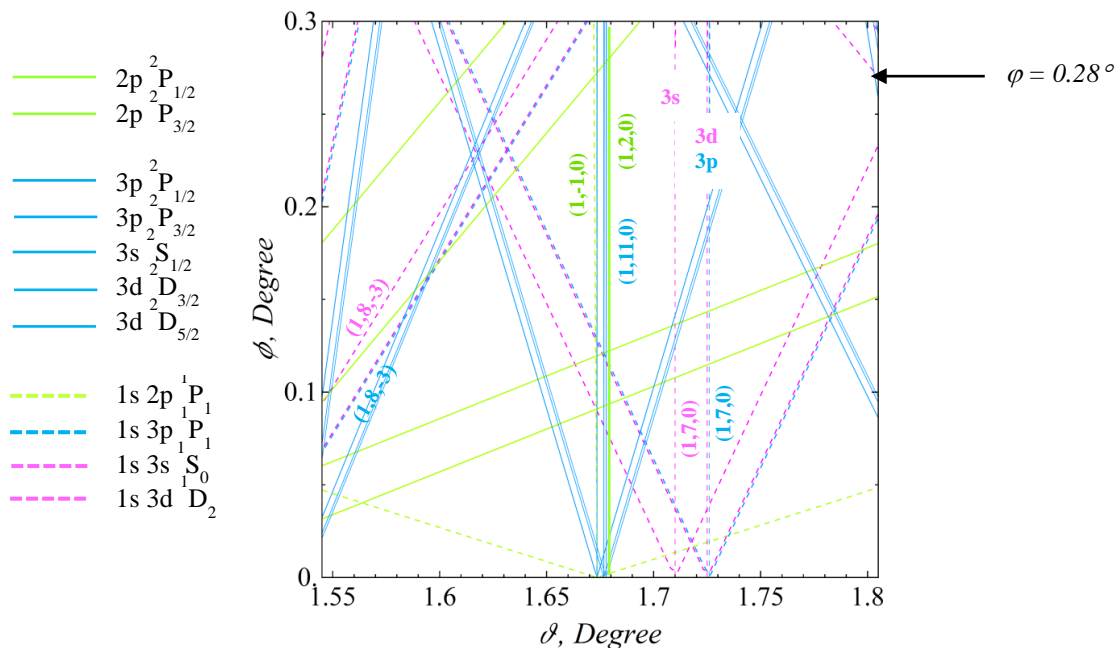

Figure 4.15 *RCE conditions for 381 MeV/u He-like and H-like Ar ions passing a Si-crystal.*

Within the chosen angular range the Ar^{16+} projectile ions can be excited into the 1s2p ^{1}P$_1$ (green dashed lines) and then into 1s3s ^{1}S$_0$ and 1s3d ^{1}D$_2$ states (magenta dashed lines). A direct excitation from the ground state into the 1s3p ^{1}P$_1$, 1s4p ^{1}P$_1$ and 1s5p ^{1}P$_1$ is also allowed. In the present study only a direct excitation into $n = 3$ state was considered because direct transitions into the higher states have lower probability, as it was demonstrated in the previous experiments. The resonance conditions for the directly excited 1s3p ^{1}P$_1$ level from the ground state are marked with blue dashed lines in figure 4.15. Figure 4.16 shows the mechanism of RCE and DRCE in He-like Ar. The probabilities of the collisional ionization from the ground and excited states calculated in section 1.2.4 and the decay rates of the excited states are given in the figure. The result of the calculation suggests that the DRCE in He-like Ar can be put in evidence via measurements of the variation in the charge-states yield and K$_\alpha$ X-ray emission which have comparable rates. The probability of the radiative decay from the $n = 3$ states is about two orders of magnitude lower.
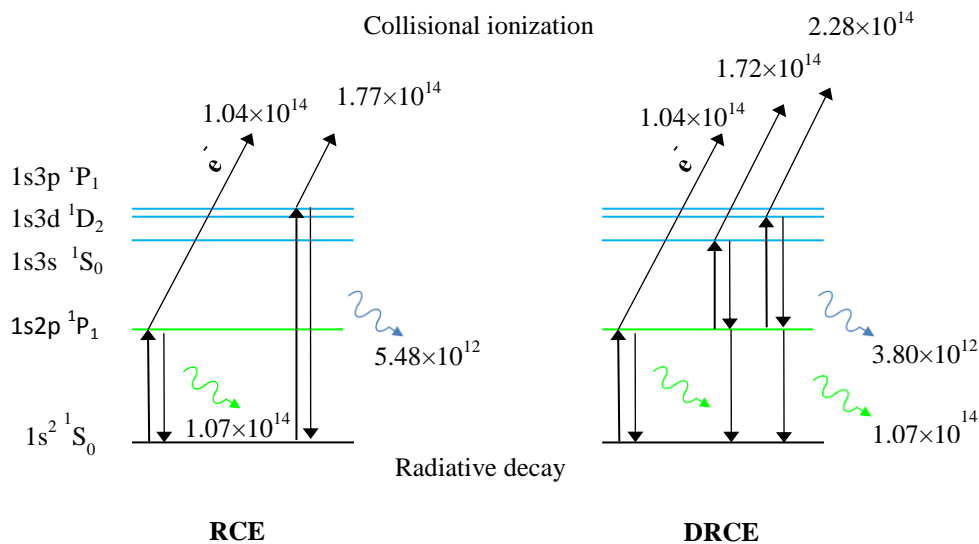
Figure 4.16 *Levels scheme of Ar^{16+}*.

The Ar^{17+} ions can be excited sequentially from the 1s^2 S$_{1/2}$ into 2p ^{2}P$_{1/2}$ and 2p ^{2}P$_{3/2}$ and further into the 3s ^{2}S$_{1/2}$, 3d ^{2}D$_{3/2}$ and 3d ^{2}D$_{5/2}$ states or directly from the ground state into the 3p ^{2}P$_{1/2}$ and 3p ^{2}P$_{3/2}$ states. In figure 4.15 the resonance conditions for the $n = 2$ transitions in H-like ions are denoted with solid green lines and for the $n = 3$ transitions − with solid blue lines.

The resonance curves obtained by the scanning of the θ angle within the range from 1.55° to 1.75° at $\varphi = 0.28°$ are presented in figure 4.17 (a), (b), (c) and (d).The charge-state resonance curve (a) represents the variation of the survival He-like ions fraction measured as a function of the rotation angle θ.
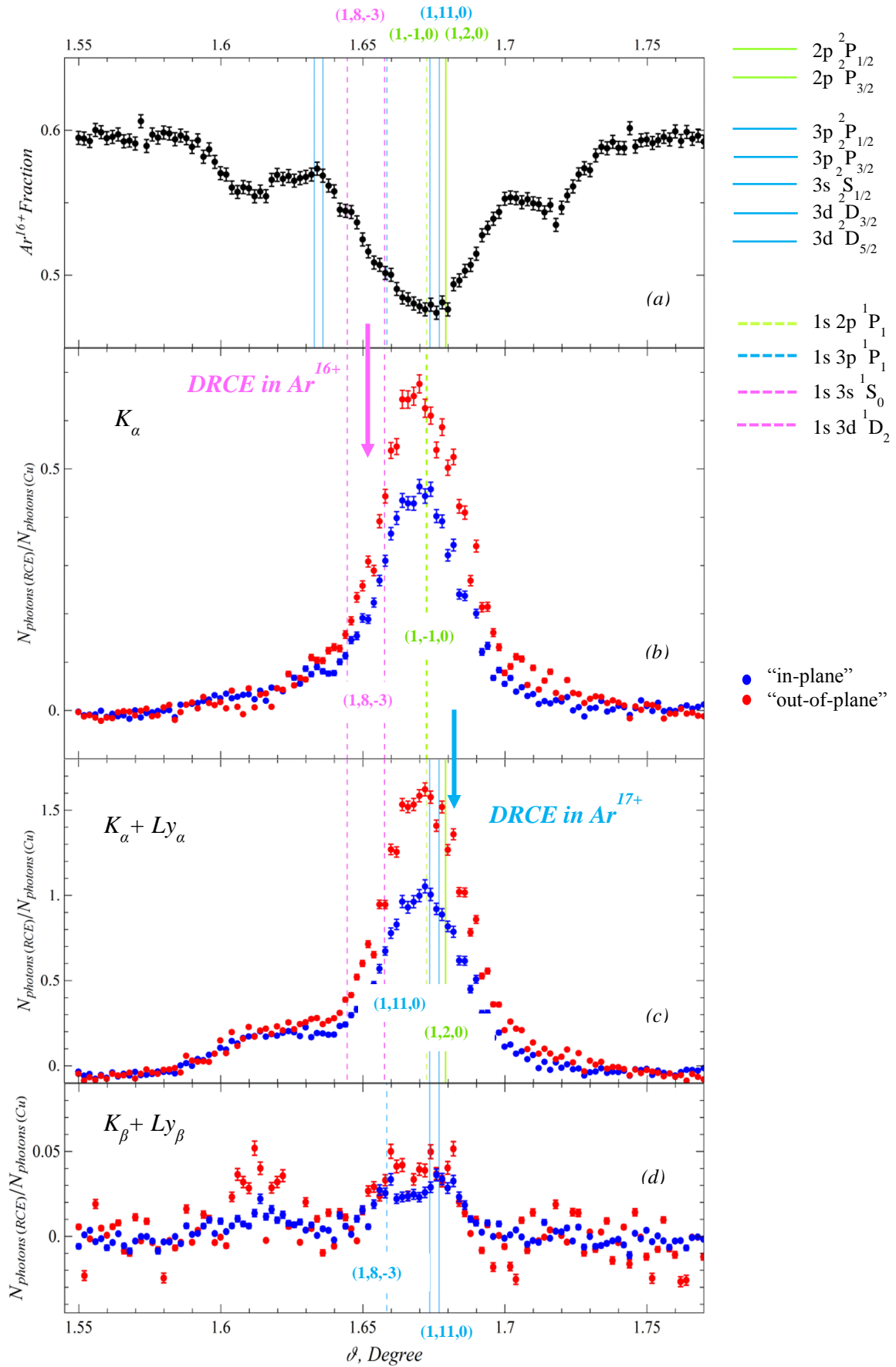
Figure 4.17 *Resonance curves for 381 MeV/u Ar^{16+} in a Si-crystal placed at $\varphi = 0.28°$: (a) charge-state variation; (b), (c) and (d) X-ray resonance curves.*

In this experiment three charge-states have been registered by the particle detector: He-like (initial charge-state), H-like (ionized ions) and bare (doubly ionized ions). The observed bare fraction is below 5% for all measurements and it is almost the same for different crystal orientations. Therefore only He-like survival fraction is considered in this analysis.

The highest remaining fraction of the He-like state in the present measurement is about 60%. This reduction of the initial charge-state is again caused by the ionization of the ions via random collisions with the target atoms (probability 1.01×10^{14} s^{-1}). At the resonance conditions the probability of the collisional ionization of the excited ions is increasing (2×10^{14} s^{-1}). Hence, an additional decrease of the initial charge-state fraction is expected and can be seen in figure 4.17 (a).

The expected estimated positions of the minima in the resonance curve are marked for the different transitions with the same colors as the ones, used in figure 4.15. The fraction of the initial charge-state is reduced from 60% to 48% at $\theta \approx 1.67°$ which satisfies RCE conditions for the $1s^2$ $^1S_1 \rightarrow 1s\, 2p$ $^1P_1$ transition in He-like Ar ions induced by the $(1,\bar{1},0)$. Smaller structures corresponding to the resonance conditions for other transitions satisfied within the range of the scanning are present in the resonance curve.

The X-ray yield has been measured by the "in" and "out-of-plane" detectors (red and blue points in the X-ray curves, respectively) within the same angular θ range as the charge-state distribution of the ions. The measured X-ray spectra contain K_α and K_β lines observed from the He-like Ar as well as Ly_α and Ly_β emitted by the decay of H-like ions (see chapter "Data analysis"). The close energy of the K_α and Ly_α lines (3139.58 eV and 3318.17 eV) cannot be separated by the X-ray detectors. Therefore, the second curve presented in figure 4.17 (c) was obtained by considering both contributions for each measurement point. This resonance curve was obtained by the integration over the range covering both lines in the measured spectra which means a sum of the transitions in H-like and He-like Ar ions. For the transition from the $n = 3$ states the statistics was too low to permit a clear K_β and Ly_β separation in the measured X-ray spectra (see figure 3.19). Therefore, the $K_\beta + Ly_\beta$ resonance curve was obtained by the integration of the measured X-ray spectra over a broad range.

The highest observed K_α emission corresponds to the resonance condition for the $1s^2 \rightarrow 1s\, 2p$ $^1P_1$ transition in He-like Ar ions induced by the $(1,\bar{1},0)$ crystal orientation and detected at $\theta \approx 1.675°$ (the angular position is marked with dashed green line). The DRCE into the $1s\, 3s$ $^1S_0$ and $1s\, 3d$ $^1D_2$ states is expected at around $1s\, 3d$ $^1D_2$ resonance condition

(magenta dashed lines). In the resonance spectrum 4.17 (b) a reduction of the K_α emission can be seen only as one measurement point (marked with a magenta arrow in the figure).

The K_α and Ly_α summation spectrum (see figure 4.15 (c)) shows a strong asymmetry of the main peak. This is can be explained by the high reduction of the Ly_α component of the sum at $\theta \approx 1.68°$ position corresponding to the DRCE condition for the $1s^2\ S_{1/2} \rightarrow 2p\ ^2P_{3/2}$ $\rightarrow 3s\ ^2S_{1/2}$, $3d\ ^2D_{3/2}$ and $3d\ ^2D_{5/2}$ states in H-like Ar.

The resonance spectrum (d) shows the sum of the K_β and Ly_β X-rays. The observed peaks at $\theta \approx 1.67°$ and $\theta \approx 1.66°$ correspond to the photons emitted from decay of the directly excited $1s3p\ ^1P_1$ state in Ar^{16+} and $3p\ ^2P_{1/2,\ 3/2}$ states in Ar^{17+} ions.

To conclude, one can say that the present resonance spectra do not fully prove the occurrence of the DRCE process in the He-like ions. A possible reason could be the occurrence of the many RCEs in the He-like and H-like ions which were satisfied at the close angular orientations and could not be separated. The scanning of the same θ range was repeated at different φ values (0.09°, 012°, 0.14°, 0.22° and 0.25°). The obtained resonance curves are summarized in "Appendix" (figures A.2-A.6). The measurements give the same results as the one discussed here.

The result could be improved by performing a coincident detection of the charge-states and X-rays yields. However, this kind of experiment would require either a longer measurement time or the use of a different type ion detector, with a higher count rate capability.

4.4 Anisotropy of the X-ray emission

In this section the anisotropy of the measured X-ray emission from the decay of the 2p excited states into the ground state of the H-like and He-like ions measured by the "in-plane" and "out-of-plane" detectors is discussed. Figure 4.18 shows the alignment of the X-ray detectors at the setup. A dependence of the population of the $2p_x$, $2p_y$ and $2p_z$ magnetic substates on the linear-polarized crystal field direction is investigated here.
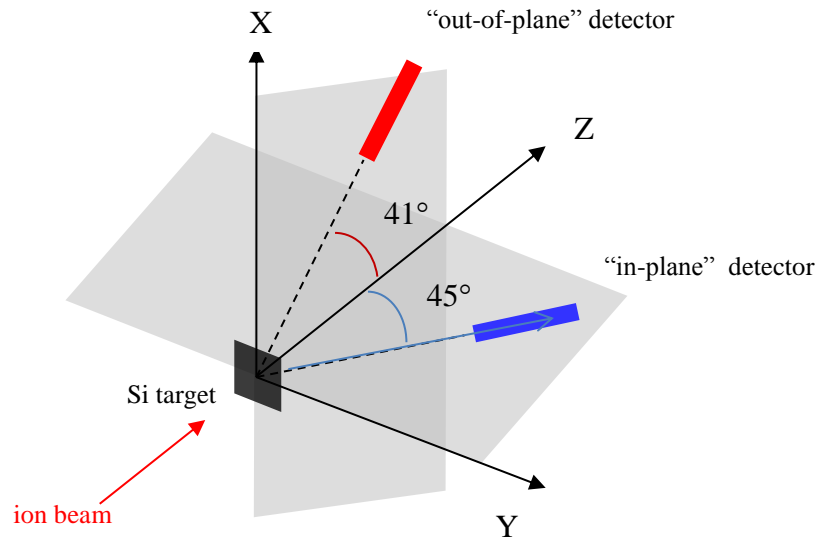
Figure 4.18 *Scheme of the X-ray detection system*

4.4.1 Anisotropy of the X-ray emission from the radiative decay of He-like ions

Figure 4.19 shows the K_α X-ray emission observed from the decay of the coherently excited He-like Ar ions in a Si crystal. The radiation was measured by the "in-plane" and "out-of-plane" detectors. The relative geometrical efficiency factor between the two detectors was estimated from the ratio of the K_α X-ray emission at non-resonance crystal orientation, considering its isotropy (see section 3.2.3). The resonance conditions for the $1s^2 \rightarrow 1s\,2p\;^1P_1$ transition satisfied at $\theta \approx 1.62°$ and $\theta \approx 1.67°$ (green dashed line in the figure) have been induced by the $(1,\bar{2},5)$ and $(1,\bar{1},0)$ harmonics of the crystal field, respectively. The transition energy is 3139.5823 eV [4.1].

The K_α emission at $\theta \approx 1.62°$ was observed only by the "in-plane" detector. This anisotropy indicates the selective excitation of the ions into the $1s\,2p_x$ magnetic substate. At $\theta \approx 1.67°$ the "out-of-plane" radiation is dominant which is a sign of the higher excitation probability into the $1s\,2p_y$ and $1s\,2p_z$ substates.
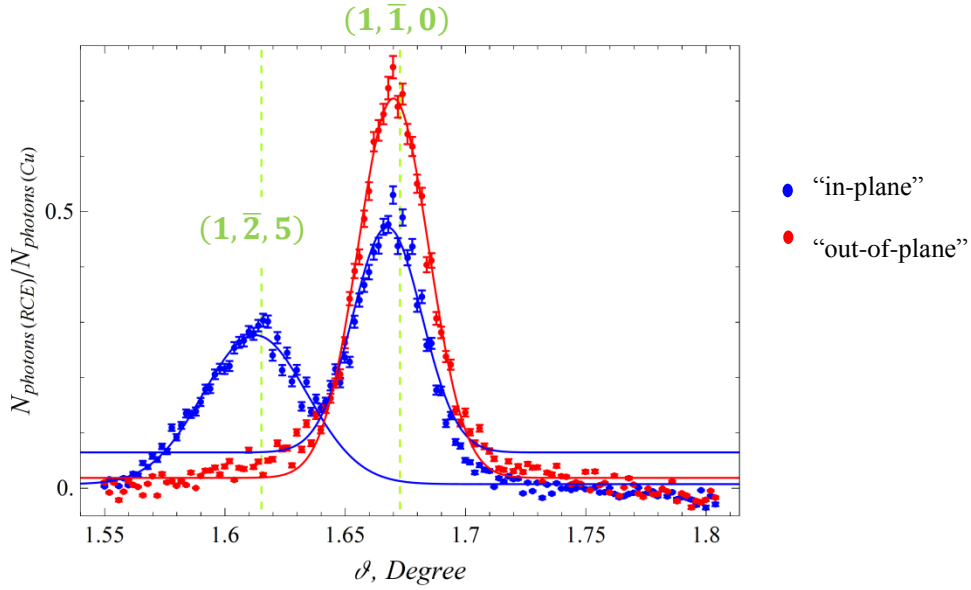
Figure 4.19 *X-ray resonance spectra from the decay of the Ar^{16+} ions coherently excited in a Si crystal measured as a function of θ rotation angle.*

The K$_\alpha$ peaks have been fitted with Gauss function for a quantitative comparison with the calculation. The fit functions were integrated over the ±3σ interval. The ratios obtained from the fit of the experimentally observed "out-of-plane" and "in-plane" radiation are compared with the values calculated using formula (1.33) in table 4.7.

Table 4.7 *Ratios of the "out-of-plane" and "in-plane" X-ray yields from the decay of the 1s 2p excited state in Ar^{16+}*

Transition	(k, l, m)	Experiment	Calculation
1s 2p ^{1}P$_1$→1s^2	$(1,\bar{2},5)$	≈ 0	0.098
	$(1,\bar{1},0)$	1.56±0.4	1.99

The observed radiation in the "out-of-plane" direction at $\theta \approx 1.62°$ was considered here as 0. This strong anisotropy is also supported by the calculated ratio of 0.098. The dependence of the X-ray anisotropy on the m Miller index was studied in [4.3]. Several measurements performed at different m values (from 0 to 5) showed that the anisotropy is increasing for higher m values.

For the radiation related to the $(1,\bar{1},0)$ harmonic a ratio of almost two was calculated, whereas the experimental data give the ratio of 1.56±0.4. A possible reason for this difference of about 22% could be the relaxation of the alignment due to the random collisions with target atoms in the crystal.

4.4.2 Anisotropy of the X-ray emission from the radiative decay of H-like ions

The radiation from the 2p $^2P_{1/2}$ state is defined by the dipole radiation pattern, i.e. it is isotropic in all directions [1.38] which was also observed in the present experiment. Figure 4.20 shows the X-ray K_α emission measured from the decay of the coherently excited 2p state in Ar^{17+}. The RCE condition for the 1s $^2S_{1/2} \rightarrow$ 2p $^2P_{1/2}$ transition induced by the (1,1,0) crystal orientation is satisfied at $\theta \approx 1.8°$ (green line in the figure). The transition energy is 3318.176 eV [4.1]. The experimental ratio R between the "out-of-plane" and "in-plane" radiation is close to unity.

Figure 4.20 *X-ray resonance spectra from the decay of the 2p $^2P_{1/2}$ state of Ar^{17+} ions coherently excited by the (1,1,0) harmonic of a Si crystal.*

The K_α X-ray emission from the decay of the 2p $^2P_{3/2}$ state of the H-like Ar ions measured as a function of rotation angle θ is presented in figure 4.21. The RCE for the 1s $^2S_{1/2} \rightarrow$ 2p $^2P_{3/2}$ transition is satisfied at $\theta \approx 1.93°$ (green lines in the figure). The highest K_α radiation is observed at this angular orientation. The energy of this transition is 3322.9919 eV [4.1]. The DRCE conditions into the $n = 3$ state are satisfied at $\theta \approx 1.91°$ and $\theta \approx 1.94°$ (blue lined in the figure). At this orientation a reduction of the K_α X-ray emission is observed because part of the ions were further excited into the higher state and deexcited via ionization instead of radiative decay.
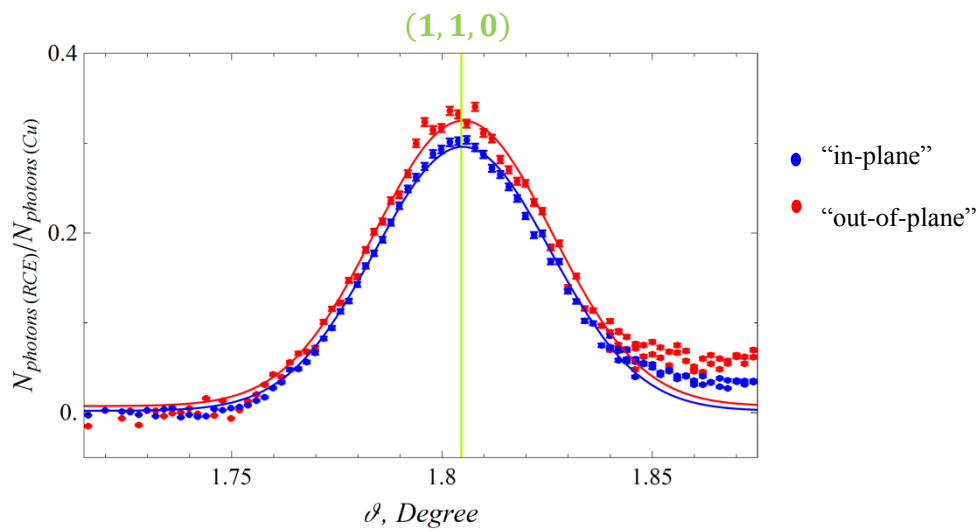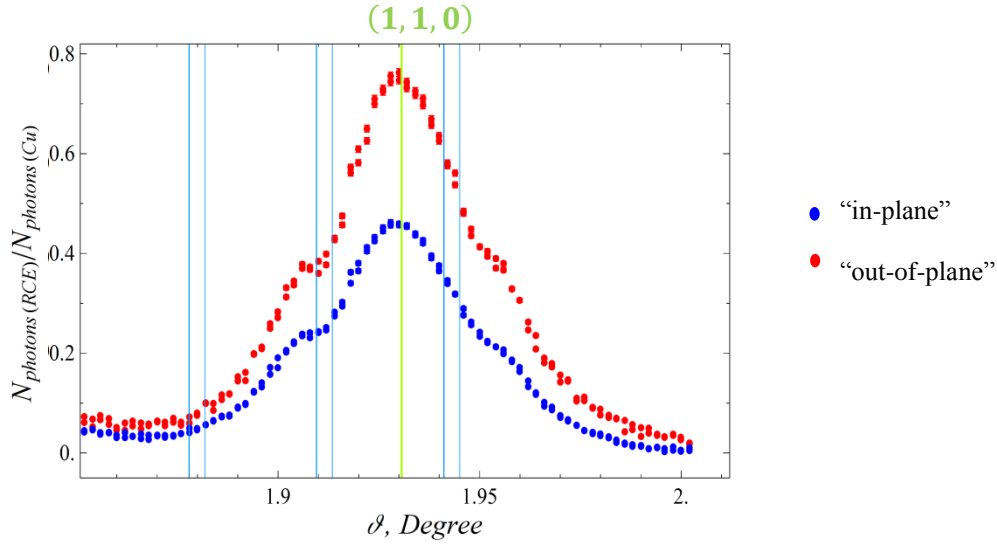
Figure 4.21 *X-ray resonance spectra from the decay of the 2p $^2P_{3/2}$ state of Ar^{17+} ions coherently excited by the (1,1,0) harmonic of a Si crystal.*

The ratio of the highest the X-ray emission measured by the "out-of-plane" and "in-plane" detectors was estimated as $R = 1.6\pm0.3$ which is equal to the calculated value using the formula (1.35). In this case the radiation is dominant in the "out-of-plane" direction which means that 1s 2p$_x$ substate was less populated.

The theoretically and experimentally obtained ratios of the radiation from the 2p $^2P_{1/2}$ and 2p $^2P_{3/2}$ excited states in H-like Ar are summarized in table 4.8.

Table 4.8 *Ratios of the "out-of-plane" and "in-plane" X-ray yields from the decay of the excited states in Ar^{17+}*

Transition	(k, l, m)	Experiment	Calculation
2p $^2P_{1/2}\rightarrow$ 1s $^2S_{1/2}$	(1,1,0)	1.1±0.3	1
2p $^2P_{3/2}\rightarrow$1s $^2S_{1/2}$	(1,1,0)	1.6±0.3	1.60

The results obtained from the experimental data are consistent with the calculated values. The alignment of the magnetic substates by the crystal field fully explains the observed anisotropy of the X-ray emission from the decay of the 2p $^2P_{3/2}$ excited state in H-like Ar ions.

Summary and outlook

In the present work the Double Resonant Coherent Excitation (DRCE) of the highly-charged relativistic ions from the ground state into the $n = 3$, 4 and 5 has been observed. For the first time the resonant excitations from the ground state into the higher states have been induced as a sequential two-step excitation via an intermediate state. The coherent excitation of the projectiles by the electric field of the crystal-target was demonstrated to be an efficient tool for the population control of the levels with energy around $3 - 4$ keV. The DRCE of the Ar ions was detected from the variations in the charge-state distribution of the projectiles and of the photon yield emitted from the decay of the excited states of the ions measured as a function of the target orientation relative to the beam direction. The resonance conditions for the specific transitions in the ions have been adjusted by changing the frequency of the crystal field defined by the k, l, and m Miller indices.

Several experiments have been performed at the HIMAC facility, Japan. The DRCEs into the $n = 3$, 4 and 5 states were observed in H-like Ar ions at 455 MeV/u mainly from the charge-states distribution of the ion yield. The initial charge-state fraction at the DRCE conditions was decreasing to about 0.72 comparing to about 0.76 fraction at RCE conditions into the $n = 2$ state and about 0.82 fraction at non-resonance conditions. The X-ray emission from the decay of the excited states has been measured only at the resonance conditions. The K_α X-ray emission from the decay of the excited state was observed at the RCE conditions into the $n = 2$ state and DRCE conditions into the $n = 3$, 4 and 5 states. The K_β emissions was observed in the X-ray spectra measured at RCE and DRCE conditions into the $n = 3$ sate with a comparable intensity. The origin of the K_β photons can be investigated by measuring a variation of the X-ray yield as a function of the crystal orientation, like it was done for the charge-states. The K_γ and K_δ X-rays related to the decay of the $n = 4$ and 5 states, respectively, could not be observed with the statistics of the present experiment. A possible reason is the lower excitation probability into the higher state combined with increased collisional ionization probability from these states.

The experiment on H-like Ar was repeated to investigate a variation of the X-ray emission from the decay of the excited states as a function of the rotation angle within the same angular range as the charge-state distribution. Different ion beam energy, 390 MeV/u, was chosen in order to induce the second excitation step by the crystal harmonics with higher l Miller index (for narrowing the resonance profile). The decrease of the initial charge-state fraction related to the second step of the sequential excitation of about 29% of the total

resonance depth has been observed. Simultaneously, a population transfer from the $n = 2$ into the $n = 3$ states of about 25% was registered from the reduction of the K_α X-ray emission. These observations confirm the occurrence of the DRCE in H-like Ar. In order to evaluate the contributions of the RCE and DRCE phenomena into the measured K_β X-ray emission, the rotation angle has been transformed into the transition energy. The calculation was performed using the resonance equation together with the value of the beam energy and the Miller indices chosen for an excitation of specific transitions. The analysis confirmed that the photon emission related to the radiative decay of the directly excited 3p $^2P_{1/2}$ and 3p $^2P_{3/2}$ states and produced due to the collisional mixing of the sequentially excited the 3S $^2S_{1/2}$, 3d $^2D_{3/2}$ and 3d $^2D_{5/2}$ states contribute into the measured K_β X-ray emission. This means that, as in the previous experiment, the direct RCE into the 3p states is always satisfied at the DRCE conditions into the 3s and 3d states. In both experiments with H-like Ar the fine structure of the ion could not be resolved.

Another experiment was performed with 381 MeV/u He-like Ar because of its simple dipole radiation. Both, the charge-state and X-ray resonance variation, were obtained as a function of the rotation angle within various ranges. The experiment showed the resonance behavior of the ions excitation process. But with the statistics of the measured X-ray emission the DCRE could not be clearly discerned from single RCEs. A possible reason could be the high production of the H-like Ar ions (about 40%) by the ionization of the initial ions in collisions with target atoms. In the present experiment a clear separation between the K_α and Ly_α X-ray emission, i.e. distinction between the RCEs in He-like and in H-like ions, was not possible due to the limited energy resolution of the X-ray detectors. The result can be improved by performing a coincident detection of the charge-states and X-rays yields. For this a particle detector with a much higher count rate capability is required (> 1MHz).

In the present work also the anisotropy of the K_α X-ray emission measured with two detectors installed in different planes ("out-of-plane" and "in-plane" relatively to the beam direction) was investigated. The anisotropy of the X-ray emission observed from the radiative decay of the excited states indicates a selective population of the magnetic substates of the excited levels of the ions which is controlled by the polarization direction of the crystal oscillating field. The experimentally observed ratios of the "out-of-lane" and "in-plane" X-ray emission are in a good agreement with theoretical calculations. This kind of investigations will be continued by measurements of the X-ray emission over a broad angular range using a new detection system which was designed and constructed.

Zusammenfassung

In der vorliegenden Arbeit wurde eine Methode untersucht, um kontrolliert und effizient die Bevölkerung angeregter n = 2, 3, 4 und 5 Zustände in schweren Wenigelektronenionen mit Hilfe elektrischer Felder in Kristallen zu manipulieren.

Bei der Durchquerung eines Kristalls spüren relativistische, hochgeladene Ionen ein mit einer Frequenz ν_{field} oszillierendes, vom Kristall erzeugtes Coulombfeld. Wenn die Frequenz dieses Feldes mit der Frequenz ν_{ij} eines im Ion dipolerlaubten Übergangs vom Anfangszustand i in den Endzustand j übereinstimmt, wird die resonante Anregung des Iones möglich. Dieser Prozess ist als resonante kohärente Anregung (*Resonant Coherent Excitation, RCE*) bekannt.

Die Frequenz des Kristallfeldes ν_{field} ist in dem Schwerpunktsystem des Projektils durch die Ionengeschwindigkeit $\boldsymbol{v}$ und den Abstand d zwischen den Atomen im Kristall gegeben:

$$\nu_{field} = \frac{\gamma \boldsymbol{v}}{d}. \tag{Z.1}$$

wobei d üblicherweise in Bereich von einigen 10^{-10} m liegt.

Für relativistische Ionen mit Energien im Bereich von hunderten von MeV/u ist die Frequenz des elektrischen Feldes in Kristall sehr hoch: $\nu_{field} \cong 10^{18}\ s^{-1}$. Dadurch können Übergänge im Bereich von einige keV im Ion angeregt werden.

$$E_{ij} = \hbar \nu_{ij} = \hbar \nu_{field} = \frac{\hbar \gamma \boldsymbol{v}}{d} \tag{Z.2}$$

Mit einer Anpassung der Ionenenergie könnte die Frequenz des Feldes geändert werden um bestimmte Übergänge im Ion anzuregen. Das gleiche Ergebnis kann auch viel präziser durch die kontinuierliche Änderung der Ausrichtung des Kristalls relativ zur Richtung der Eintrittsgeschwindigkeit des Ions bei konstant bleibender Ionenenergie erzielt werden. Dadurch kann der RCE Prozess als effiziente Methode für die Spektroskopie einer Vielzahl angeregter Zustände in hochgeladenen Ionen über einen breiten Energiebereich eingesetzt werden. Diese Spektroskopietechnik erschließt einen Energiebereich der in der Laserspektroskopie nicht zugänglich ist.

In der vorliegenden Arbeit wird die resonante Anregung des Projektils durch die Anpassung der Kristallorientierung erzielt. Für den Anregungsprozess kann man zwei Regime unterscheiden: unter channeling Bedingungen und ohne diese Orientierung.

Wenn die Orientierung die *channeling* Bedingungen erfüllt, d.h. das Ion bewegt sich entlang einer Kristallachse (*axial*) oder in einer Kristallebene (*planar*), dann erfahren die Ionen den Einfluß einer wohl definierten Feldfrequenz. Dies führt zum sogenannten 2D-RCE. Durch die Bewegung des Projektils entlang der Kanäle, werden die Stöße des Projektils mit den in dem Kristall gebundenen Atomen stark unterdrückt. Diese Stöße würden die Resonanz der Anregung stark stören. Besonders stark tritt dieser Effekt im Falle von leichten Ionen mit niedriger Kernladungszahl auf.

Wenn die Ionen sich nicht entlang einer Kristallebene oder Achse bewegen, kann trotzdem RCE stattfinden. Wegen der Kristallsymmetrie können die Ionen dann unterschiedliche Frequenzen simultan erfahren (3D-RCE). Die resonante Anregung außerhalb der *channeling* Bedingungen eröffnet neue experimentelle Möglichkeiten im Vergleich zur 2D-RCE. Erstens, ermöglicht sie die Kontrolle über die Polarisation der angeregten Zustände im Ion mit Hilfe des Kristallfeldes. Zweitens, erlaubt sie eine doppelte Anregung des Ions durch gleichzeitige Einwirkung zweier verschiedener Feldfrequenzen des Kristalls, erzeugt von verschiedenen Symmetrien im Kristall selbst. Somit werden auch die durch die Erhaltungsregel des Drehimpulses im Atom verbotenen direkten Übergänge via sequentieller doppelter RCE (DRCE) möglich.

Der Schwerpunkt dieser Arbeit ist die Untersuchung der DRCE in höhere Zustände (n = 3, 4 und 5) in hochgeladenen mittelschweren Ionen. Zur Untersuchung wurden wasserstoffähnliches Argon (Ar^{17+}) und heliumähnliches Argon (Ar^{16+}) gewählt.

Während der Wechselwirkung der Argon Ionen mit dem Kristall werden Projektil Elektronen aus dem 1s Grundzustand ($1s\ ^2S_{1/2}$) in die höheren energetischen Zustände mit n = 2, 3 4 oder 5 resonant angeregt. Je höher der Wert von n ist, desto niedriger wird die Anregungswahrscheinlichkeit für den Zustand. Das angeregte Ion wird durch die Aussendung eines Photons (radiativ) oder eines Elektrons (Auger-Zerfall) relaxieren. Das Elektron im angeregten Zustand könnte auch durch Stöße des Ions mit den Kristallatomen ionisiert werden. Die Ionisationswahrscheinlichkeit für einen angeregten Zustand ist höher als für den Grundzustand. Diese zwei Prozesse, die Emission eines Photons bzw. die Ionisation des angeregten Projektils wurden in dieser Arbeit für den Nachweis der RCE/DRCE Prozesse verwendet.

Die Präsenz einer resonanten kohärenten Anregung in den Ionen zeigt sich prinzipiell durch eine steile Abnahme des Einfangsladungszustandes der Ionen bei einer bestimmten Targetorientierung. Der Grund hierfür ist die Zunahme der Ionsationswahrscheinlichkeit des Elektrons in angeregten Zuständen. Dazu kommt noch eine simultane Zunahme der K_α

Strahlung bei gleicher Kristallorientierung. Falls die Bedingungen für einen doppelten RCE (DRCE) erfüllt sind, ändert sich die Signatur des Prozesses. Der Eingangsladungszustand nimmt noch stärker ab und deutet somit auf eine noch höhere Ionizationswahrscheinlichkeit hin. Gleichzeitig wird die K_α Emission reduziert. Diese beiden Beobachtungen weisen darauf hin, dass der $n = 2$ Zustand weniger bevölkert wird, dafür aber Zustande mit höherem n stärker.

Für die experimentelle Untersuchung des DRCE Prozesses müssen die Resonanzbedingungen (Z.2) zwischen der Ionengeschwindigkeit und der Orientierung des Kristalls erfüllt werden. Für die nicht *channeling* Orientierung des Kristalls ist die Resonanzbedingung gegeben durch:

$$E_{ij} = \frac{\hbar \gamma \boldsymbol{v}_{ion}}{d} = \hbar \gamma v_{ion} \left(k \cos\theta \cos\varphi \frac{\sqrt{2}}{a} + l \sin\theta \frac{1}{a} + m \cos\theta \sin\varphi \frac{\sqrt{2}}{a} \right). \qquad (Z.3)$$

wobei v_{ion} die Geschwindigkeit des Ions entspricht. Die Orientierung des Kristalls ist durch die Winkel θ, φ und ω relativ zu der Kristallachse [110] definiert und k, l und m sind die Miller-Indices des Kristalls.

Für die Anregung eines bestimmten Zustandes des Ions wird für die Orientierung des Target-Kristalls die Relation zwischen den Winkeln θ und φ aus der Gleichung (Z.3) berechnet, in dem die Ionengeschwindigkeit v_{ion} und die Energie des Übergangs ΔE_{ij} festgelegt werden. Wenn für eine Kristallorientierung (gegebenes θ, φ und ω) gleichzeitig die Resonanzbedingungen für zwei verschiedene Übergänge erfüllt sind, wird die doppelte resonante Anregung des Ions (*double resonant coherent excitation, DRCE*) möglich.

Der absolute Wert der Ionengeschwindigkeit wird durch die Energie des Ionenstrahls mit Hilfe des Beschleunigers festgelegt. Die Präzision des Energiewertes ist limitiert durch die Impulsverteilung des Ionenstrahls, welche eine Eigenschaft des Beschleunigers ist, und zweitens durch den Energieverlust und die Energieverbreiterung der Ionen im Target. Um die Targeteffekte zu minimieren, ist die Benutzung eines dünnen Targets von Vorteil. Allerdings wird dadurch die Wahrscheinlichkeit für die RCE reduziert. Letztendlich muß ein Kompromiss zwischen der Targetdicke, der Strahlintensität und der Strahlqualität (Impulsverbreitung und Divergenz) gefunden werden. Die feine Energieanpassung an die Resonanzbedingung erfolgt durch die Drehung des Targets relativ zur Flugrichtung der Ionen in sehr feinen Schritten.

Die nachfolgend beschriebenen Experimente wurden an dem medizinischen Synchrotron-Beschleuniger HIMAC in Chiba, Japan durchgeführt. Die Anlage liefert, hauptsächlich für medizinische Zwecke, Strahlen von leichten bis mittelschweren hoch geladenen Ionen bei Energien von 100 bis 800 MeV/u mit einer Energieunschärfe $\Delta E / E \cong$ 2.4×10^{-4} und Intensitäten von 10^9 pps. Für die RCE Experimente wurden Strahlen von Ar^{16+} und Ar^{17+} bei ungefähr 455 MeV/u und 380 MeV/u gut kollimiert und mit sehr niedriger Divergenz ($<10^{-4}$) vorbereitet. Als Target wurde ein 1µm dicker Siliziumkristall verwendet. Das Target wurde auf einem Hochpräzisionsgoniometer in einer Vakuumkammer eingebaut. Das Goniometer kann in 5 Richtungen bewegt werden: zwei Translationen entlang der X und Y Achsen senkrecht zur Strahlrichtung und drei Rotationen um die Achsen X, Y und Z. Die Startposition des Kristalls wurde so gewählt, dass die (220) Kristallebene parallel zum Kammerboden orientiert war.

Der Zerfall der angeregten Zustände in den Argonionen wurde mit zwei Siliziumdetektoren nachgewiesen. Ein Detektor wurde in der horizontalen Ebene unter 45° und der andere in der vertikalen Ebene, unter 41° in der Goniometerkammer, im Vakuum installiert.

Nach der Wechselwirkung mit dem Target wird der Ionenstrahl weiter in Richtung eines ortsauflösenden Silizium-Teilchendetektors transportiert. Zwischen der Targetkammer und dem Teilchendetektor wurde einen Dipolmagnet installiert, um die verschiedenen Ladungszustände der Ionen zu trennen, so dass die Ausbeute der einzelnen Ladungszustände in dem Teilchendetektor nachgewiesen werden konnte.

Obwohl in dem Fall von hochgeladenen Argonionen die Ionzationswahrscheinlichkeit der angeregten Zustände und die Relaxation durch Röntgenemission gleich hoch sind (9.12×10^{13} s^{-1} bzw. 6×10^{13} s^{-1} für die 2p ^{2}P$_{1/2}$ und 2p ^{2}P$_{3/2}$ Zustände) konnte die Messung der Röntgenstrahlung und der Ladungsverteilung nach Durchqueren des Kristalls nicht gleichzeitig durchgeführt werden. Der Grund dafür ist der große Unterschied in den Raumwinkeln zwischen den Röntgendetektoren und dem Teilchendetektor verbunden mit dessen limitierter Zählrate (~5 kHz). Diese experimentelle Einschränkung und die Instabilität der Strahlintensität während des Experiments verlangen eine zusätzliche Messung für die Normierung der Ergebnisse. Diese Normierung wurde nur für die Photonenmessungen mit Hilfe eines dritten Siliziumdriftdetektors gemacht, der am Ende des Strahlrohrs hinter einer Kupferfolie plaziert wurde. Für die Normierung der Intensität des Ionenstrahls während den Röntgenmessungen wurde die Ausbeute der Cu-K$_\alpha$ and -K$_\beta$ Linien benutzt. Die Normierung

der Ionen im Teilchendetektor war nicht notwendig, weil dessen Nachweiseffizienz bei den niedrigen Zählraten 100% beträgt.

Der Nachweis des RCE und/oder des DRCE Prozesses in wasserstoff- und heliumähnlichen Argonionen erfolgt indirekt durch Änderungen in der Verteilung der Ladungszustände bzw. in der Ausbeute der Röntgenemission aus den angeregten Zuständen des Projektils nach der Wechselwirkung mit dem Kristall, in Abhängigkeit von der Kristallorientierung relativ zur Strahlrichtung (Winkel θ und φ). Zum Nachweis des RCE Prozesses ist keine genaue Energiemessung notwendig. Es ist ausreichend, die Ausbeute der Photonen zu messen, die bei der Relaxation des angeregten Zustands emittiert werden.

Die RCE und DRCE Messungen in Ar^{17+} Ionen wurden in zwei Experimenten bei zwei verschiedenen Strahlenergien durchgeführt. Die DRCE in $n = 3$, 4 und 5 Zustände wurde bei 450 MeV/u Strahlenergie untersucht. Der Nachweis des Prozesses basiert auf der Abnahme der Ionen im Anfangsladungszustand und auf der Röntgenausbeute nach Durqueren des Kristalls in Abhängigkeit von dessen Orientierung. Bei der Targetorientierung, welche die Bedingungen für die resonante Anregung erfühlt, ist die Überlebenswahrscheinlichkeit der A^{17+} Ionen 76% im Falle einer *single RCE* aus dem Grundzustand in den $2p$ $^2P_{3/2}$ Zustand. Für das gleiche Ion ist die Überlebenswahrscheinlichkeit nur 72% bei einer Targetorientierung, welche die DRCE Bedingungen für den Übergang in die $n = 3$ Schale erfüllt. Im Gegensatz hierzu beträgt die Wahrscheinlichkeit bei einer Targetorientierung außerhalb der Resonanzbedingungen 82%. Die geringere Überlebenswahrscheinlich des Ladungszustands 17+ im Falle von RCE/DRCE erklärt sich mit der höheren Ionisationswahrscheinlichkeit eines Elektrons aus einem angeregten Zustands (niedrigere Bindungsenergie) im Vergleich mit dem Grundzustand.

Die Relaxation des angeregten Zustands findet auch über die Emission eines Photons statt. In diesem Experiment wurde die Röntgenemission nur für jene ausgewählte Targetorientierungen gemessen, bei denen die Resonanzbedingung erfüllt ist. Für RCE in den $2p$ $^2P_{3/2}$ Zustand in Ar^{17+} ist dies die K_α Ausbeute. An der Targetposition, welche die DRCE Bedingungen erfüllt, wurde eine Abnahme der K_α Ausbeute beobachtet. Dies erklärt sich durch eine Reduzierung in der Bevölkerung des $2p$ Zustands aufgrund des DRCE Prozesses, der die angeregten Elektronen von $2p$ weiter in die $n = 3$ Schale befördert ($1s$ $^2S_{1/2} \rightarrow 2p$ $^2P_{3/2}$ $\rightarrow 3s$ $^2S_{1/2}$, $3d$ $^2D_{3/2}$ und $3d$ $^2D_{5/2}$). Sie ist somit ein starkes Argument für die Präsenz eines DRCE Prozesses. Die Anregung in den $n = 3$ Zustand kann aber auch auf dem direkten Weg von $1s$ $^2S_{1/2}$ nach $3p$ $^2P_{3/2}$ und $3p$ $^2P_{1/2}$ mittels eines einfachen RCE Prozesses erfolgen. Dies führt zur Emission der K_β Linie, welche sowohl unter den Bedingungen für den einfachen

RCE als auch für den DRCE beobachtet wurde, da bei Letzterem aufgrund der geringen Energiedifferenz zwischen dem 3p und dem 3d Niveau (ca. 1 eV) die Bedingungen für direkte und sequentielle Anregung gleichzeitig erfüllt sind. Als Folge dessen, beinhaltet die Resonanz in K_β zwei Emissionskomponenten. Eine entsteht aus der direkten Anregung des 3p Zustandes aus dem Grundzustand 1s $^2S_{1/2}$ und die zweite ist das Ergebnis der im Stoß erzeugten Mischung der durch DRCE sequentiell angeregten 3S $^2S_{1/2}$, 3p $^2D_{3/2}$ und 3p $^2S_{5/2}$ Zustände mit dem 3p Zustand.

Für wasserstoffähnliche Argonionen wurde auch die doppelte resonante Anregung (DRCE) in höhere Zustände für $n = 4$ und 5 untersucht. Das Vorhandensein des Prozesses (1s $^2S_{1/2} \rightarrow$ 2p $^2P_{3/2} \rightarrow$ 4s $^2S_{1/2}$, 4d $^2D_{3/2}$ und 4d $^2D_{5/2}$ oder 1s $^2S_{1/2} \rightarrow$ 2p $^2P_{1/2} \rightarrow$ 5s $^2S_{1/2}$, 5d $^2D_{3/2}$ und 5d $^2D_{5/2}$) wurde auch in diesem Fall durch Messungen der Röntgenemission der angeregten Zustände beobachtet. Wie oben beschrieben, wurde ebenfalls eine Abnahme der K_α Komponente beim Übergang von der einfache RCE Bedingung zur und DRCE Bedingung nachgewiesen. Allerdings konnte die erwartete simultane Zunahme der K_γ und K_δ Komponente aus der $n = 4$ und 5 Schale nach dem Übergang (4s, 4d→1s bzw. 5s, 5d→1s) auf Grund der geringen Statistik nicht gemessen werden. Ein möglicher Grund hierfür ist die niedrige Anregungswahrscheinlichkeit in die Zustände mit höherem n in Kombination mit einer erhöhten Wahrscheinlichkeit zur Stoßionisation aus diesen Schalen.

Das Experiment mit wasserstoffähnlichem Argon wurde auch bei einer niedrigeren Ionenenergie von 390 MeV/u wiederholt. Bei dieser Energie finden sich die Resonanzbedingungen bei höheren Werten des Millerindex l. Dies führt zu einer schmäleren Resonanzbedingung. Die DRCE in die $n = 3$ Schale wurde wieder durch die Abhängigkeit des Ladungszustandes sowie der Röntgenemission von der Orientierung des Kristalls nachgewiesen. In diesem Fall wurden die Röntgenmessungen über den gleichen Winkelbereich wie die Messungen des Ladungszustandes durchgeführt. Die Änderung der K_α Ausbeute als Funktion der Kristallposition ergibt eine klare experimentelle Signatur des DRCE Prozesses als ein sequentieller Anregungsprozess.

In einem weiteren Schritt wurde nach DRCE in He-ähnlichem Argon bei einer Energie von 381 MeV/u gesucht. Sowohl die Abhängigkeit des Eingangsladungszustandes als auch der Röntgenemission als Funktion der Kristallorientierung wurde über einen weiten Winkelbereich gemessen. In der Variation des Ladungszustandes konnten verschiedene Resonanzen identifiziert werden. Die Röntgenemissionsausbeute hingegen zeigt keine klare Trennung zwischen DRCE und dem einfachen RCE. Eine mögliche Erklärung dafür könnte sein, dass die Bedingungen für beiden einzelnen Anregungsschritte im DRCE zu weit

auseinander liegen. Hinzu kommt ein Untergrund aus der Produktion von wasserstoffähnlichen Argonionen durch Stoßíonisation im Kristall. Unter den gegebenen Experimentbedingungen war keine klare Trennung der K_α und Ly_α Komponenten, d.h. keine Trennung zwischen den RCEs in wasserstoff- und heliumähnlichen Ionen, möglich. Eine bessere Übereinstimmung der Resonanzbedinungen könnte bei anderen Ionenenergien erzielt werden und würde damit für zukünftige Messungen die Wahrscheinlichkeit der Beobachtung des DRCE in heliumähnlichen Argonionen erhöhen. Eine zweite Möglichkeit wäre eine koinzidente Messung zwischen Ladungszustand und Röntgenquant um die Produktion des wasserstoffähnlichen Argons durch Stoßionisation auszuschließen. Dafür ist aber eine erheblich längere Meßzeit oder ein neuer ortauflösender Teilchendetektor mit höherer Ratenverträglichkeit nötig. Dies war im Rahmen dieser Arbeit nicht möglich.

Desweiteren wurde in der vorliegenden Arbeit die Anisotropie der K_α Emission mittels der beiden Röntgendetektoren in der horizontalen und der vertikalen Ebene untersucht. Die Anisotropie wird durch die selektive Population der unterschiedlichen magnetischen Unterzustände des angeregten Ions erzeugt. Ursache hierfür sind verschiedene Polarisationsebenen des oszillierenden Feldes im Kristall. Je nachdem, welche Harmonischen des Feldes im Kristall gewählt wurden (gekennzeichnet durch die Miller- Indices k, l und m), wurde für die heliumähnlichen Argonionen ein Anisotropiefaktor von Null (starke Polarisation in der horizontale Richtung) bis 1.56 ± 0.4 zwischen den vertikalen und horizontalen Emissionrichtungen bestimmt. Dieser liegt ca 24% unter den theoretischen Vorhersagen, was ein deutlicher Hinweis auf die Zerstörung des Alignments durch Stöße mit den Kristallatomen ist. Weitere Messungen für unterschiedliche m - Werte (von 0 bis 5) bestätigen die in dieser Arbeit gemachte Beobachtung, dass höhere m - Werten zu höherer Anisotropie führen, was auf eine sehr selektive Bevölkerung der angeregten Zuständen hindeutet. Diese Ergebnisse sind in guter Übereinstimmung mit den theoretischen Vorhersagen.

Bei wasserstoffähnlichen Ionen wurde, wie erwartet, eine isotrope Emission für den Übergang von 2p $^2P_{1/2}$ nach 1s $^2S_{1/2}$ Zustand beobachtet. Ein entsprechender Faktor von 1.1 ± 0.3 wurde gemessen. Für den Übergang von 2p $^2P_{3/2}$ nach 1s $^2S_{1/2}$ wurde eine bevorzugte Emission in der vertikalen Richtung gemessen (Anisotropiefaktror von 1.6 ± 0.3). Beide Messungen wurden für dieselben k, l, m Werten durchgeführt.
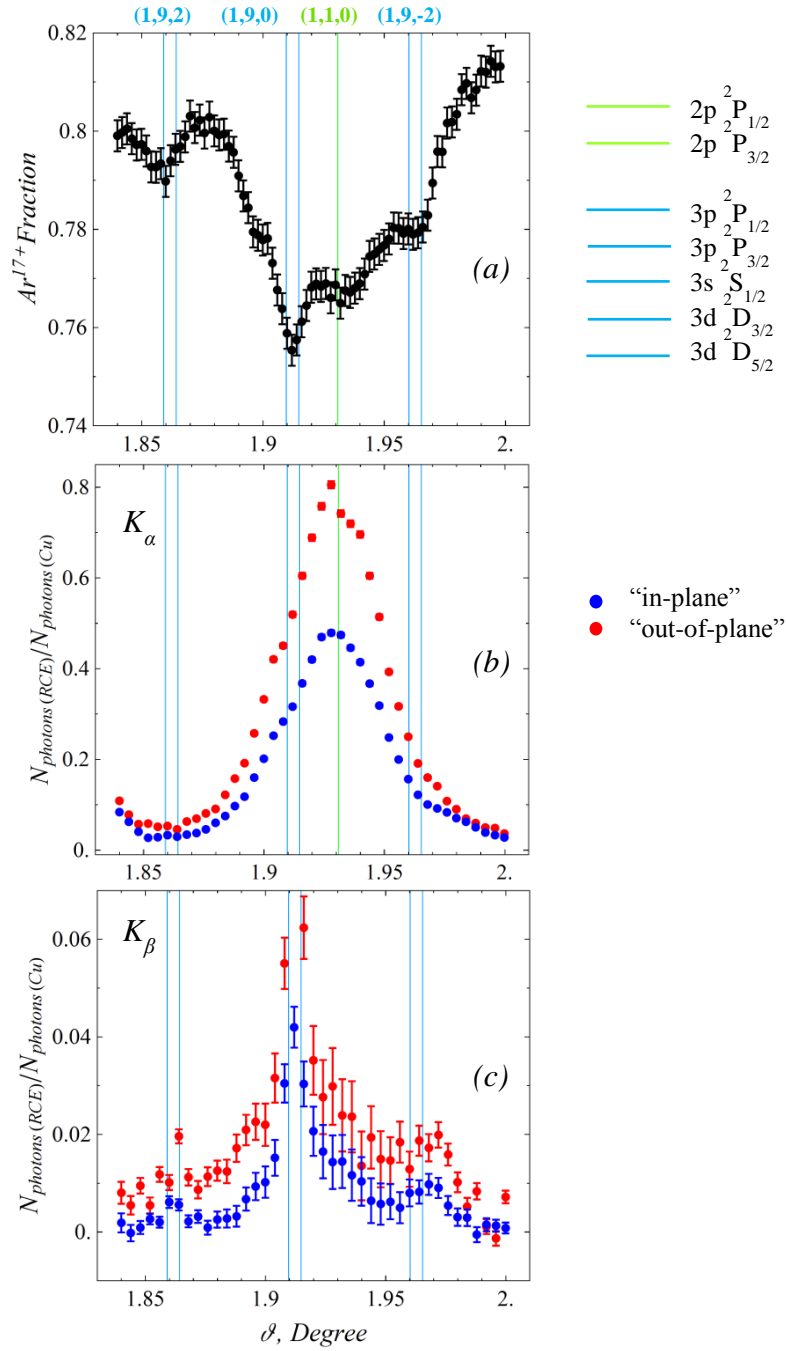
Appendix

Figure A.1 *Resonance curves for 390 MeV/u Ar^{17+} ions excited in a Si crystal at φ = 0.16°: (a) - initial charge-state fraction measured as a function of the θ rotation angle; (b) K$_\alpha$ X-ray emission and (c) K$_\beta$ X-ray emission measured from the decay of the excited states.*

Figure A.2 *Resonance curves for 381 MeV/u Ar^{16+} in a Si-crystal placed at $\varphi = 0.09°$: (a) charge-state variation; (b), (c) and (d) X-ray resonance curves.*

Figure A.3 *Resonance curves for 381 MeV/u Ar^{16+} in a Si-crystal placed at $\varphi = 0.12°$: (a) charge-state variation; (b), (c) and (d) X-ray resonance curves.*

117

Figure A.4 *Resonance curves for 381 MeV/u Ar^{16+} in a Si-crystal placed at $\varphi = 0.14°$:*
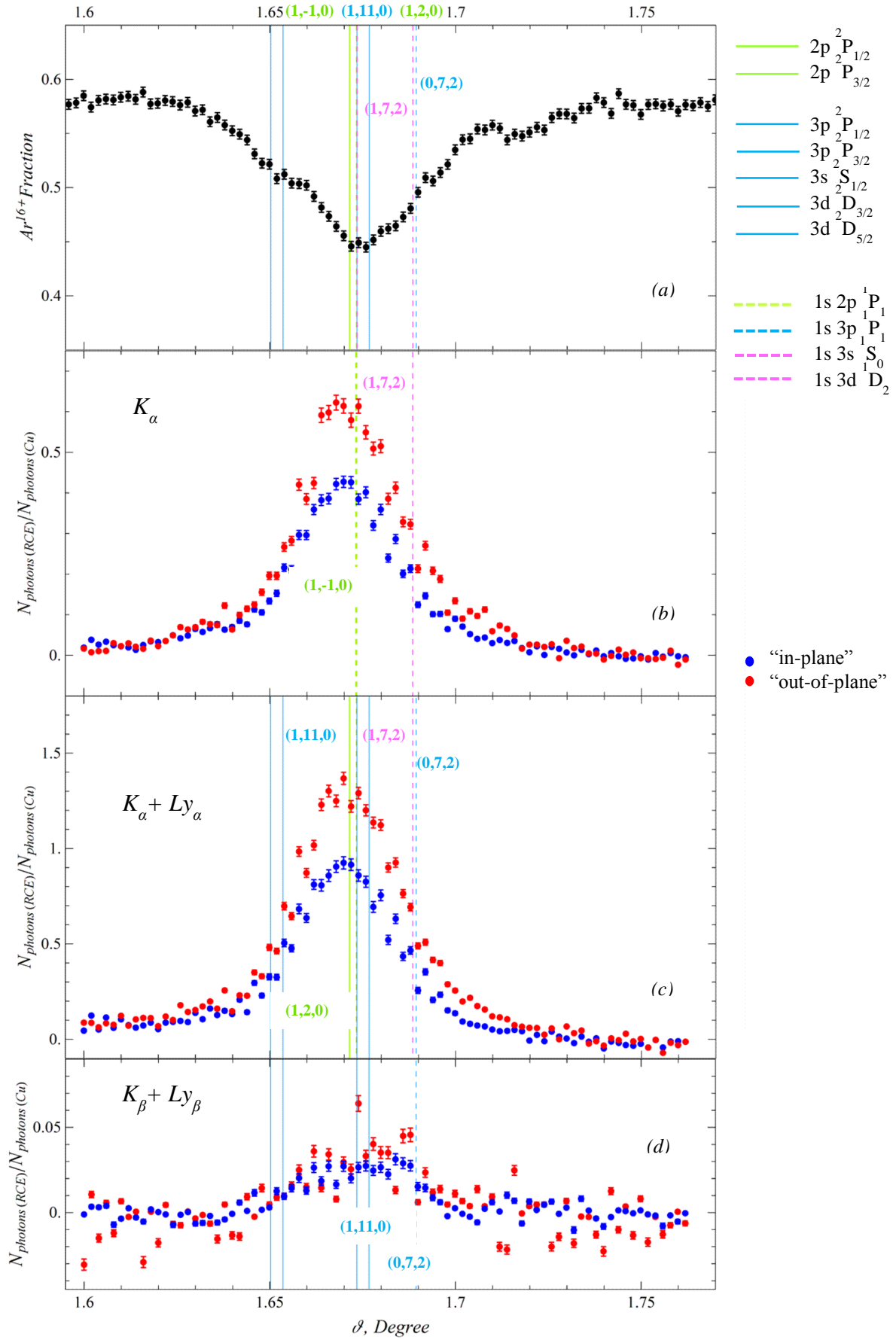*(a) charge-state variation; (b), (c) and (d) X-ray resonance curves.*

Figure A.5 *Resonance curves for 381 MeV/u Ar^{16+} in a Si-crystal placed at $\varphi = 0.22°$: (a) charge-state variation; (b), (c) and (d) X-ray resonance curves.*

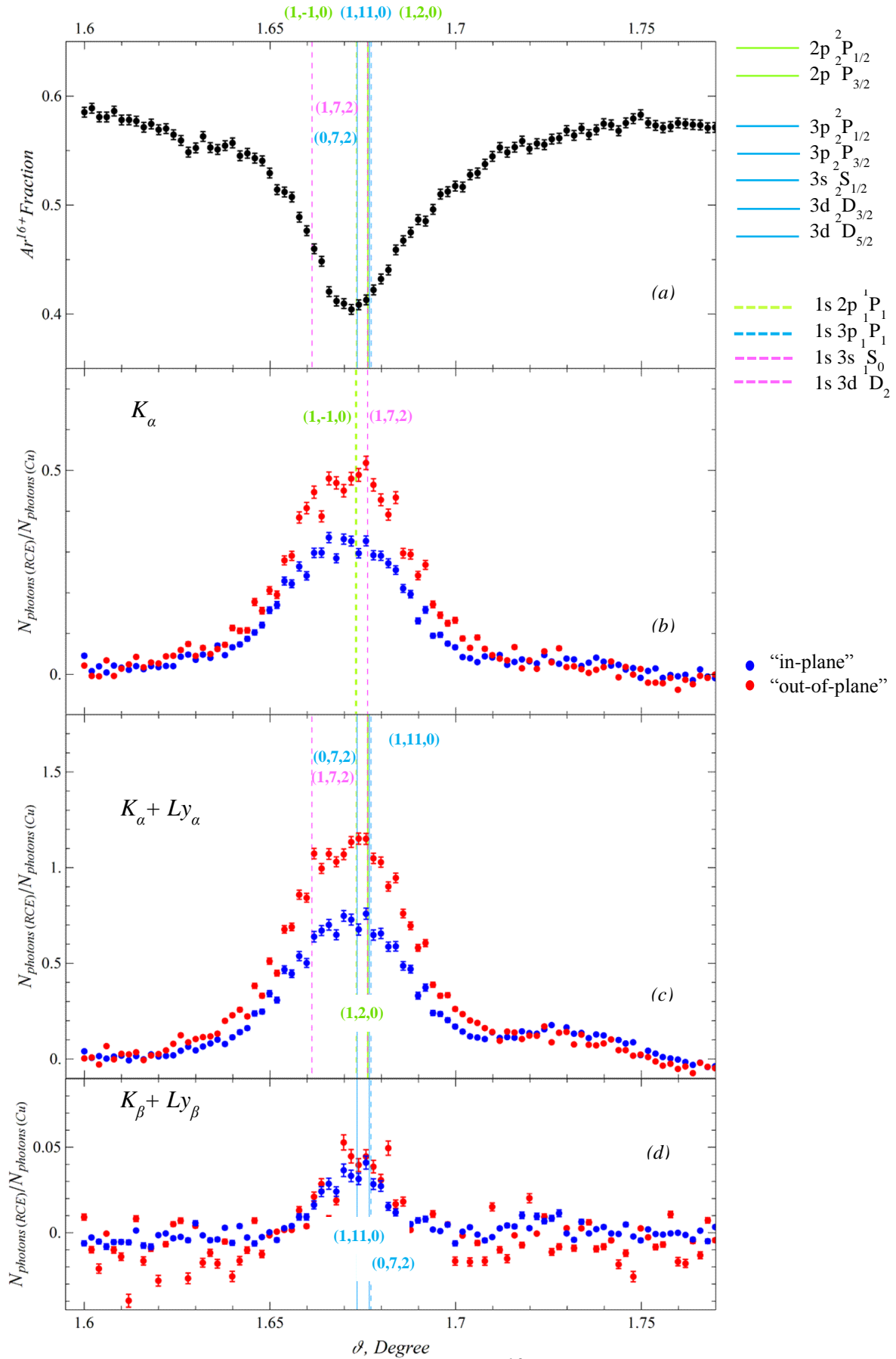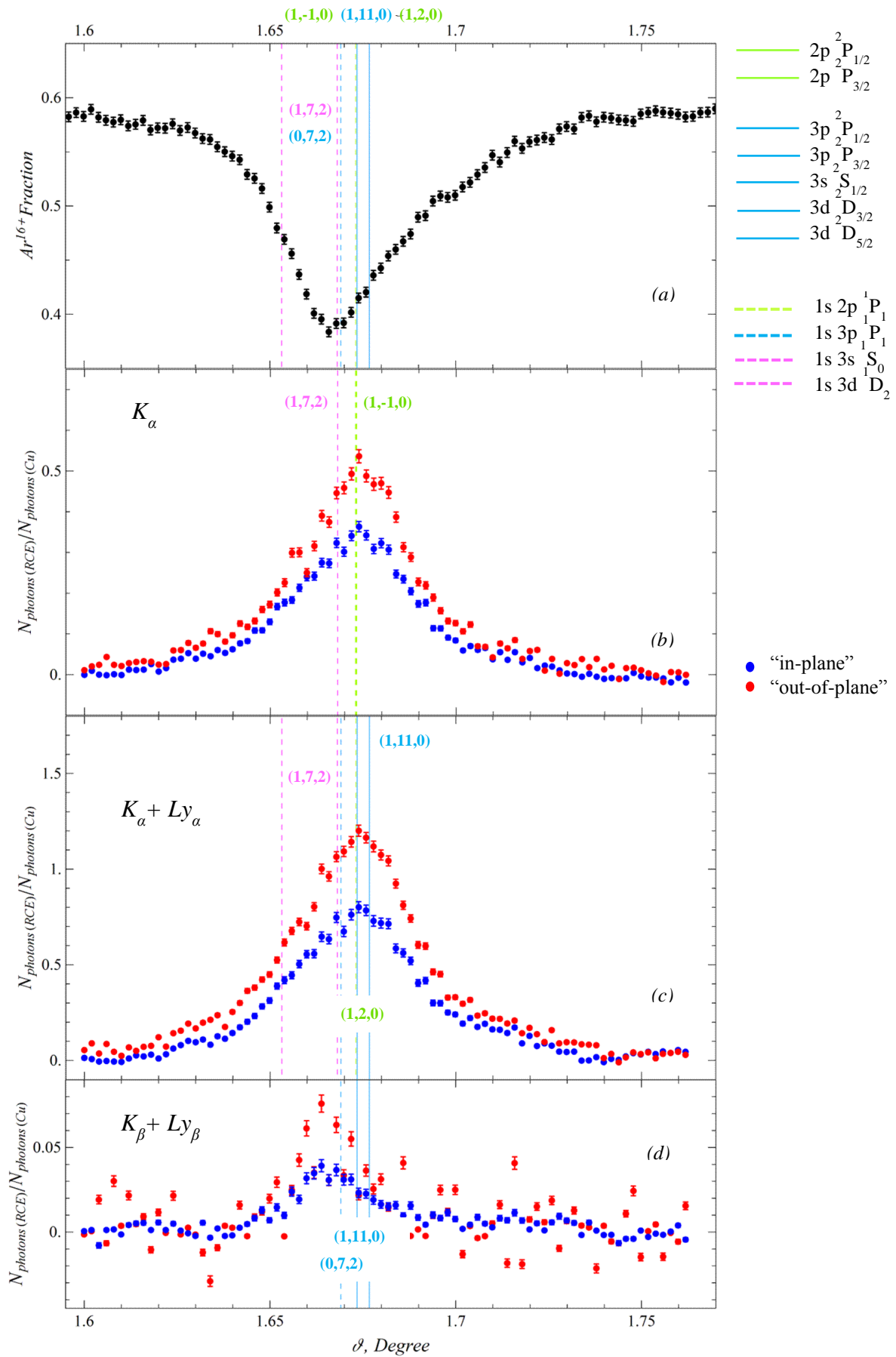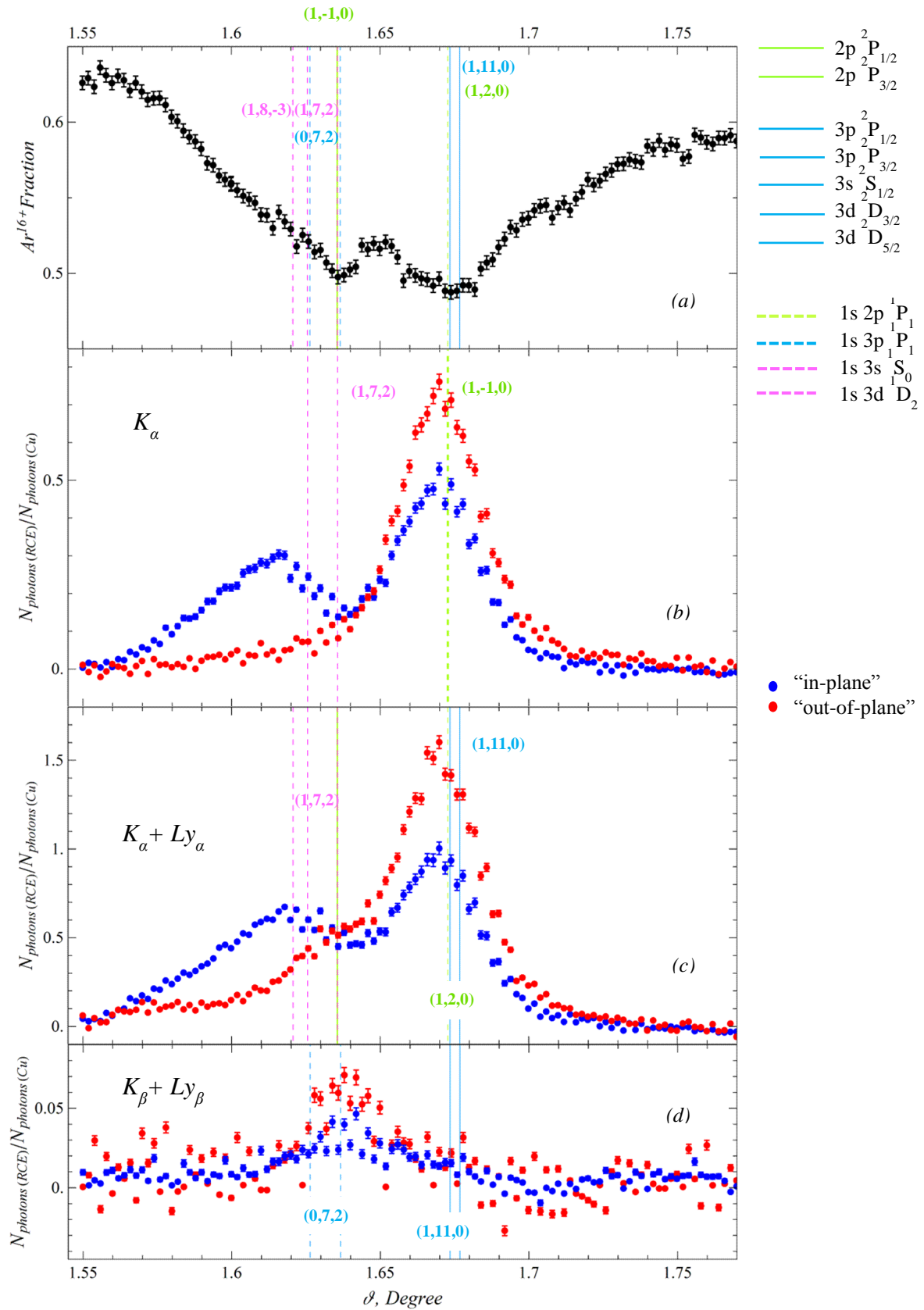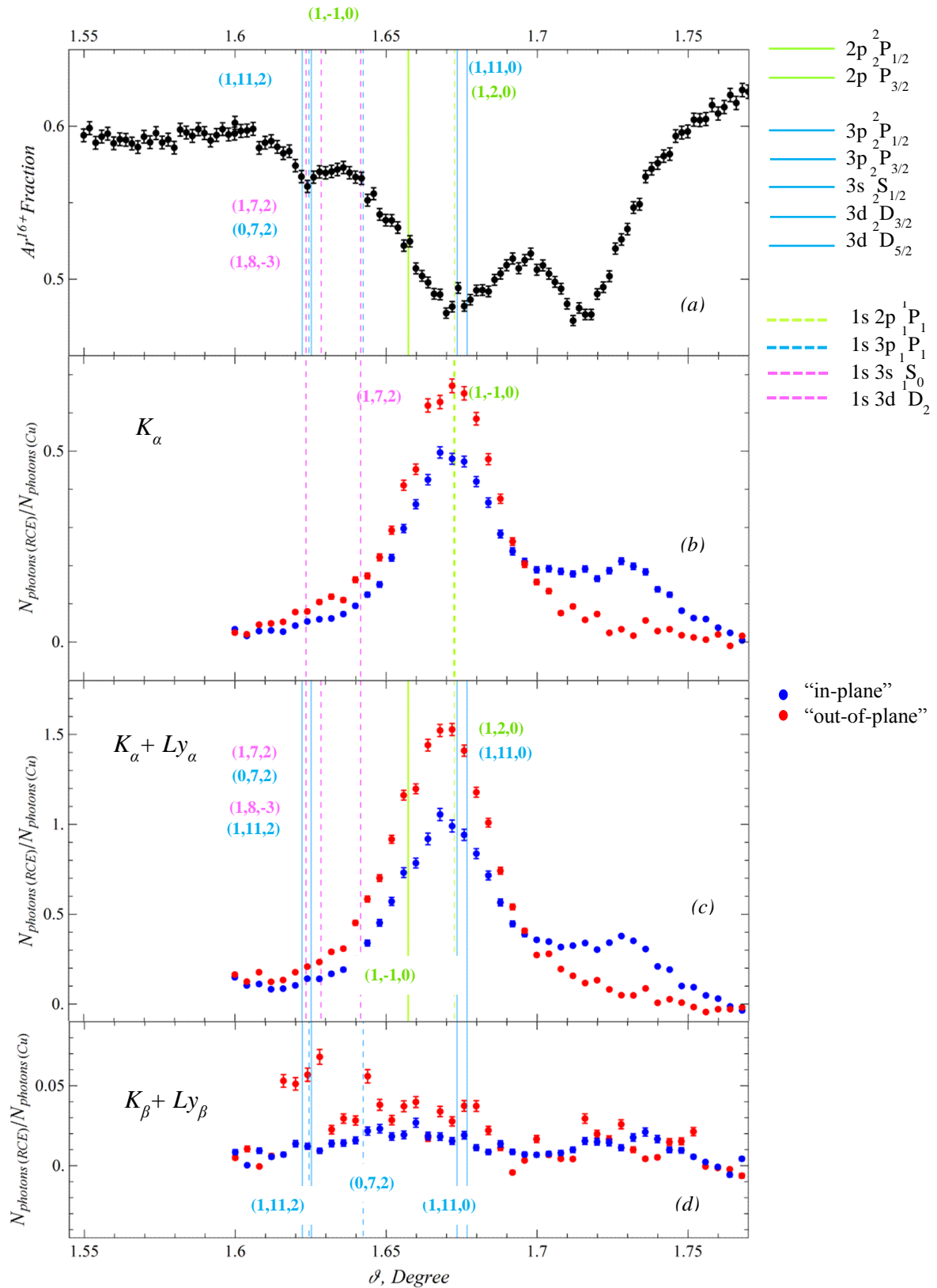Figure A.6 *Resonance curves for 381 MeV/u Ar^{16+} in a Si-crystal placed at φ = 0.22°: charge-state variation; (b), (c) and (d) X-ray resonance curves.*

References

Introduction

[0.1] M. Domke, K. Schulz, G. Remmers, G. Kaindl, and D.Wintgen. High-resolution study of $^1P^o$ double-excitation states in helium. *Physical Review A* **53**, p.1424 (1996).

[0.2] K. Schulz, G. Kaindl, M. Domke, J. D. Bozek, P. A. Heimann, A. S. Schlachter, and J. M. Rost. Observation of New Rydberg Series and Resonances in Doubly Excited Helium at Ultrahigh Resolution. *Physical Review Letters* **77**, p.3086 (1996).

 [0.3] P. Camus, T. F. Gallagher, J. M. Lecomte, P. Pillet, L. Pruvost, and J. Boulmer. Observation of an electronic correlation for double-Rydberg states of barium. *Physical Review Letters* **62**, p.2365 (1989).

[0.4] S. Reinhardt, G. Saathoff, Th. W. Hänsch, C. N., G Huber, S. Karpuk, W. Nörtershäuser, D. Bing, D. Schwalm, A Wolf, B. Botermann, C. Geppert, T. Kühl, T. Stöhlker, H. Yoneda, K. Nakagawa, F. Shimizu. Laser Spectroscopy on Relativistic Ion Beams. *Proceedings of the XIX International Conference Laser Spectroscopy, World Scientific*, p. 298 (2010).

[0.5] HIMAC homepage: http://www.nirs.go.jp/ENG/rd/1ban/himac_inf.html.

[0.6] GSI homepage: https://www.gsi.de/start/aktuelles.htm.

[0.7] T. Kuhl, A.Dax, M. Gerlach, D. Marx, H. Winter, M. Tomaselli, T. Engel, M. Wurtz, V.M. Shabaev, P. Seelig, R. Grieser, G. Huber, P. Merz, B. Fricke, C. Holbrow. New access to the magnetic moment distribution in the nucleus by laser spectroscopy of highly charged ions. *Nuclear Physics A* **626**, p.235c-240c (1997).

[0.8] V. V. Okorokov. Employment of coherent excitation of relativistic nuclei in a crystal in basic research on SRT and GRT. *Physics-Uspekhi* **46**, p.433-438 (2003).

[0.9] S. Datz, C. D. Moak, O. H. Crawford, H. F. Krause, P. F. Dittner, J. Gomez del Campo, J. A. Biggerstaff, P. D. Miller, P. Hvelplund, and H. Knudsen. Resonant Coherent Excitation of Channeled Ions. *Physical Review Letters* **40**, p.843 (1978).

[0.10] P. D. Miller, H. F. Krause, J. A. Biggerstaff, O. H. Crawford, S. Datz, P. F. Dittner, Del Campo, J. Gomez, C. D. Moak, N. Neskovic, P. Pepmiller, L. Brown. Resonant coherent

excitation of O^{7+}, F^{8+}, and C^{5+} in the <100> axial channel in gold. *Nuclear Instruments and Methods in Physics Research B* **13**, p.566 (1986).

[0.11] S. Datz, P.F. Dittner, H.F. Krause, C.R. Vane, O.H. Crawford, J.S. Forster, G.S. Ball, W.G. Davies, J.S. Geiger. Resonant coherent excitation of N^{6+} and Mg^{11+} in planar channeling: anisotropies in ionization probabilities and X-ray emission. *Nuclear Instruments and Methods in Physics Research B* **100**, p.272-278 (1995) .

[0.12] K. Komaki, T. Azuma, T. Ito, Y. Takabayashi, Y. Yamazaki, M. Sano, M. Torikoshi, A. Kitagawa, E. Takada, T. Murakami. Resonant coherent excitation of 390 MeV/u Ar ions planar channeled in Si crystals. *Nuclear Instruments and Methods in Physics Research B*, **146**, p.19-28 (1998).

[0.13] Yoichi Nakai , T. Ikeda, Y. Kanai , T. Kambara, N. Fukunishi, T. Azuma, K. Komaki, Y. Takabayashi, Y. Yamazaki. Resonant coherent excitation of 94 MeV/u Ar^{17+} ions channeling through a Si crystal *Nuclear Instruments and Methods in Physics Research B* **205**, p.784–788 (2003).

[0.14] Yoichi Nakai , T. Ikeda, Y. Kanai, T. Kambara, N. Fukunishi, K. Komaki, C. Kondo, T. Azuma, Y. Yamazaki, Resonant coherent excitation of 2s electron of Li-like Fe ions to the $n = 3$ states. *Nuclear Instruments and Methods in Physics Research B* **230**, p.90–95 (2005).

[0.15] Y. Nakano, S. Suda, A. Hatakeyama, Y. Nakai, K. Komaki, E. Takada, T. Murakami, and T. Azuma. Selective production of the doubly excited $2p^2$ (^1D) state in He-like Ar^{16+} ions by resonant coherent excitation. *Physical Review A* **85**, p.020701(R) (2012).

[0.16] C. Kondo, S. Masugi, T. Muranaka, A. Ishikawa, Y. Nakano, T. Azuma, A. Hatakeyama, K. Komaki, Y. Nakai, Y. Yamazaki, E. Takada, T. Murakami. Trajectory dependent resonant coherent excitation of planar-channeled ions in a thin Si crystal. *Nuclear Instruments and Methods in Physics Research B* **256**, p.157–161 (2007).

[0.17] A. Bräuning-Demian, A. Ananyevna, T. Azuma, H. Bräuning, D. Dauvergne, Y. Kanai, Y. Nakano, T. Shindo, S. Suda, Y. Yamazaki. Resonant coherent excitation of 191.1 MeV/u U89+ ions planar-channeled in a silicon crystal. *Journal of Physics Conference Series 10/2012* **388**(8), p.1.

[0.18] C. Kondo, S. Masugi, Y. Nakano, A. Hatakeyama, T. Azuma, K. Komaki, Y. Yamazaki, T. Murakami, and E. Takada. Three-Dimensional Resonant Coherent Excitation of Nonchanneling Ions in a Crystal. *Physical Review Letters* **97**, p.135503 (2006).
122

1 Ion – atom collisions

[1.1] R.K. Janev, L.P. Presnyakov, V.P.Shevelko. Physics of Highly-Charged Ions. *Springer-Verlag Berlin, Heidelberg* (1985).

[1.2] V.P.Shevelko, H. Tawara. Atomic Processes in Basic and Applied Physics. *Springer Series on Atomic, Optical, and Plasma Physics* Volume **68**, (2012).

[1.3] H. Bethe. Theory of the Passage of Fast Corpuscular Rays Through Matter. *Annalen der Physik* **f 5**, p.325 (1930).

[1.4] M. Inokuti. Inelastic Collisions of Fast Charged Particles with Atoms and Molecules — The Bethe Theory Revisited. *Reviews of Modern Physics* **43**, p.297 (1971).

[1.5] R.K. Janev. Approximate charge and transition energy cross-section scaling for excitation of atoms colliding with multicharged ions. *Physical Review A*, **53**, p.219, (1996).

[1.6] C.O. Reinhold, R.E. Olson, W. Fritsch. Excitation of atomic hydrogen by fully stripped ions. *Physical Review A*, **41**, p.4837, (1990).

[1.7] J.T. Park, J.E. Aldag, J.M. George, J.L. Peacher. Cross sections for excitation of atomic hydrogen to the $n = 2$, 3, and 4 states by 15-200-keV protons. *Physical Review A* **14**, p.608 (1976).

[1.8] K.H. Schartner, D. Detleffsen, B. Sommer. Balmer-α emission in proton - hydrogen collisions. *Physical Review A* **136**, p.55 (1989).

[1.9] F.J. de Heer, R. Hoekstra, H.P. Summers. Excitation of He ($2^{1,3}$s) by electron impact. *Supplement to the Journal Nuclear Fusion* **3**, p.47 (1992).

[1.10] M. Anton, D. Detleffsen, K.-H. Schartner. Heavy ion impact excitation of helium: Experimental total cross-sections. *Supplement to the Journal Nuclear Fusion* **3**, p.51 (1992).

[1.11] W. Erb. Umladung schwerer Ionen nach Durchgang durch Gase und Festkörper im Energiebereich 0.2 bis 1.4 MeV/u. *GSI Report* **P-7-78** (1978).

[1.12] A. N. Perumal, V. Horvat , R.L. Watson, Y. Peng, K.S. Fruchey. Cross sections for charge change in argon and equilibrium charge states of 3.5 MeV/amu uranium ions passing through argon and carbon targets. *Nuclear Instruments and Methods in Physics Research B* **227**, p.251-260 (2005).

[1.13] V.P. Shevelko, I.L. Beigman, M.S. Litsarev, H. Tawara, I.Yu. Tolstikhina, G. Weber. Charge-changing processes in collisions of heavy many-electron ions with neutral atoms. *Nuclear Instruments and Methods in Physics Research B* **269**, p.1455 (2011).

[1.14] V. P. Shevelko, Th. Stöhlker, H. Tawara, I. Yu. Tolstikhina, and G. Weber. *Nuclear Instruments and Methods in Physics Research B* **268**, p.2611 (2010).

[1.15] J. Alonso, H. Gould. Charge-changing cross sections for Pb and Xe ions at velocities up to 4 10^9 cm/sec. *Physical Review A* **26**, p.1134 (1982).

[1.16] A. S. Schlachter, J. W. Stearns, W. G. Graham, K. H. Berkner, R. V. Pyle J. A. Tanis. Electron capture for fast highly-charged ions in gas targets: an empirical scaling rule. *Physical Review A* **27**, p.3372 (1983).

[1.17] L. P. Presnyakov, A. D. Ulantsev, Sov. Charge exchange between multiply charged ions and atoms. *Soviet Journal of Quantum Electronics* **4(11)**, p.1320 (1975).

[1.18] L. P. Presnyakov, D. B. Uskov, R. K. Janev. Ionization and charge exchange in atom collision with multicharged ion, *Journal of Experimental and Theoretical Physics* **86**, p.882-895 (1984).

[1.19] Y. Wu, P. C. Stancil, H. P. Liebermann, P. Funke, S. N. Rai, R. J. Buenker, D. R. Schultz, Y. Hui, I. N. Draganic, and C. C. Havener. Theoretical investigation of charge transfer between N^{6+} and atomic hydrogen, *Physical Review A* **84**, p.022711 (2011).

[1.20] V. K. Nikulin and N. A. Guschina. Single-electron charge transfer and excitations at collisions between Bi^{4+} ions in the kiloelectronvolt energy range. *Technical Physics* **52**, p.148 (2007).

[1.21] M. I. Chibisov. Charge exchange of atoms on multiply charged ions. JETP Letters **24**, p.46 (1976).

[1.22] R. E. Olson and A. Salop. Electron transfer between multicharged ions and neutral *Physical Review A* **14**, p.579 (1976).

[1.23] A. Bárány and C. J. Setterlind. Interaction of slow highly charged ions with atoms, clusters and solids: a unified classical barrier approach. *Nuclear Instruments and Methods in Physics Research B* **98**, p.184 (1995).

[1.24] H. Ryufuku and T. Watanabe. Total and partial cross sections for charge transfer in collisions of multicharged ions with atomic hydrogen. *Physical Review A* **20**, p.1828-1837 (1979).

[1.25] Dž. Belkić, I. Mančev, J. Hanssen. Four body methods for high-energy ion-atoms collisions. *Reviews of Modern Physics* **80**, p.249 (2008).

[1.26] N. Bohr. and K. Dan. The penetration of atomic particles trough matter. *Mat.-fys. Medd XVIII* **nr.8** (1948).

[1.27] G.D. Alton, L.B. Bridwell, M. Lucas, C.D. Moak, P.D. Miller, C.M. Jones,Q.C. Kessel, A.A. Antar, M.D. Brown. Single- and multiple-electron-loss-cross-section measurements from 20-MeV Fe^{4+} on thin gaseous targets. *Physical Review A* **23**, p.1073 (1981).

[1.28] I. Yu. Tolstikhina and V. P. Shevelko. Collision processes involving heavy many-electron ions interacting with neutral atoms. *Physics -Uspekhi* **56 (3),** p.213-242 (2013).

[1.29] J.R. Hook and H.E. Hall. Solid State Physics (2nd Edition). *Manchester Physics Series.*

[1.30] <u>A. Ananyeva,</u> O. V. Bogdanov, Yu. L. Pivovarov. *Journal of Surface Investigation. X-ray, Synchrotron and Neutron Techniques* **Vol.4** 282 (2010).

[1.31] O. V. Bogdanov, K. B. Korotchenko, Yu. L. Pivovarov. Features of the formation of radiation spectra at (111) planar channeling of relativistic electrons in a Si crystal. *Journal of Surface Investigation X-ray Synchrotron and Neutron Techniques* **3**(6), p.966-970 (2009).

[1.32] O. V. Bogdanov, E I Fiks, K B Korotchenko, Yu L Pivovarov, T A Tukhfatullin. Basic channeling with Mathematica©: A new computer code. *Journal of Physics Conference Series* **236**(1), p.012029 (2010).

[1.33] J. Linhard. Influence of Crystal Lattice on Motion of Energetic Charged Particles. Mat. Phys. Dan. Vid. Selsk. **34** (14) (1965).

[1.34] M.A. Kumakhov and G. Shimmer. Atomic collisions in crystals. *M. Atomizdat*, (1980).

[1.35] V.P. Shevelko. Atoms and Their Spectroscopic Properties. Springer Series on Atoms and Plasmas, Vol. **18**, p. 40 (1997).

[1.36] V.S. Lebedev, I.L. Beiman. Physics of Highly Excited Atoms. *Springer, Berlin,* (1998).

[1.37] W.R. Jonson and G. Soff. The Lamb Shift in Hydrogen-like Atoms, $1 \leq Z \leq 110$. *Atomic Data and Nuclear Data Tables* **33**, p.405 (1985).

[1.38] D.J. Griffiths. Introduction to Electrodynamics (3rd Edition). *Pearson Education, Dorling Kindersley*, (2007).

[1.39] G. Molière. Theorie der streuung schneller geladener teilchen I: Einzelstreuung am abgeschirmten coulomb-feld. *Z. f. Naturforsch. A.* **2**, p. 133–145 (1947).

2 Experiment

[2.1] Y. Hirao, H. Ogawa, S. Yamada, T. Murakami, A. Kitagawa, K. Sato, A. Itano, M Kumada, E. Takada, M. Kanazawa, K. Noda, M. Sudou, K. Kawachi, F. Soga, M. Endo, T. Kanai, S. Minohara, H. Koyama-Ito and T. Kohno. Heavy Ion Medical Accelerator in Chiba. A Design Summary and Update. *National Institute of Radiological Sciences*, (1992).

[2.2] Institute for Radiological sciences homepage (NIRS): http://www.nirs.go.jp/index.shtml

[2.3] Virginia Semiconductor Incorporated (VSI) homepage: https://www.virginiasemi.com/

[2.4] Ketek GmbH homepage: http://www.ketek.net/

[2.5] PGT homepage: http://www.pgt.com/

[2.6] S.M. Sze (1981). Physics of Semiconductor Devices (secondnd edition), *John Wiley and Sons (WIE).*

[2.7] First Sensor Technology GmbH: http://www.first-sensor.com/en

[2.8] NIST Database http://www.nist.gov/pml/data/asd.cfm

3 Data analysis

[3.1] G. Audi. The NUBASE Evaluation of Nuclear and Decay Properties. *Nuclear Physics A (Atomic Mass Data Center)* **729**, p. 3-128 (2003).

[3.2] B.L. Henke, E.M. Gullikson, and J.C. Davis. X-ray interactions: photoabsorption, scattering, transmission, and reflection at E = 50-30000 eV, Z=1-92. *Atomic Data and Nuclear Data Tables* Vol. **54** (no.2), p.181-342 (1993).

4 Results

[4.1] The NIST database: http://www.nist.gov/pml/data/asd.cfm

[4.2] A. A. Babaev and Yu. L. Pivovarov. Resonant Coherent Excitation of Ar^{17+} Ions Taking into Account a Fine Structure of Energy Levels. *Journal of Surface Investigation. X-ray, Synchrotron and Neutron Techniques*, Vol. **2**, No. 2, p. 241–244 (2008).

[4.3] Y. Nakano. PhD dissertation.

List of abbreviations

RCE – Resonant Coherent Excitation

DRCE – Double Resonant Coherent Excitation

HIMAC – Heavy Ion Medical Accelerator in Chiba

NIRS – National Institute of Radiological Sciences

RFQ – Radio Frequency Quadropole

Linacs – Linear accelerator

LEBT – Low Energy Beam Transport

HEBT – High Energy Beam Transport

VSI – Virginia Semiconductor Incorporated

SDD – Silicon Drift Detector

Si(Li) detector – Lithium-Drifted Silicon detector

PIN diode – Positive Intrinsic Negative diode

PSD – Position Sensitive Detector

NIST – National Institute of Standards and Technology

PIG – Penning Ionization Gauge

Curriculum vitae

Alena Ananyeva

Date of birth: 09.08.1988

Education:

09/2011 – 02/2015	**Beginning of the PhD study**, Goethe University (Frankfurt am Main, Germany)
	Thesis: "Double Resonant Coherent Excitation of Highly Charged Ions in Crystals"
	Supervisor: Prof. Dr. R. Dörner
09/2009 – 06/2011	**Master in physics**, Tomsk Polytechnic University (Russia)
	Thesis: "Resonant Coherent Excitation of Relativistic Highly-Charged Heavy Ions in Crystals"
	Supervisor: Prof. Dr. Yu.L. Pivovarov
09/2005 – 06/2009	**Bachelor in physics**, Tomsk Polytechnic University (Russia)
	Thesis: "Simulation of Axial Channeling Motion and Radiation Spectra of Relativistic Electrons in Crystals"
	Supervisor: Prof. Dr. Yu.L. Pivovarov

University lecturers: Yu.L. Pivovarov, Yu.Yu. Kryuchkov, V.A. Tryasuchev, N.K. Ryzhakova, V.I. Bespalov, I.I. Fix, A.Yu. Trifinov, G.V. Garanin, A.A. Baturin, Yu.M. Stepanov, V.P. Ponomarev, A.P. Mamontov, V.A. Serdyutsiy, D.N. Chislov.

Publications:

- R. Reuschl, T. Gassner, U. Spillmann, A. Bräuning-Demian, <u>A. Ananyeva</u>, H. Beyer, K.-H. Blumenhagen, W. Chen, S. Hagmann, M. Hegewald, P. Indelicato, M. Schwemlein, S. Toleikis, M. Trassinelli, S. Trotsenko, D. Winters, N. Winters, Th. Stöhlker. Lifetime measurement of the $2\,^3P_0$ state in He-like uranium. *Physica Scripta 2013* p.014024

- A. Bräuning-Demian, <u>A. Ananyeva</u>, T. Azuma, H. Bräuning, D. Dauvergne, Y. Kanai, Y. Nakano, T. Shindo, S. Suda, Y. Yamazaki. Resonant coherent excitation of 191.1 MeV/u U^{89+} ions planar-channeled in a silicon crystal. *Journal of Physics: Conference Series* **388**, p.1(2012)

- A. Ananyeva, O. V. Bogdanov, Yu. L. Pivovarov. Relativistic electron radiation spectra at axial channeling in crystals. *Journal of Surface Investigation. X-ray, Synchrotron and Neutron Techniques*, Vol.**4**, p.282 (2010)

Conferences:

09/2014   **Poster** "Observation of the Double Resonant Coherent Excitation of Ar^{16+} and Ar^{17+} ions in Crystals" (Bariloche, Argentina)

07/2014   **Invited Talk** "Observation of the Resonant Coherent Excitation of highly-charged ions in crystals", (INFN Frascati, Italy)

09/2012   **Talk** "Observation of the $2p_{3/2}$-$2s_{1/2}$ Radiative Transition in U^{89+} Using the Resonant Coherent Excitation", Physics of Highly Charged Ions Conference (Heidelberg, Germany)

09/2012   **Talk** "Resonant Coherent Excitation of Relativistic Highly Charged Ions at Planar Channeling in Si-Crystal", Channeling conference (Algero, Italy)

01/2011   **Talk** "Resonant coherent excitation of Li-like uranium in Si crystal", EAS - Extreme Atomic Systems (Riezlern, Austria)

10/2009   **Talk** "Simulation of motion and radiation Spectra of Relativistic Electrons and Positrons at Axial Channeling in Crystals", Physics and Progress conference (St.Petersburg, Russia)

09/2008   **Poster** "Spectra of Radiation of Relativistic Electrons at Axial Channeling in the Crystals", Channeling conference (Eriche, Italy)

Special achievements:

- The best early stage researcher award at the "Charged and Neutral Particles Channeling Phenomena 2012" conference (certificate)
- The best Master thesis at Physics department of Tomsk Polytechnic University in 2011 (1st place certificate)
- The best Bachelor thesis at Physics department of Tomsk Polytechnic University in 2009 (1st place certificate)

Acknowledgment

I would like to thank my supervisor Prof. Dr. Reinhard Dörner for accepting me as a PhD student. Thank you for your support and kindness. I am grateful to Prof. Dr. Toshiyuki Azuma for getting me involved into the experiments at the HIMAC facility (Japan) and accepting to be the second referee for this thesis. I would also like to thank Prof. Dr. Alwin Schempp and Prof. Dr. Joachim A. Maruhn who agreed to join the examination committee.

In the following I would like to sincerely thank those people whose help and cooperation made this work possible.

First of all, I would like to express my gratitude towards Dr. Angela Bräuning-Demian, my everyday supervisor at GSI who spent enormous time coaching me. Her guidance helped me in all the time of research and writing of this thesis.

I would like to particularly thank Dr. Yuji Nakano who has always been friendly and supportive, for his help and suggestions. I am also thankful to Dr. Helmut Weick, Dr. Anton Babaev, Prof. Dr. Vyacheslav Shevelko, Dr. Yury Kozhedub, Prof. Dr. Siegbert Hagmann, Dr. Eiichi Takada, Prof. Dr. Thomas Kühl, Dr. Hong-Keun Kim and Marianne Frey for their always prompt cooperation.

Finally, I would like particularly thank Prof. Dr. Yu.L. Pivovarov for introducing me to the GSI. He is the person whose motivation, enthusiasm, and immense knowledge inspired me and pushed forward and whose advice and support were invaluable.